BIOMECHANICS AND MODELING METHODS FOR QUANTIFYING MECHANICALLY-MEDIATED DISEASE PROGRESSION IN NEGLECTED POPULATIONS

A Dissertation
Presented to
The Academic Faculty

by

Alexander W. Caulk

In Partial Fulfillment
of the Requirements for the Degree
Doctor of Philosophy in Bioengineering in the
George W. Woodruff School of Mechanical Engineering

Georgia Institute of Technology
May 2015

Copyright © 2015 by Alexander Wilson Caulk

BIOMECHANICS AND MODELING METHODS FOR QUANTIFYING MECHANICALLY-MEDIATED DISEASE PROGRESSION IN NEGLECTED POPULATIONS

Approved by:

Dr. Rudolph L. Gleason, Jr., Adviser
School of Mechanical Engineering
Georgia Institute of Technology

Dr. Hanjoong Jo
School of Biomedical Engineering
Georgia Institute of Technology

Dr. W. Robert Taylor
School of Medicine
Emory University

Dr. Manu O. Platt
School of Biomedical Engineering
Georgia Institute of Technology

Dr. Roy L. Sutliff
School of Medicine
Emory University

Dr. J. Brandon Dixon
School of Mechanical Engineering
Georgia Institute of Technology

Date Approved: April 8, 2015

To my wife, Sarah, for her unconditional support, and to my family for a lifetime of encouragement

ACKNOWLEDGEMENTS

I owe an extreme debt of gratitude to the many people that made my tenure at Georgia Tech such an incredible experience. To start, I would not have been afforded the opportunity to complete this work without the help of my adviser, Dr. Rudy Gleason. Rudy is a true embodiment of the term “servant leadership” and has been nothing short of an excellent mentor, both personally and professionally. He taught me the importance not only of performing high quality scientific research but also to consider its broader impact and to search for ways in which we can utilize our opportunities to make a difference. The opportunities I had in my work with Rudy were innumerable, but perhaps the greatest was the chance to work abroad in Ethiopia. Between working at a hospital and volunteering with local women and children, my time could best be described as life-changing, and for that opportunity, I am truly grateful.

I would also like to thank the members of my reading committee for their contributions to my project and their investment in me as a student over the past five years. My graduate work took many different turns over the course of my studies, and my committee was there at each turn, ready to help direct and refine the project. Dr. Platt has always been readily available to discuss my project as well as my career goals. At each of our meetings, I was met with some combination of caution, correction, and encouragement (always encouragement), and looking back it seems that the combination was always what I needed. He served as a collaborator, a teacher, an advocate, and a mentor, and I am indebted to him for the countless hours he spent serving all of those roles for my benefit as a student. Dr. Sutliff offered himself as a resource on multiple occasions and challenged me on the aspects of my research in which I needed it most. He

offered career advice, reviewed fellowship applications, and most of all, he helped me to think through my project as a physiologist rather than an engineer. His assistance was invaluable, especially in regards to the branch of my project relating to HIV and cardiovascular disease. Dr. Jo provided his expertise in a unique blend of engineering and biology. His feedback on the relevance of the human studies in this project as well as the utility of the animal models was challenging and useful. More importantly, he encouraged me to always critically evaluate my study design, a process that is difficult but well worth the effort. Dr. Taylor was always willing to help and offer his perspective on the project. His unique experience as a physician and a researcher proved to be immensely helpful in the evaluation of my project, especially as it relates to our ultimate goal in the medical sciences – to improve the lives of others. His most valuable advice to me was to question everything, and along the way he coached me through that process. I owe Dr. Dixon special thanks for taking me on as an adjunct member of his lab and serving as a co-adviser for the last couple of years of my studies. Working under Dr. Dixon has been a privilege. His dedication to his students and his work are evident in his excitement for solving new problems, and the proactivity with which he operates makes him an excellent leader and mentor. I am grateful to have had the opportunity to work with him and to have seen such an outstanding model of servant leadership.

I would be remiss if I did not also mention the faculty and staff at IBB that gave me so much personal and professional advice along the way. Dr. Garcia offered many hours of his time to share his thoughts on faculty life, professional goals, and maintaining a healthy work/life balance. I had the opportunity to work directly with him when serving on the bioengineering graduate association, and he was always available to help and was

always an advocate for the students. Dr. Garcia is and has been an excellent leader for the bioengineering program, and the benefits I have received from his leadership and sacrifice are immeasurable. The staff in the PRL has been incredibly helpful over the past five years. Dr. O'Farrell seemed like a constant consultant for me as I brought her questions about experiments and procedures. Kim Benjamin, Ogeda Blue, Andrea Gibson, Altair Rivas, and Josh Scarbrough are easily the best animal caretakers that a person could ask for when conducting animal studies. They are dedicated, helpful, and always friendly, and working with them makes tedious experiments substantially more enjoyable. Andrew Shaw leads the microscopy core in IBB, a job for which he is well suited. I could never tell if he was more excited about microscopy in general or just simply being a resource to students, but either way he always seems available to help and always happy to do it. Aqua Asberry coordinates the histology core, and she works diligently to process samples, answer questions, and repair equipment, all while managing to keep a smile on her face. Her help was critical in the portions of this study requiring histological analysis. Lamar Dorsey deserves high praise for taking on the core facilities at TEP. The move to a new building is never easy. Lamar has done an excellent job of getting the new core facilities up and running, and he has been an excellent resource to those of us who struggled through the move and getting our projects back online. Chris Ruffin was the original academic adviser for our program. He was a bright and smiling face, a calming presence in an otherwise chaotic environment, and a constant friend to all of the students, faculty, and staff. His passing grieved the IBB community, and he will be remembered as a champion and advocate for the program. When Laura Paige stepped in as the new adviser, she had incredibly big shoes to fill, but I'm

convinced that nobody could have done it better than her. She is always one step ahead of the game, predicting questions and offering answers, and best of all she is every bit the advocate and friend that the students in our program need.

I also have many fellow students and lab mates that deserve special recognition. There have been many members of the Gleason lab that directly contributed to my success as a student. Dr. William Wan was the first member of the lab that I knew. He was my TA as an undergrad, my graduate adviser when I hired on in the lab, and he remains a colleague whom I am also privileged to call a friend. William's willingness to sacrifice for others is truly incredible. I still have the opportunity to bug him from time to time, and he never fails to respond with the same spirit of sacrifice that he's always had. I consider his countless pieces of advice particularly formative for my personal and professional development, and for that I owe him an extreme debt of gratitude. Dr. Anastassia Pokutta-Paskaleva joined the lab just before the wave of graduations and the exodus of students from our lab. I have learned a lot from her curiosity, her excitement, her attention to detail, and her desire to help. She has stepped in for me in the lab during times of crisis, led brainstorming and troubleshooting sessions, offered advice and encouragement, and overall just helped me keep my sanity during my final days as a graduate student. She is a constant source of positivity and a pleasure to have as a lab mate and friend. Dr. Laura Hansen was the pioneer of the HIV studies in our lab, and she is a true model of excellence in research and in her personal life. She happily jumped on to a new study, taking on all the headaches of the unknown in research, all while managing to be the leading runner, cook, and socialite in the lab. Her contributions, research and otherwise, and her relaxed presence made our lab a more enjoyable place to

work. Dr. Ruoya Wang can best be described as the idea guy. Roy has a clear and evident passion for his work. I am convinced that nobody brainstorms better than him, and his energy for productivity and accomplishment is one that is worthy of praise and duplication. Dr. Julia Raykin is a top notch scientist whose excitement for research is second only to her desire to see others succeed, and she has been an obvious impetus for the success of her peers, including me. Lab work aside, I will always value the opportunities that I had with Julia to engage in honest and heartfelt discussions regarding politics, philosophy, and life in general. Her thoughtfulness is truly admirable. There have been many others that have come and gone in the Gleason lab. Dr. Michael Zaucha, Seth Gazes, Kelly Straub, Daniel Howell, Prem Midha, and Yasaman Nemat were all instrumental in fostering a collaborative and fun environment.

Members of the Dixon lab have been especially welcoming and patient as I invaded their lab space and asked them for constant help, and they all deserve special recognition and thanks. Timothy has taken care of my cells, walked me through experimental procedures, and otherwise selflessly sacrificed his own time and energy for my sake. Tyler showed me their state-of-the-art imaging system and allowed me to utilize the system as well as all the time and resources that go along with it. Zhanna assisted with every ex vivo lymphatic test that is reported in this dissertation, and for that I owe her tremendous gratitude. Mike, Iris, Josh, and Anish were always around to answer any questions that I had about the lab or any procedures that I was running. In addition to their help, they have all gone out of their way to make me feel like a part of their lab. I'm thankful for the sense of community that they foster in their lab and for including me in it. Members of other labs have also been instrumental in the success of my graduate

school experience. Ivana Parker and Kristi Porter helped extensively in my HIV studies, particularly by offering their intellectual expertise and their time. JP Rabbah, Andrew Siefert, Mike Tree, Swetha Rathan, and the rest of the Yoganathan lab were always around to provide some friendly relief from the day-to-day work in the lab.

My family has also been instrumental in my success in my graduate studies and a constant source of support throughout my life. First, my in-laws have provided unending encouragement since the day that Sarah and I were married. Steve and Karen have offered themselves as a resource for both of us at the cost of many things, but most often their time, and they both have endeavored to pray for us daily, a task to which I'm certain they were unwaveringly dedicated. Lisa and Logan have walked side-by-side with us as we have navigated the difficulties of graduate school and have also prayed regularly for our success and well-being. I am overwhelmingly thankful to all of them for their love and support. My grandparents, Bob and Gerry, are a paragon of self-sacrifice, walking with each other in marriage for more than 60 years. Much of what I've learned about dedication and sacrifice I have learned from them as they have sought to serve their family before themselves. I will always appreciate their effort to be involved in my life, and I owe them a debt of gratitude that can likely never be paid. My siblings, Ben and Emily, are always a source of joy for me. In my most difficult moments, I have been able to rely on them as reminders of the things that are most important in life. I will be forever envious of my brother's ability to enjoy the moment and my sister's ability to operate independently. I have learned more from them than they could possibly realize, and I will always appreciate the love and support that they have given to me. There are not words enough to express my gratitude to my parents, Jim and Berni. The love they have shown

and the sacrifices they have made for me and my siblings are beyond my comprehension. I am incredibly grateful for their lifelong model of selflessness and dedication, a model to which I owe nearly all of my personal and professional success. I would not be writing this had it not been for love and support.

Last and certainly not least I have to thank my wife, Sarah. She is truly my better half; the fun-loving, thrill-seeking but somehow has-it-all-together woman that I met four years ago willingly chose to join herself to a guy that was living hand-to-mouth and had a strict 10:00 PM bedtime. Her decision will always baffle me, but if there's anything I've learned from scientific research, it's that you don't ask "Why?" when fate smiles upon you. If a better partner than Sarah exists, she is beyond my imagination. Sarah has been overwhelmingly supportive, a teammate in my victories, an emotional pillar in my failures, and overall the object of my admiration. Her intellect and ambition are second only to her selflessness. I am truly honored to be called her husband, and I look forward to sharing in the many more thrills that she'll undoubtedly discover for us, as long as she finds them before bedtime.

It is my personal conviction that nothing of value in this life is earned, but rather all of it is given. I have not earned the encouragement of my peers; they have provided it willfully. I have not earned the loyalty of my friends; they have extended it freely. I have not earned the love of my family; they have offered it selflessly. It is with this conviction and profound humility that I offer my utmost thanks to my Lord and Savior, Jesus Christ, who gave of himself ultimately and offered the perfect sacrifice, saying, "Greater love hath no man than this, that a man lay down his life for his friends." Of all the things that I have received without merit, His love is by far the greatest.

TABLE OF CONTENTS

LIST OF TABLES

LIST OF FIGURES

LIST OF ABBREVIATIONS

3D	3-dimensional
AAA	Abdominal aortic aneurysm
AHA	American Heart Association
AIDS	Acquired Immune Deficiency Syndrome
AIx	Augmentation index
AIx-75	Augmentation index normalized to heart rate of 75 bpm
ANOVA	Analysis of Variance
AP	Augmentation pressure
$ApoE^{-/-}$	Apolipoprotein E null
ART	Antiretroviral Therapy
AZT	Azidothymidine
Bas	Basophil granulocytes
CBC	Complete blood count
CCA	Common carotid artery
cm	Centimeter
CVD	Cardiovascular disease
DBP	Diastolic blood pressure
dL	Deciliter
DNA	Deoxyribonucleic acid
ECM	Extracellular matrix
EDD	End diastolic diameter
EFV	Efavirenz
EKG	Electrocardiogram
ELISA	Enzyme-linked immunosorbent assay
eNOS	Endothelial nitric oxide synthase
Eos	Eosinophil granulocytes
ESD	End systolic diameter
FMD	Flow-mediated dilation
FSI	Fluid-structure interaction
HA	Heart attack
HAART	Highly active antiretroviral therapy
HCT	Hematocrit
HDL	High-density lipoprotein
H&E	Hematoxylin and eosin
HGB	Hemoglobin
HIV	Human immunodeficiency virus
HIV-1+	HIV-1 positive
hsCRP	High-sensitivity C-reactive protein
(s)ICAM-1	(Soluble) Intracellular adhesion molecule-1
IL-1	Interleukin-1
IMT	Intima-media thickness
INSTI	Integrase strand transfer inhibitor
KO	Knockout
LDL	Low-density lipoprotein

LPV/r	Ritonavir-boosted lopinavir
Lym	Lymphocyte
µg	Microgram
µL	Microliter
MCH	Mean corpuscular hemoglobin
MCHC	Mean corpuscular hemoglobin concentration
MCV	Mean corpuscular volume
mL	Milliliter
mm	Millimeter
mmHg	Millimeters of mercury
mN	Millinewton
Mon	Monocyte
MP	Mean pressure
MPV	Mean platelet volume
Neu	Neutrophil
ng	Nanograms
NRTI	Nucleoside reverse transcriptase inhibitor
NNRTI	Non-nucleoside reverse transcriptase inhibitor
NO	Nitric oxide
NOS	Nitric oxide synthase
NRTI	Nucleoside reverse transcriptase inhibitor
NVP	Nevirapine
PBS	Phosphate buffered saline
PCT	Plateletcrit
PDW	Platelet distribution width
PI	Protease inhibitor
PLT	Platelet
PP	Pulse pressure
PSS	Physiologic saline solution
PWA	Pulse wave analysis
PWV	Pulse wave velocity
RBC	Red blood cell
RDW-CV	Red blood cell distribution width-coefficient variation
RDW-SD	Red blood cell distribution width-standard deviation
RNA	Ribonucleic acid
ROS	Reactive oxygen species
SBP	Systolic blood pressure
SEM	Standard error of the mean
SHG	Second harmonic generation
SMC	Smooth muscle cell
SNP	Sodium nitroprusside
TC	Total cholesterol
TDF	Tenofovir disoproxil fumarate
TG	Triglycerides
(s)VCAM-1	(Soluble) Vascular cell adhesion molecule-1
WBC	White blood cell

LIST OF SYMBOLS

$\mathbf{F}$	Deformation gradient
$\mathbf{T}$	Cauchy stress tensor
$\mathbf{C}$	Right Cauchy-Green strain tensor
$\mathbf{I}$	Identity matrix
W	Strain energy function
α^k	k^{th} fiber family angle
b	Neo-Hookean material parameter
$b_k^{\,1}$	First k^{th} family material parameter
$b_k^{\,2}$	Second k^{th} family material parameter
p	Lagrange multiplier
P	Pressure
a	Loaded inner radius
h	Loaded thickness
l	Loaded length
A	Unloaded inner radius
H	Unloaded thickness
L	Unloaded length
λ_θ	Circumferential stretch ratio
λ_r	Radial stretch ratio
λ_z	Axial stretch ratio
RV_x	Maximum valve resistance
RV_n	Minimum valve resistance
Q_L	Flow through a vessel
Q_V	Flow across a valve
Δp	Pressure drop
p_o	Pressure differential at which a valve changes state
μ	Kinematic viscosity
ρ	Fluid density
g	Acceleration due to gravity
f	Frequency
dt	Change in time
η_r	Time constant governing radial growth
η_θ	Time constant governing circumferential growth
η_τ	Time constant governing shear-induced circumferential growth

SUMMARY

Biomechanics plays a key role in the development and maintenance of biological tissue. It is well known that biological tissue grows and remodels in response to varying mechanical loads. Arteries and lymphatic vessels share many similar mechanical loads such as luminal pressure, axial force, and fluid shear force on the endothelium. Diseases of these vascular systems have frequently been associated with deviations from a hypothesized "preferred" homeostatic mechanical environment and maladaptive growth and remodeling. Changes in mechanical loading such as hypertension and disturbed flow have been shown to lead to well known preclinical markers of cardiovascular disease including arterial stiffening, increased thickness of the arterial wall, and endothelial dysfunction as diagnosed by a decrease in flow-mediated dilation. Similarly, although the progression of lymphedema is less understood, lymphatic dysfunction has been associated with changes in luminal and/or interstitial pressure and tissue remodeling that includes thickening of the lymphatic wall.

Mechanically-mediated disease development affects many populations, but developing nations face challenges that are unique due to disease burdens that are specific to the regions. Treatment strategies for HIV have resulted in HIV-positive patients living longer lives, but these patients also suffer from non-AIDS-related comorbidities including accelerated progression of cardiovascular disease. Such progression may occur via mechanisms that differ from traditional pathways leading to cardiovascular disease in the developed world. Developing nations, specifically those in sub-Saharan Africa, carry the majority of the burden of HIV infection and, consequently, its associated comorbidities, making the characterization of HIV-associated

cardiovascular disease a critical step in the treatment and care of a large population. Similarly, lymphedema is a common side effect of lymphatic filariasis, a condition characterized by parasitic infection that occurs preferentially in tropical areas. Again, sub-Saharan Africa carries a significant portion of the burden of lymphatic filariasis and suffers from significant disability burden due to the lack of treatment options for lymphedema associated with lymphatic filariasis. The overall goal of this project is to develop novel experimental and theoretical frameworks for the study of mechanically-mediated diseases of the arterial and lymphatic vasculature that are commonly seen in developing nations with the ultimate intention of identifying key parameters that contribute to tissue growth and remodeling that underlie disease progression.

In this study, we investigated the progression of two primary pathologies: HIV-associated cardiovascular disease and mechanically-mediated progression of lymphatic dysfunction. First, we investigated the role of efavirenz (EFV), a commonly used antiretroviral for HIV treatment, in the progression of early markers of cardiovascular disease. We characterized EFV-associated vascular remodeling and dysfunction in adult and pediatric HIV-1-positive Ethiopian populations. Arterial stiffness was quantified via pulse wave analysis and pulse wave velocity with applanation tonometry, and carotid intima-media thickening and impairment of brachial flow-mediated dilation were quantified using non-invasive ultrasound. We found that adult patients infected with HIV-1 who were taking EFV-containing treatment regimens had increased aortic stiffness as measured by pulse wave velocity compared to NVP-containing treatment regimens (a similar drug of the same class of antiretrovirals) as well as decreased brachial flow-mediated dilation and increased normalized carotid intima-media thickness (cIMT)

compared to HAART-naïve controls and NVP-treated subjects, indicating endothelial dysfunction and maladaptive vascular remodeling due to EFV treatment. Correlation and regression analysis revealed that current EFV use was an independent predictor for increased pulse wave velocity and increased normalized cIMT.

Additionally, we developed a novel experimental and theoretical paradigm to quantify lymphatic mechanical function and mechanically-mediated growth and remodeling to highlight key parameters that may be contributing to the onset of lymphedema. We quantified the *ex vivo* passive and active mechanical properties of rat thoracic ducts using a microstructurally-motivated constitutive model and incorporated the theoretical framework and experimentally-determined parameters into a lumped parameter model to predict the mechanical environment of a lymphatic vessel during active and passive lymph transport. Using this predictive model, we then developed a novel framework for prediction of lymphatic growth and remodeling and identified potential parameters involved in the progression of lymphedema. This study serves to identify possible contributors to mechanically-mediated lymphatic dysfunction using a novel mathematical framework and consequently provide direction for future investigations of lymphatic dysfunction.

This dissertation demonstrates the utility of modeling and biomechanics in the investigation of disease progression in understudied populations using applied biomechanics concepts in clinical, experimental, and theoretical contexts. The application of biomechanics to the study of arterial and lymphatic dysfunction in this study has successfully identified potential parameters involved in the progression of cardiovascular disease associated with HIV treatment as well as the progression of mechanically-

mediated lymphatic dysfunction. This work can be utilized in future studies as we continue to parse out specific mechanisms driving mechanically-mediated disease progression.

CHAPTER 1

INTRODUCTION

Medical advances over the past century have dramatically improved both life expectancy and quality of life for many global populations. However, it is well known that the benefits of medical advancement are strikingly different between people groups. Results from the Global Burden of Disease study recently reported healthy life expectancy (i.e. years of life without disability) for all nations in 2010. Countries in sub-Saharan Africa dominated the bottom of the list for both men and women, with values as low as 38 years in the Central African Republic [1]. Compare this to the 70+ year healthy life expectancy in Japan, and the disparity between public health burdens becomes obvious.

In order to effectively combat such a staggering statistic, it is critical that we first understand the problem before providing a solution. Sub-Saharan Africa has been devastated in recent years by the AIDS epidemic [2], and while the advent of HAART has transformed HIV from a death sentence into a chronic and manageable disease, many still suffer from the large number of co-morbidities associated with HIV infection and treatment. Such co-morbidities include neurological disorders, nephropathy, diabetes, malnutrition, dyslipidemia, and cardiovascular disease (CVD) [3]. More specifically, CVD related to HIV has been attributed to both the infection as well as the treatment, creating difficulty in understanding the pathology associated with this condition. Additionally, diseases such as lymphatic filariasis, while not generally fatal, contribute to a substantial portion of the burden of global disability rates. Approximately 40 million people worldwide are disfigured or disabled by lymphedema associated with lymphatic

filariasis [4], and again sub-Saharan Africa carries a significant portion of the burden [5]. As with HIV-induced CVD, the pathological development of lymphedema is not well understood.

Within the past few decades, much research has been dedicated to understanding the role of mechanics in disease development, and many important discoveries have been made that suggest disease pathology may in many cases be mechanically-mediated [6]. This knowledge offers a novel perspective in the search for a solution to disease burden in underdeveloped nations, including HIV-induced CVD and lymphedema associated with lymphatic filariasis. This dissertation aims to utilize modeling approaches to quantify the role of mechanics in the development of these conditions with the ultimate goal of supporting long-term efforts at identifying therapeutic targets for the treatment and prevention of these and other diseases.

1.1 Specific Aim 1: Characterize the role of efavirenz in HAART-induced mechanically-mediated vascular remodeling in an HIV-positive Ethiopian cohort as well as a mouse model of atherosclerosis.

Clinical studies have shown an increased incidence of preclinical markers of atherosclerosis such as arterial stiffening, endothelial dysfunction, and thickening of the arterial wall along with resultant cardiovascular events following the initiation of HAART [7]. While most clinical studies addressing cardiovascular-related comorbidity with HIV are focused on the developed world, the majority of the burden of HIV infection is in sub-Saharan Africa, with 69% of the HIV-infected population residing there [2]. Treatment programs in Africa have dramatically reduced HIV-related deaths, but disparities in infrastructure inhibit patient access to follow-up treatment and a broad

range of combination therapy. Consequently, patients in sub-Saharan Africa remain on first-line therapy, which often includes EFV, for a longer period of time.

Despite the prevalence of EFV in first line therapy, research addressing its role in the development of HAART-related CVD is minimal, with only a handful or recent reports quantifying its role in vascular dysfunction [8, 9]. Because treatment involves a cocktail of drugs as opposed to a single drug, the use of animal models is a desirable route in the effort to characterize the role of EFV in CVD development. Laboratory studies of EFV have shown vascular dysfunction [8], mitochondrial dysfunction [10, 11], and increased production of ROS [10]. Laboratory studies of other drug classes for HIV treatment have demonstrated similar results in addition to arterial stiffening and alteration of cathepsin expression and activity [12]. Given the clinical need and available laboratory data, our *working hypothesis is that EFV will be associated with arterial stiffening and vascular remodeling in an Ethiopian cohort of HIV-positive patients and will lead to arterial stiffening and aortic intima-media thickening in a mouse model of atherosclerosis.*

1.2 Specific Aim 2: Develop an experimental / theoretical paradigm to characterize lymphatic dysfunction associated with mechanically-mediated growth and remodeling.

Lymphatic function is directly dependent on the ability of lymphatic vessels to spontaneously and rhythmically contract to transport fluid against an unfavorable pressure gradient, a function which, if impaired, leads to lymphedema. Progression of lymphedema can be spontaneous (primary or idiopathic lymphedema), or it can occur following cancer treatment or parasitic infection. Lymphedema is estimated to occur in

12.5% of cases of lymphatic filariasis infection, and sub-Saharan Africa contains approximately 40% of the world's cases of infection, suggesting that approximately 5 million cases of lymphedema occur in sub-Saharan Africa due to lymphatic filariasis alone [5].

It is well known that the mechanical environment of lymphatic vessels contributes to their contractile function [13, 14]. Consequently, much work has been devoted to quantifying the relationship between mechanical cues such as inlet and outlet pressure, magnitude and direction of flow, and pressure gradient and lymphatic contractile function. In the context of lymphedema, lymphatic contractile function is inhibited to the extent that lymph propulsion no longer exists. Mechanically-mediated growth and remodeling has been well established in biological tissue (see, for example [15]), and given the intimate relationship between mechanical cues and lymphatic function together with observed tissue thickening in lymphedema [16], it seems likely that mechanically-mediated growth and remodeling may be a primary contributor to the loss of contractile function that leads to lymphedema. Experimentally-motivated mathematical models describing such a process are glaringly absent, and thus *the goal of this aim is to develop a theoretical paradigm that incorporates experimental data to quantify the relationship between mechanically-mediated growth and remodeling and concomitant loss of lymphatic contractile function in order to identify key parameters in the progression of lymphedema.*

CHAPTER 2

BACKGROUND AND LITERATURE REVIEW

2.1 Arterial structure and function

Systemic circulation consists of arteries, which are responsible for carrying oxygenated blood from the heart to the peripheral tissues, and veins, which are responsible for carrying deoxygenated blood from the peripheral tissues to the heart for oxygenation. Arteries can be divided into two categories: *elastic* arteries are generally larger arteries that are closer to the heart (e.g. aorta, common carotid arteries), and *muscular* arteries are generally smaller vessels and located closer to peripheral tissues (e.g. femoral artery, cerebral artery). The arterial wall consists of three primary layers: the intima, the media, and the adventitia [17]. The intima is a single layer of endothelial cells lining the luminal face of the vessels and exists to provide a non-thrombogenic surface as well as to regulate transport of substances from blood to tissues and vice versa. During inflammatory cascades, endothelial permeability is increased to facilitate transport of immune cells. Endothelial cells are capable of sensing and responding to the local flow environment and thus also assist in the regulation of blood pressure via production of nitric oxide (NO) and subsequent relaxation of vascular smooth muscle cells [18]. The media is a layer of vascular smooth muscle cells (SMCs) and numerous sheets of elastic lamina. In elastic arteries, the vascular smooth muscle is organized into concentric layers that are separated by thin fenestrated sheets of elastin. In muscular arteries, smooth muscle generally appears as a single layer surrounded by an internal and external layer of elastin. Vascular SMCs are capable of communicating with neighboring

cells, a function which is critical for maintenance of blood pressure following production of signaling molecules by endothelial cells. Finally, the adventitia is the outermost layer of the artery wall and is comprised mostly of collagen and fibroblasts. The adventitia is the primary load-bearing component of the arterial wall and serves to limit the extent to which an artery can extend following systolic contraction of the heart.

All constituents of the arterial wall work together to govern both the mechanical and biological functions of the systemic circulation. Interruption or alteration of any cellular or structural function of any component can inhibit the ability of the vessels to function properly, leading to any number of cardiovascular diseases including hypertension, coronary artery disease, atherosclerosis, and peripheral arterial disease.

2.2 Cardiovascular disease

Cardiovascular disease (CVD) is currently the leading cause of death in the developed world, causing as many as one in three deaths in the United States and killing approximately 2200 Americans every day [19]. Most CVD-related deaths are attributable to atherosclerosis and eventual ischemia. In 2008, cardiovascular events related to ischemic heart disease (i.e. heart attacks and strokes) in the United States were responsible for 13.5 million out of 17.3 million deaths worldwide [20]. Atherosclerosis is a condition in which lipids accumulate in the arterial wall and eventually form calcified plaques. These plaques can rupture, leading to thrombosis and complete occlusion of the lumen of a vessel, thus preventing blood flow to critical organs such as the heart and brain. Risk factors for CVD are partially behavioral. Tobacco use, physical inactivity, unhealthy diet, and alcohol abuse are all primary contributors to CVD [21]. Metabolic

risk factors also exist such as hypertension, elevated blood sugar, increased cholesterol, and obesity, and still others exist such as ethnicity, age, and gender [21].

Atherosclerosis is considered a chronic inflammatory condition due to the constant cascade of immune cells and inflammatory cytokines associated with its progression [22]. Progression of atherosclerosis begins with activated endothelial cells and subsequent endothelial dysfunction marked by an increase in endothelial permeability, increased expression of adhesion molecules, and decreased shear-induced production of NO [23]. Many have suggested that such endothelial dysfunction is due in large part to a change in the hemodynamic environment due to altered or disturbed blood flow [24-26], a hypothesis which arose from the discovery that atherosclerotic plaques occur preferentially in locations of disturbed flow [27]. Increased expression of adhesion molecules attracts circulating monocytes to attach to the vascular endothelium, and increased endothelial permeability then allows an influx of monocytes, platelets, and T-lymphocytes into the arterial wall [22]. Monocytes differentiate to become macrophages that ingest lipoproteins and eventually become the lipid-laden foam cells that form the characteristic fatty streaks that form in the early stages of atherosclerosis. These cells secrete various chemokines that continue to attract additional monocytes and promote a positive feedback loop of lipid accumulation in the wall. As lipids accumulate, smooth muscle cells begin to change to a synthetic phenotype, a process which results in increased production of collagen and decreased vascular compliance [28]. Note, however, that arterial stiffening and thickening of the carotid wall are also considered risk factors for cardiovascular events that precede plaque progression, so decreased compliance and vascular remodeling likely occur prior to plaque accumulation in the wall of the artery

[29, 30]. Without behavioral, pharmaceutical, or surgical intervention, atherosclerotic plaques will continue to grow until the lumen is mostly occluded, likely resulting in plaque rupture, thrombosis, and a subsequent ischemic cardiovascular event.

Clinically, there are multiple methods for assessing markers of CVD in order to increase awareness and decrease risk of cardiovascular events. Endothelial dysfunction is diagnosed via measurement of flow-mediated dilation (FMD) in which blood flow is occluded and flow-induced dilation of an artery (usually the brachial artery) is quantified using ultrasound following the release of the occlusion. Decreased FMD is interpreted as endothelial dysfunction due to the presumed lack of NO production by the endothelial cells upon increased blood flow [31]. Increased intima-media thickness (IMT) of the carotid artery is another preclinical marker of CVD that can be easily assessed using ultrasound [30, 32]. Arterial stiffness can also be quantified using either pulse wave velocity (PWV) or pulse wave analysis (PWA) which are quantified using applanation tonometry [33]. Lastly, coronary artery calcification can be measured using computed tomography in order to quantify the level of calcium deposits in an artery, a metric which follows the progression of atherosclerosis.

2.3 HIV and highly active antiretroviral therapy

The Human Immunodeficiency Virus (HIV) was first diagnosed when the Centers for Disease Control reported an outbreak of pneumocystis pneumonia in an otherwise healthy group of young homosexual males in New York City and San Francisco [34]. By 1987, the first antiretroviral drug for the treatment of HIV (AZT) was produced. While the treatment was somewhat successful, viral mutations resulted in drug resistance that led to development of other drugs and eventually a standard treatment consisting of a

cocktail of three drugs, now known as highly active retroviral therapy (HAART). The result of the development of HAART has been undeniable: HIV has transformed from a death sentence to a chronic and manageable disease. Indeed, the introduction of HAART led to a decrease in AIDS-related mortality in the United States by 47% in 1997 [35].

HIV is a lentivirus that causes the acquired immunodeficiency syndrome (AIDS). HIV infects many different immune cells, but primarily CD4+ lymphocytes, by first binding to the cell surface. Binding is promoted by the expression of the CD4 receptor and a chemokine receptor, usually CXCR4 or CCR5 [36]. Following fusion with the membrane, the virus undergoes a shedding process in which the viral RNA is incorporated into the host cell's DNA via reverse transcription. Viral DNA is then integrated into the genome DNA, new viral genes are transcribed, and the RNA is either packaged into new virions or translated into viral proteins. Proteins then move close to the cell membrane and begin a budding process to form a new virus that contains all of the necessary RNA and proteins to repeat the process in another host cell.

HAART treatment consists of a daily regimen of three drugs that work together to inhibit replication of HIV. Multiple drug types exist and are prescribed in particular combinations based on drug-drug interactions as well as patient considerations such as age, previous HAART experience, and current viral load or CD4 cell count. Most prescribed first-line therapy consists of a backbone of nucleoside reverse transcriptase inhibitors (NRTIs) along with either a non-nucleoside reverse transcriptase inhibitor (NNRTI), a protease inhibitor (PI), or an integrase strand transfer inhibitor (INSTI) [37]. NRTIs and NNRTIs have similar mechanisms of action in that they both inhibit the reverse transcriptase enzyme and thus prevent incorporation of viral RNA into the host

cell genome [38]. A dual NRTI backbone is most often prescribed to patients who have never undergone HAART therapy, and the most commonly recommended backbone is tenofovir disoproxil fumarate (TDF) together with emtricitabine (FTC) [37]. This backbone is frequently prescribed with efavirenz (EFV), the most commonly prescribed NNRTI. PIs operate differently by inhibiting the protease enzyme that facilitates cleaving and final assembly of the mature virus following replication, thus allowing viral replication within the cell but preventing the virus from maturing and infecting other cells [38]. PIs are also often prescribed with the common dual NRTI backbone. Some common PIs include ritonavir-boosted atazanavir (ATV/r), ritonavir-boosted lopinavir (LPV/r), and ritonavir-boosted darunavir (DRV/r). INSTIs also inhibit integration of the viral RNA into the host cell's DNA by inhibiting the integrase enzyme [39]. Some INSTIs that are recommended for use with a dual NRTI backbone are dolutegravir (DTG) and elvitegravir (EVG) [37]. Fusion inhibitors and CCR5 co-receptor antagonists are also relatively newly available drug types but are prescribed much less frequently than the other drug types listed here.

2.4 HIV, HAART, and cardiovascular disease

The advent of HAART has resulted in patients infected with HIV-1 living much longer lives. However, these patients are now suffering from many non-infectious comorbidities. HIV-1+ patients suffer from increased incidence of neurological disorders such as toxicity of the central nervous system and peripheral neuropathy, diabetes, dyslipidemia and lipodystrophy, renal failure, bone fracture, and cardiovascular disease [3, 40]. Of particular interest is the association between HIV and CVD. Multiple studies have shown that HIV-1+ patients are at increased risk of cardiovascular and

cerebrovascular events [7, 41-44], have atherosclerotic lesions [45-47], and present with multiple preclinical markers of atherosclerosis including arterial stiffness [48-50], increased cIMT [48, 51], and impaired FMD [52, 53]. However, the exact mechanisms driving the progression of CVD in HIV-1+ patients are still not fully understood. Some studies have implicated the viral infection as a singular cause of CVD, demonstrating coronary arteriopathy and atherosclerotic lesions following post-mortem analysis of HAART-naïve HIV-1+ patients [54, 55], and many laboratory studies have implicated HIV-1 proteins in preclinical markers of atherosclerosis and vascular dysfunction [56-59]. However, multiple other studies have shown an increase in markers of CVD between HAART-naïve and HAART-treated patients [48, 52, 53, 60, 61]. Consequently, many laboratory studies have been devoted to understanding the individual roles of HIV-1 proteins or specific HAART drugs on the development of markers of CVD.

Various HIV-1 proteins have been shown to cause markers of CVD via different mechanisms. The Tat protein has been linked to endothelial dysfunction in porcine coronary arteries via NOS inhibition [62]. The same protein has also been shown to bind to endothelial cells and alter secretion of matrix remodeling proteins, cell-cell adhesion, angiogenesis, and vascular permeability [63-67]. Parker et al. showed that Tat increases expression of matrix remodeling proteins (cathepsin K) in areas of the vasculature with low or oscillatory shear stress [58]. Hansen et al. demonstrated a synergistic role of multiple HIV-1 proteins in the onset of arterial stiffening in a transgenic rat model [56], and Kline et al. demonstrated increased ROS production using the same model [57]. Similarly, gp120 and Tat have both been implicated in the production of reactive oxygen species in brain endothelial cells by multiple groups [68-70].

While it seems clear that HIV-1 infection alone may contribute to accelerated progression of CVD due to the impact of HIV-1 proteins on vascular function and the inflammatory cascade initiated by infection, many other studies have also implicated the treatment as a primary contributor to vascular dysfunction and CVD. Multiple markers of CVD are exacerbated in HIV-1+ patients receiving HAART (compared to HAART-naïve patients) including arterial stiffening [71-74], impaired FMD [52, 75-77] (noting exceptions in Gupta et al. in which various HAART treatments were different, but not compared to HAART-naïve), and increased cIMT [46, 78]. NRTIs have been heavily implicated in the development of these markers. In a longitudinal study, van Vonderen et al. showed a *decrease* in carotid arterial stiffness, but increase in femoral artery stiffness after 24 months of AZT+3TC+LPV/r treatment (an NRTI-based regimen), with similar trends in NVP+LPV/r treatment (an NNRTI-based regimen) [71]. Indeed, laboratory studies have corroborated the role of various NRTIs, most commonly AZT, in progression of markers of CVD. AZT causes endothelial dysfunction via increased production of reactive oxygen species [79-82], intima-media thickening [12, 83], and arterial stiffening [12]. Similarly, PIs have been widely implicated class of antiretroviral drugs associated with atherosclerosis and have been correlated with increased c-IMT [84, 85], impaired FMD [86-88], dyslipidemia [89], atherosclerosis [7, 90], and myocardial infarction [91], but others have reported contradictory results [92-96]. NNRTIs have been associated with elevated cholesterol levels and triglycerides [7], with EFV associated with higher total cholesterol and triglyceride levels than NVP [89]. Less is known about the association between NNRTIs and c-IMT, FMD, and arterial stiffness. Some laboratory studies have implicated EFV in development of endothelial dysfunction in

coronary endothelial cells via ROS production [8] as well as mitochondrial dysfunction and ROS production in hepatic cells [10, 11]. Others have shown EFV to be cytotoxic in Jurkat T cells and peripheral blood monocytes [97]. Mondal et al. reports that EFV alone does not contribute to increased leukocyte adhesion [98], so the detrimental effects of EFV have still not been fully characterized. Given this plethora of data, there clearly exists a need to further elucidate the effects of individual drugs and combined therapy and investigate the mechanisms behind HAART-induced cellular dysfunction and disease progression.

2.5 Vascular mechanics and growth and remodeling

As early as 1880, Dr. Charles Roy observed that "with animal tissues (excepting bone), [Hooke's Law] does not hold good" [99]. Since then, many have sought to accurately characterize the behavior of biological tissue. The mechanical environment of blood vessels consists primarily of luminal pressure, axial force, and shear stress on the endothelium. Some vessels such as coronary arteries experience a high degree of torsion during loading from contractions of cardiac muscle [100], but in general, mechanical forces can be simplified to in plane forces excepting fluid shear stress. Previous observations have asserted that elastin is the primary load-bearing constituent under low-loading conditions, whereas collagen supports the majority of the load under high-loading conditions [101]. The mechanical environment can be easily quantified using Laplace's Law to calculate the average stresses in the wall of the vessels based on the applied loads and the geometry of the vessels. However, such quantification neglects stress distributions within the wall of the vessel and does not adequately predict the highly non-linear, heterogeneous, anisotropic behavior of the tissue. In order to accurately

characterize the complex behavior of the vessels, a combination of an accurate strain energy function and an appropriate kinematic framework must be considered. Appropriate kinematics are generally simplified to include only inflation and extension; however, some models have included torsion to account for forces experienced in coronary arteries [102]. Additionally, Chuong and Fung identified the presence of residual stresses in arteries that became a critical consideration for accurate predictions of stress in a 3D framework [103]. Various empirical strain energy functions have been proposed that capture the non-linearity of vascular tissue while treating the tissue as homogeneous [104-107]. Additional functions have been proposed and utilized that are more phenomenological and attempt to account for contributions from the microstructure of the vessel [108-110], and other models have moved beyond characterization of the passive mechanics to include active stress contributions due to smooth muscle cell contraction [111]. Ex vivo testing can be performed in order to acquire data regarding mechanical behavior, and non-linear regression analysis can then be performed using any of the constitutive models here in conjunction with Laplace's Law to quantify parameters associated with specific tissue. This parameter estimation process provides a wider range of parameters describing material behavior (as opposed to a single value such as Young's modulus for linear elastic behavior) and also provides a methodology for quantification of differences in mechanical behavior between tissue types [112].

Accurate quantification of the mechanical environment of blood vessels has become an important focus since studies have suggested that arteries grow and remodel to restore homeostatic values of stress. These studies have shown that arteries have an increased radius in response to increased flow in order to restore wall shear stress [113]

as well as increased thickness in response to increased blood pressure in order to restore circumferential stress [114]. Other studies have shown that axial stress is regulated by remodeling of the arterial wall as well [115]. The remodeling described in these studies is indicative of the remodeling seen in the progression of preclinical markers of atherosclerosis, especially thickening of the arterial wall. Consequently, many have sought to quantify the growth and remodeling process in order to identify key parameters that drive the process. Such models were initially proposed as volumetric growth, defined as uniform growth of infinitesimally small volumes of the arterial wall in response to changes in mechanical loading [116, 117]. In these models, growth can be governed mathematically by evolution equations containing parameters that drive the rate at which the tissue grows in particular directions as well as the stimulus that drives the growth. However, these models cannot account for preferential growth of particular constituents within the wall. Consequently, constrained mixture models of growth and remodeling have been proposed that describe tissue growth in terms of increased production of collagen, elastin, and SMCs [118-122]. These models utilize the kinematic assumptions and constitutive equations previously detailed as well as new evolution equations that govern the unloaded states of newly produced constituents as well as the rate at which they are produced. Volumetric models as well as constrained mixture models can support either empirical or microstructurally-motivated constitutive models, and all types have been utilized extensively to predict growth and remodeling behavior of arteries.

2.6 Lymphatic physiology and function

The lymphatic system is a robust network of vessels and organs that serves multiple functions including immune trafficking, lipid transport from the gut to the

bloodstream, and tissue fluid balance [123]. Transport of fluid through lymphatics begins at the peripheral tissues with fluid uptake into lymphatic capillaries and continues with fluid transport into progressively larger lymphatic vessels (precollecting lymphatics and collecting lymphatics), eventually returning to the venous circulation through the thoracic duct. The lymphatic system is unique from the systemic circulation in that the lymphatic system is not a closed circulatory system but rather a one-way conduit for fluid. The lymphatic system lacks a central pump to propel fluid forward to its destination, which presents a unique challenge given that the system is often working against a negative pressure gradient. Consequently, lymphatic vessels are capable of spontaneous and rhythmic contraction that provides them with the ability to effectively transport fluid against a negative gradient, a function which, if impaired, leads to fluid imbalance and lymphedema.

Collecting lymphatics have similar structure to arteries in that they are composed of an endothelium consisting of a single layer of lymphatic endothelial cells, a middle layer consisting of lymphatic muscle cells and elastin, and an outer layer of collagen, although mass fractions of these components may differ dramatically from arteries. Lymphatic endothelial cells provide similar function as vascular endothelial cells by producing NO in response to fluid shear stress on the endothelium and consequently reducing tonic contraction of the lymphatic muscle cells [124]. Lymphatic endothelial cells are also responsible for cell signaling that affects shear-induced rhythmic contraction, a function that does not exist in arteries. Lymphatic muscle cells exhibit complementary functions that are similar to vascular smooth muscle as well as skeletal muscle due to their ability to maintain tonic contraction and produce spontaneous

contraction, respectively [125]. Spontaneous contraction begins with pacemaker activity originating somewhere in the vessel wall and results from depolarization and sudden increases in intracellular calcium levels. Impairment of this function inhibits fluid flow along the lymphatic vasculature. Also found in the lymphatic vasculature is a system of one-way valves that facilitates forward flow of lymph. Following spontaneous contraction from the muscle cells, a proximal valve will close while the distal valve opens due to changes in pressure gradients across the valves, and a portion of the fluid in the vessel is consequently ejected. These valves are biased to stay open even in the face of a small negative pressure gradient [126], and it is therefore critical that contractions of lymphatic vessels be coordinated and timed such that backflow is minimized.

2.7 Lymphatics and cardiovascular disease

The lymphatic system has been suggested as a possible mediator of the progression of CVD [127]; however, direct evidence of its role is sparse. The transport of cholesterol from peripheral tissues to the bloodstream is thought to be a critical process that prevents the development of atherosclerotic plaques [128], and given the role of the lymphatic system in the transport of lipids, some investigators have hypothesized that the lymphatic vasculature plays a role in prevention of atherosclerosis. Indeed, one group has demonstrated a correlation between hypercholesterolemia and lymphatic dysfunction in mice [129], and the same group later demonstrated a direct role for the lymphatic vasculature in reverse cholesterol transport from the aortic wall in mice [130]. Lymphatic vessels and lymphangiogenic factors have been identified at sites of atherosclerosis [131, 132], and others have shown that aortic smooth muscle produces lymphangiogenic factors in a mouse model of atherosclerosis [133]. Similarly, other groups have suggested

that lymphatic obstruction plays a role in myocardial infarction. Studies have shown that experimental obstruction of cardiac lymphatics leads to interstitial edema [134], subendocardial edema and hemorrhage [135], increased cardiac collagen synthesis and tissue fibrosis [136], and reduced left ventricular contractility [137], while others have shown that increased cardiac lymph drainage reduces infarct risk area [138]. Despite these data, the role of lymphatic dysfunction in the development of CVD is still unclear and requires further investigation.

2.8 Lymphedema and lymphatic filariasis

Lymphedema is characterized by the inability of the lymphatic system to properly transport fluid from the peripheral tissues to the central venous system and subsequent edema and fibrosis of the tissue. Lymphedema can occur for multiple reasons, many of which are related to cancer treatment (e.g. axillary lymph node removal or sentinel node biopsy) [139]. Disruption of the lymphatic system following surgical excision of lymph nodes and neighboring lymphatic vessels triggers edema in the affected limb by mechanisms that are still relatively unknown. Treatment options for cancer-related lymphedema (generally following mastectomy) include simple compression therapy by which fluid transport is stimulated manually by massage or compression garments [140] as well as surgical techniques such as lymphaticovenous anastomosis [139].

Another significant contributor to lymphedema is parasitic infection of the lymphatic system, termed lymphatic filariasis. The World Health Organization estimates that over 120 million people are currently infected by the parasites that lead to lymphatic filariasis, and 40 million people are disfigured or incapacitated by lymphedema associated with the infection [4]. Lymphatic filariasis is transmitted via mosquitoes

whereby the worms are lodged in the lymphatic system following a mosquito bite. The worms live for 4-6 years and produce larvae that circulate in the blood. Lodging of the worms leads to lymphatic obstruction, and left untreated the obstruction can lead to lymphedema and ultimately a condition known as elephantiasis that is characterized by extreme disfigurement.

2.9 Regulation of lymphatic contractile function

Regulation of contractility in lymphatic vessels has many factors, but perhaps the most studied are the effects of the mechanical environment (e.g. pressure and flow) on metrics defining contractility. Metrics such as pumping frequency, contractile amplitude, and ejection fraction are commonly quantified as measures for comparison of contractile function in vessels. Many studies have shown that changes in pressure gradient have marked effects on such metrics. Studies investigating the role of elevated afterload have shown that creating a more negative pressure gradient triggers a clear decrease in contractile amplitude and stroke volume but an increase in pumping frequency [13]. Conversely, a study from the same group investigating preload showed that a more favorable pressure gradient has little effect on the contractile amplitude and only a slight decrease in ejection fraction [141]. In both cases, experiments were performed with both step changes in pressure gradient as well as continuous ramping of pressure gradient in order to compare differences. Lymphatic vessels have been shown to demonstrate transient changes in contractility following changes in intramural pressure [142], which motivates the need to compare step and ramp changes in pressure.

Independent of pressure gradient, the luminal pressure also directly affects contractile function of lymphatic vessels. Many have reported length-tension

relationships of lymphatics, and it has been well established that such behavior is quite heterogeneous based on location within the vasculature (i.e. thoracic duct vs. cervical lymphatics) [143-146]. One hypothesis explaining this phenomenon is that lymphatic vessels adapt to maximize their contractile force based on the local hydrostatic pressure conditions, although this hypothesis is unproven. Additionally, magnitude and direction of flow have also been implicated in the regulation of contractile activity. One study demonstrated that imposed flow reduces frequency depending on the magnitude of flow but not the direction and reduces contractile amplitude depending on the direction of flow but not the magnitude, and both responses were time-dependent [14]. These changes were attributed in part to changes in production of NO. Conversely, another study showed that imposed flow leads to a decrease in amplitude but an increase in contractile frequency [147]. However, this study was performed in lymphatic vessels from iliac lymph nodes, and given the regional heterogeneity established in other studies, the observed differences may simply be due to vessel type. Others have demonstrated contractile regulation based on flow generated from contractions rather than imposed flow. Gasheva et al. showed tonic relaxation in lymphatic vessels due to spontaneous contractions [124]. Aside from mechanical factors, there are other biological factors that may also play a role in contractile function including but not limited to the presence of metabolites [148], regulation of lipids [129], and muscle cell phenotype [149]. These data taken together suggest an extremely complex regulation of lymphatic contractility that demands further investigation in order to better understand lymphatic dysfunction and subsequent disease.

2.10 Mathematical modeling of lymphatic function

The ability to predict lymphatic contractile function and consequently bulk transport is key to understanding parameters affecting disease development. Consequently, many have developed predictive mathematical models attempting to capture the salient features of lymphatic function. The problem is inherently complex and requires considerations of both the solid mechanical properties of the tissue as well as the fluid dynamics of lymph transport through the lumen of these vessels. Investigations of the passive mechanical properties of the lymphatic vessel wall as well as the active tension generation have been performed in order to develop predictive models of the solid mechanical behavior [145, 150-153]. Other studies have modeled the bulk flow through vessels exclusively [154]. While a select few of these studies investigated only the solid or fluid mechanical properties specifically, many of them sought to incorporate both properties into one model, hereafter referred to as a fluid-structure interaction (FSI) model. These models have taken on various forms, some focusing on transport through the lumen and neglecting contribution of the valves [151, 155], others have focused specifically on flow across valves [156, 157], and still others incorporate valve behavior into a model of bulk flow through one or multiple lymphangions [152, 158-160]. Many of these models have been powerful steps forward in our characterization of lymphatic function; however, the models all contain simplifications that limit their predictive power. The solid mechanics considerations are often empirical, and those that are not still neglect the non-linear, anisotropic behavior that is characteristic of most soft tissue. The fluid mechanics in some cases neglect the inertial forces experienced during fluid transport, and those that do assume unidirectional and fully-developed flow, which may

overlook important minutiae in fluid behavior. Finally, valve behavior has been shown to be highly complex [126], and almost all models have dramatic simplifications of valve behavior, with the notable exception of a study from Bertram et al. which incorporates a tedious study of valve behavior into an FSI model [160]. Regardless of simplifying assumptions, these models are critical tools for furthering our understanding of the complex mechanical environment in the lymphatic vasculature.

CHAPTER 3

THE ROLE OF EFAVIRENZ IN DEVELOPMENT OF MECHANICALLY-MEDIATED VASCULAR REMODELING

3.1 Introduction

Since the advent of highly active antiretroviral therapy (HAART), patients infected with HIV-1 are living longer lives. The World Health Organization reports that over 35 million people worldwide were living with HIV-1 as of 2012 [161]. Consequently, co-morbidities associated with HIV-1 infection and treatment have become a prevalent issue. Indeed, non-AIDS related comorbidities associated with cardiovascular disease (CVD) including myocardial infarction [43, 44, 162], atherosclerotic lesions [45-47], and other subclinical markers of atherosclerosis are widely reported among HIV-infected populations.

A pressing need remains to better quantify non-AIDS related co-morbidities in people living with HIV in sub-Saharan Africa. Most studies of cardiovascular co-morbidities with HIV represent populations from developed countries; yet, 69% of all people living with HIV reside in sub-Saharan Africa. Antiretroviral programs in Africa have made a tremendous impact in reducing HIV-related deaths and have been available in Ethiopia since 2005; the treatment disparities, however, between the developing world and the developed world remain great. People living with HIV in the developing world have access to fewer combinations of HAART regimens and patient adherence and clinical monitoring of CD4+ cell counts and viral loads in the developing world is well below that in the developed countries. As a result, people living with HIV in developing nations remain on first line therapy with less follow up. These treatment disparities,

combined with differences in demographics, lifestyle, and nutritional status between Ethiopian and Western populations, may make this population more susceptible to non-AIDS related co-morbidities.

The individual roles of HIV-1 infection and HAART treatment in the progression of atherosclerosis are not well understood. Some studies have implicated the viral infection as a singular cause of CVD, demonstrating coronary arteriopathy and atherosclerotic lesions following post-mortem analysis of HAART-naïve HIV-1+ patients [54, 55], and many laboratory studies have implicated HIV-1 proteins in preclinical markers of atherosclerosis and vascular dysfunction [56-59]. Conversely, a multitude of studies have shown accelerated progression of atherosclerosis in HAART-treated patients compared to HAART-naïve patients, suggesting an additive role of the drugs in disease progression. Azidothymidine (AZT) has been shown to cause arterial stiffening [12, 48, 49], cardiomyopathy [163, 164], and endothelial dysfunction [80, 165, 166]. Similarly, endothelial dysfunction has been associated with use of protease inhibitors (PIs) via mitochondrial dysfunction, oxidative stress, and ROS [79, 167, 168]. PIs are also known to cause an increase in cIMT [169] as well as impairment of FMD [53, 170], but these results are controversial due to conflicting evidence [61, 92, 93, 171, 172].

While NRTIs and PIs have both been implicated in the development of preclinical markers of CVD, there remains much information to be discovered regarding the contributions of non-nucleoside reverse transcriptase inhibitors (NNRTIs), specifically efavirenz (EFV), to the progression of CVD in HIV-1 infection. Clinical studies have shown that NNRTI-containing regimens are associated with increased markers of CVD, particularly alterations of lipid profiles, but have less pronounced changes than those of

PI-containing regimens [173, 174]. More recently, EFV was implicated in worsening endothelial function over time [9]. In laboratory studies, EFV has been associated with increased production of reactive oxygen species and endothelial dysfunction [8] as well as progressive mitochondrial dysfunction and associated changes in lipid levels [10, 11]. Conflicting data should be noted as another study has shown transient increases in cholesterol efflux with EFV treatment, suggesting a beneficial effect in the prevention of atherosclerosis [175]. In general, clinical data and the majority of laboratory data seem to suggest a role of EFV in the progression of subclinical markers of CVD.

The role of mechanics in the development of CVD has been well characterized. Arterial stiffening is a commonly used preclinical marker of atherosclerosis and is commonly seen in HIV-1+ populations [49, 176]. However, given the combination treatment regimen that these patients receive, it is difficult to parse out the roles of individual drugs in development of CVD, thus making laboratory studies of significant use. Additionally, laboratory studies offer the opportunity for additional endpoints for quantification of CVD development beyond the possible clinical endpoints. Alteration of axial force behavior is one such indicator [177, 178]. Indeed, previous laboratory studies from our lab investigating the role of AZT in the progression of CVD report changes in axial force generation in addition to the stiffening normally observed in the circumferential direction [12] while other studies have reported axial changes that precede circumferential stiffening [179]. Thus, utilization of an animal model offers the opportunity to identify contributions of EFV to the development of CVD without interference from drug-drug interaction and with higher sensitivity than standard clinical measurements.

Taken together, it seems clear that a pressing need exists to quantify the role of EFV in the progression of atherosclerosis. The purpose of this paper is to demonstrate the role of EFV in the development of subclinical markers of atherosclerosis including arterial stiffening and geometric changes as well as early onset plaque development. We utilized a common mouse model of atherosclerosis to quantify these tissue level changes with long-term administration of EFV in order to provide direction for future studies surrounding EFV use in the context of HIV treatment.

3.2 Hypothesis 1: Treatment with EFV will be associated with accelerated markers of CVD in HIV-1+ adult[1] and pediatric[2] Ethiopian patients

To test this hypothesis, adult Ethiopian HIV-1-negative, HIV-1-positive / HAART-naïve, and HIV-1-positive / HAART-treated patients as well as pediatric Ethiopian HIV-1-positive / HAART-naïve, and HIV-1-positive / HAART-treated patients were recruited and evaluated for arterial stiffening using pulse wave velocity and pulse wave analysis using applanation tonometry as well as increased carotid intima-media

---

[1] Gleason RL, Caulk AW, Seifu D, Parker I, Vidakovic B, Getenet H, Assefa G, Amogne W (2015). Current efavirenz (EFV) or ritonavir-boosted lopinavir (LPV/r) use correlates with elevated markers of atherosclerosis in HIV-infected subjects in Addis Ababa, Ethiopia. PLoS ONE, 10(4): e0117125. doi:10.1371/journal.pone.0117125.

[2] Gleason RL, Caulk AW, Rosebush J, Seifu D, Shapiro A, Schwartz M, Ross-Eckard A, Taye WA. HAART use correlates with elevated markers of atherosclerosis in pediatric HIV-infected subjects in Addis Ababa, Ethiopia. Submitted to J Pediatric Infectious Disease Society.

thickness and impaired flow-mediated dilation using non-invasive ultrasound. The goal of testing this hypothesis is to investigate the role of a frequently prescribed antiretroviral in the development of a common non-AIDS-related comorbidity and shed light on possible differences of HAART treatment in an understudied population of HIV-infected patients.

3.2.1 Methods and Materials[3]

3.2.1.1 Participant enrollment and baseline data

All work was performed in accordance with the Declaration of Helsinki. All participants provided written informed consent and this study was approved by the Institutional Review Board Committees at Addis Ababa University and Georgia Institute of Technology. Eighteen- to 65-year-old HIV-negative, HIV-positive HAART naïve, and HIV-positive subjects on EFV-, NVP-, or LPV/r-containing regimens for at least two months prior to the exam were recruited from Tikur Anbessa (Black Lion) Specialized Referral Hospital in Addis Ababa, Ethiopia to participate in this study. Six- to 17-year-old subjects who were vertically infected with HIV and HAART naïve or taking EFV-, NVP-, or LPV/r-containing HAART regimens for at least two months prior to the exam

---

[3] AWC was responsible for analysis of cIMT data, FMD data, and worked with IKP on quantification and analysis of inflammatory blood markers. RLG collected and analyzed PWA and PWV data, collected all ultrasound data, oversaw collection of anthropometric and metabolic data, and performed all statistical analyses.

were also recruited. Note that 99% of the pediatric HAART-treated subjects were on therapy for 6 months or more and 95% were on therapy for more than 1 year. For subjects between 6 and 11 years of age, written informed consent was obtained from the parent or guardian of the participant and for subjects between 12 and 17 years of age, written informed consent was obtained from both the participant and the parent or guardian of the participant. Subjects were excluded if they had active AIDS defining illnesses or diabetes mellitus. Subjects fasted and refrained from tobacco products for at least 8 hours prior to the test and refrained from exercise in the morning of the test.

Participant age, sex, HIV-serostatus, date of first HIV-seropositive test, initial CD4+ cell count, last CD4+ cell count, and any viral load determinations, and date of initiation of current and all previous HAART regimens were obtained from the participants hospital card. Questionnaire-driven interviews were performed by the local recruiting nurse at the Black Lion Hospital HIV clinic under the direction of the research team. Self-reported personal and familial (mother, father, brothers, or sisters) history of heart attack, angina, stroke, kidney disease, diabetes, or lipid disorders and self-reported alcohol and cigarette use were recorded.

3.2.1.2 Body composition

Body weight, body height, waist and hip circumference, and skinfold thickness (bicep, tricep, suprailiac, and sub scapula) were measured. Skinfold measurements were taken in in duplicate on the right and left sides and reported as the average of these four values. The ratio of the sum of skin-fold measurements in the suprailiac and sub-scapula divided by the sum of those from the bicep and tricep was reported as the Trunk/arm ratio. Adult subjects were asked if they observed an ‘increase in fat’, ‘decrease in fat’, or

'no change' at each of the following locations: face, arms, legs, abdomen, chest, cervical fat pad, supraclavicular fat, and across their entire body.

3.2.1.3 Blood pressure, pulse wave analysis, and pulse wave velocity

Brachial artery systolic (B-SBP) and diastolic (B-DBP) blood pressure were measured with a digital automatic blood pressure measurement device after the subjects rested in a supine position for at least 10 minutes. Pulse wave analysis (PWA) and pulse wave velocity (PWV) measurements were subsequently taken with a SphygmoCor CPV Clinical System (AtCor Medical) following manufacturer protocol. PWA and PWV measurements meeting the manufacturer quality control criteria were collected in triplicate and averaged.

3.2.1.4 Carotid intima-media thickness

Ultrasound measurements were collected using a Sonocyte Micromax portable ultrasound device with vascular software for two-dimensional imaging, color and spectral Doppler, high- frequency (10 MHz) linear transducer, and internal electrocardiogram monitor. The right and left common carotid arteries (CCA) were examined with the head in the midline position tilted slightly upward and away from the artery being imaged. The probe was placed so that the near and far walls were parallel in the acquired image and lumen diameter was maximized in the longitudinal plane. Three 6-second clips of each artery were collected and stored for analysis. cIMT was reported in systole and diastole as the average of the near and far wall measurements from three separate clips from both the right and left CCA. Given subject-to-subject variability in the carotid artery size, a normalized measure was defined as $\mathrm{cIMT}^{\mathrm{norm}} = \mathrm{cIMT}/(D/2)$, where D was the measured inner diameter of the CCA.

The linearized cyclic strain $\Delta\varepsilon = \Delta D/D$, was also reported, where ΔD is the difference between the systolic and diastolic luminal diameter and D is the diastolic luminal diameter. The Peterson's modulus (E_p), a common measure of arterial stiffness, defined as $E_p = \frac{PP}{\Delta\varepsilon} = 1/C$, where PP is the pulse pressure and C is the compliance, was reported. The medial hoop stress approximated as $\sigma_\theta = P(\frac{D}{2})/(\text{cIMT}) = P/\text{cIMT}^{\text{norm}}$, was also reported. P and PP in the carotid artery were approximated by the values determined for the aorta via PWA. A single analyst, blinded to the patients HIV status and HAART regimen, analyzed all images from adult patients. Three analysts, blinded to the patients HIV status and HAART regimen, analyzed all images from pediatric patients.

3.2.1.5 Flow-mediated dilation

An appropriately sized sphygmomanometer was placed on the widest part of the proximal right forearm ~1 cm distal to the antecubital fossa. Prior to inflation, three 6-second clips of the brachial artery image and EKG tracings were stored for baseline measurements. The sphygmomanometer was inflated at least 50 mmHg above the subjects' systolic blood pressure. Five minutes after occlusion, the cuff was deflated and a 6-second clip of the brachial artery image and EKG tracing was stored at 30, 45, 60, 75, and 90 seconds after deflation. A single analyst, blinded to the patients HIV status and HAART regimen, analyzed all images from adult patients. Three analysts, blinded to the patients HIV status and HAART regimen, analyzed all images from pediatric patients. Further, $FMD = (D_t - D_B)/D_B$, where D_t is the brachial artery inner diameter during diastole at the time-point of interest and D_B is the average of the three measurements of the brachial artery diameter during diastole at baseline.

3.2.1.6 Blood sample analysis

Complete blood count, total cholesterol (TC), triglyceride (TG), high-density lipoprotein cholesterol (HDL), low-density lipoprotein cholesterol (LDL), and glucose analysis were performed at the clinical laboratory at Black Lion Hospital. CD4+ cell count and plasma HIV RNA analysis was performed at the International Clinical Laboratory (Addis Ababa, Ethiopia). In adult patients, high-sensitivity C-reactive protein (hsCRP), soluble vascular cell adhesion molecule-1 (sVCAM-1) and intercellular adhesion molecule-1 (sICAM-1), and leptin analyses were performed on blood serum using commercially available ELISA kits (Life Technologies Corporation). Analysis for HIV viral load was performed on 70%, hsCRP on 80%, sVCAM-1 on 85%, sICAM-1 on 80%, and leptin on 80% of the adult subject pool, equally distributed among groups.

3.2.1.7 Statistical analysis

All statistical analyses were performed using MATLAB© (MathWorks). A one-way analysis of variance (ANOVA) was performed to determine statistical significance across groups ($p < 0.05$) on continuous variables that satisfied Bartlett's test for equal variances and Pearson Chi-square test for normality of residuals; a Kruskal-Wallis non-parametric one-way ANOVA was performed on continuous variables that did not show equal variances or normality. For continuous variables with significance across groups, a pairwise Wilcoxon rank sum test was performed to detect differences between individual groups ($p < 0.05$). For categorical variables, χ^2 analysis was performed to determine statistical significance across groups ($p < 0.05$); for those with significance across groups, a pairwise Marascuillo procedure was performed to compare differences in proportions between individual groups ($p < 0.05$).

Correlation analysis was performed and multivariable linear regression models were constructed to examine the association of study parameters with PWV for all HAART-treated subjects. Relevant study parameters were selected for the inclusion of the initial models and the `stepwisefit` multivariable regression MATLAB subroutine, which eliminates (or adds) covariates in a stepwise fashion, was used with the criteria $p<0.05$ for removal from (or inclusion in) the final model.

3.2.2 Results

3.2.2.1 Participant characteristics

Adult population: CD4+ cell count was lower in all HIV-positive groups, compared to HIV-negative subjects, and lower in LPV/r-treated, compared to NVP-treated subjects (Table 3.1). Plasma HIV RNA levels were lower and percentages of subjects with plasma HIV RNA levels below detectable limits (<40 copies/mL) were higher in all HAART-treated groups, compared to HAART-naïve subjects. Years since first HIV diagnosis was higher in HAART-treated groups compared to HAART-naïve and in NVP- and LPV/r-treated compared to EFV-treated subjects. LPV/r-treated subjects were on HAART longer than EFV-treated subjects. EFV-treated subjects have been on their current regimen longer than LPV/r-treated, but shorter than NVP-subjects. The HAART treated groups had similar distributions of NRTI-backbone, with the exceptions that less LPV/r-treated subjects had an AZT-3TC backbone compared to NVP-treated subjects and more LPV/r-treated subjects had an NRTI-backbone other than AZT-3TC or TDF-3TC compared to EFV-treated subjects. The 'Other' NRTI backbones included stavudine in the NNRTI groups and didanosine, abacavir, or stavudine in the LPV/r

group. More LPV/r-treated subjects had taken a previous regimen, which was expected, as LPV/r is considered a second-line regimen.

Table 3.1. Baseline characteristics and body composition metrics for HIV-1-negative, HIV-1-positive HAART-naïve, and HIV-1-positive HAART-treated adults. Continuous variables are reported as median (interquartile range). A, a = $p<0.005$ or $p<0.05$ versus HIV-negative controls, respectively; B, b = $p<0.005$ or $p<0.05$ versus HAART-naive, respectively; D, d = $p<0.005$ or $p<0.05$ versus EFV, respectively; E, e = $p<0.005$ or $p<0.05$ versus NVP, respectively.

End-point	HIV-Negative (n= 36)	HAART Naïve (n= 51)	Efavirenz (EFV) (n= 91)	Nevarapine (NVP) (n= 95)	Lopinavir/r (LPV/r) (n= 44)
Demographics					
Age (yrs)	**39** (29 - 45)	**38** (32 - 45)	**38** (34 - 45)	**37** (32 - 42)	**39** (35 - 44)
Male ratio [# (%)]	**8** (22%)	**14** (27%)	**23** (25%)	**21** (22%)	**14** (32%)
HIV / HAART History					
CD4+ count	**730** (656 - 1047)	**395** (182 - 546) [A]	**349** (232 - 481) [A]	**390** (271 - 534) [A]	**285** (147 - 453) [A,e]
Viral Load (log_{10}copies/mL)	--	**3.6** (2.2 - 4.7)	**<1.6** (<1.6 - <1.6) [B]	**<1.6** (<1.6 - <1.6) [B]	**<1.6** (<1.6 - <1.6) [B]
Viral Load (% BDL)	--	**18%**	**92%** [B]	**87%** [B]	**81%** [B]
Yrs since diagnosis	--	**1.6** (0.3 - 3.7)	**5.7** (3.4 - 7.0) [B]	**6.0** (5.6 - 7.4) [B,d]	**6.5** (5.3 - 8.3) [B,d]
Yrs on HAART	--	--	**5.0** (3.2 - 6.2)	**5.7** (3.9 - 6.2)	**5.9** (4.2 - 6.8) [d]
Yrs on Current Regimen	--	--	**2.5** (1.5 - 4.4)	**3.8** (1.9 - 5.7) [d]	**1.8** (0.7 - 3.2) [E]
Current NRTI backbone					
TDF+3TC [# (%)]	--	--	**55** (60%)	**38** (40%)	**28** (64%)
AZT+3TC [# (%)]	--	--	**35** (38%)	**53** (56%)	**7** (16%) [E]
Other [# (%)]	--	--	**1** (1%)	**4** (4%) [e]	**9** (20%)
Previous Regimen					
All [# (%)]	--	--	**39** (43%)	**29** (31%)	**40** (91%) [D,E]
EFV-containing [# (%)]	--	--	**24** (26%)	**5** (5%)	**20** (45%) [d,e]
NVP-containing [# (%)]	--	--	**15** (16%)	**24** (25%)	**22** (50%) [d,e]
Body Composition					
BMI [kg/m^2]	**22** (20 - 26)	**22** (20 - 26)	**21** (19 - 24)	**23** (20 - 25)	**22** (18 - 25)
WHR [ ]	**0.82** (0.77 - 0.86)	**0.84** (0.79 - 0.89)	**0.86** (0.81 - 0.91) [A]	**0.86** (0.81 - 0.92) [A]	**0.88** (0.82 - 1) [A,b]
Skinfold Thickness					
Tricep [mm]	**12.2** (7.6 - 15.3)	**10.8** (5.4 - 14.9) [A]	**6.7** (3.9 - 9.5) [A,B]	**6.7** (4.2 - 10.0) [A,b]	**8.0** (5.2 - 10.6) [A]
Bicep [mm]	**6.1** (3.3 - 8.8)	**6.2** (3.1 - 9.2)	**3.1** (2.4 - 5.8) [A,B]	**3.5** (2.4 - 6.0) [A,B]	**4.4** (2.7 - 8.1)
Suprailiac [mm]	**9.3** (6.4 - 13.7)	**7.9** (5.0 - 13.1)	**6.2** (4.0 - 8.9) [A,b]	**7.4** (4.3 - 10.9) [A]	**7.7** (4.0 - 12.4)
Sub-scapula [mm]	**20.9** (16.0 - 27.1)	**19.8** (11.7 - 28.4)	**15.8** (9.9 - 20.7) [a,b]	**18.4** (11.2 - 28.2) [d]	**20.2** (9.8 - 30.4) [d]
Trunk:arm [ ]	**1.6** (1.4 - 2.0)	**1.8** (1.4 - 2.2)	**2.1** (1.4 - 2.8) [a,b]	**2.2** (1.5 - 3.3) [a,b]	**2.1** (1.5 - 2.6) [a,b]
Observed change in fat (% observing decrease in fat / % observing increase in fat)					
Face [%]	**0%** / **0%**	**8%** / **4%**	**27%** [A,b] / **5%**	**15%** [A] / **23%** [A,b,d]	**36%** [A,b] / **11%**
Arms [%]	**0%** / **0%**	**4%** / **4%**	**16%** [A] / **4%**	**8%** / **13%** [A]	**23%** [A] / **7%**
Legs [%]	**0%** / **0%**	**6%** / **2%**	**22%** [A] / **5%**	**17%** [A] / **20%** [A,b]	**25%** / **7%**
Abdomen [%]	**0%** / **0%**	**4%** / **6%**	**1%** / **32%** [A,B]	**1%** / **29%** [A,B]	**2%** / **41%** [A,B]
Chest [%]	**0%** / **0%**	**4%** / **0%**	**2%** / **11%** [a,b]	**1%** / **9%** [a,b]	**0%** / **25%** [a,b]
Buffalo hump [%]	**0%** / **0%**	**4%** / **0%**	**1%** / **7%**	**0%** / **9%** [a,b]	**2%** / **14%**
Neck [%]	**0%** / **0%**	**4%** / **0%**	**3%** / **5%**	**0%** / **8%**	**2%** / **16%**
Body [%]	**0%** / **8%**	**20%** [a] / **14%**	**14%** [A] / **32%** [a]	**13%** [a] / **42%** [A,B]	**16%** / **36%**

Less than 3% of the participants in any group reported being current cigarette smokers and less than 6% of the participants in any group report drinking more than 4 drinks per week. Less than 10% and 15% of the subjects from any group reported a family history and personal history, respectively, of heart attack, angina, or stroke, kidney disease, diabetes, or lipid disorders.

Pediatric population: CD4+ cell count was higher in NVP-treated subjects compared to HAART-naïve and EFV-treated subjects, and EFV-treated, compared to HAART-naive subjects (Table 3.2). LPV/r-treated subjects were on HAART longer than EFV- and NVP-treated subjects and EFV-treated subjects were on HAART longer than NVP-treated subjects. LPV/r-treated subjects were on their current regimen for a shorter period than EFV-treated subjects. The EFV- and NVP-treated subjects had similar distributions of NRTI-backbone, with a majority of subjects taking zidovudine (AZT) + lamivudine (3TC) or stavudine (d4T) + 3TC. The majority of LPV/r-treated subjects had an NRTI backbone of abacavir (ABC) + didanosine (ddI). The 'Other' NRTI backbones for the EFV- and NVP-treated subjects were tenofovir (TDF) + 3TC (*n*=4) and ABC + 3TC (*n*=3). The 'Other' NRTI backbone for the LPV/r-treated subjects was ABC+3TC.

3.2.2.2 Body composition and anthropometric measurements

Adult population: No differences were observed in BMI across groups. WHR was elevated in all HAART-treated groups, compared to HIV-negative subjects and in the LPV/r-treated subjects compared to HAART-naïve subjects. Skin-fold thickness measurements yielded multiple differences between HAART treated versus HIV-negative and HAART-naïve subjects. Trunk/Arm skin-fold thickness ratio was significantly higher in all HAART-treated subjects compared to HIV-negative and HAART-naïve subjects. The self-reported fat redistribution followed these trends, with HAART-treated subjects generally reporting decreased fat in their face, arms, and legs, increased fat in the chest, buffalo hump, and neck and increased overall body fat. A significant fraction of NVP-treated subjects also reported increased fat in their face, arms, and legs. Taken together,

WHR, skin-fold thickness measurements, and self-reported observations show that adult HAART-treated subjects in Addis Ababa, Ethiopia exhibit lipodystrophy.

Pediatric population: No differences were observed in BMI or WHR across groups. Bicep skin-fold thickness measurements were lower in EFV- and NVP-treated subjects compared to HAART-naïve subjects.

Table 3.2. Cardiovascular metrics for HIV-1-negative, HIV-1-positive HAART-naïve, and HIV-1-positive HAART-treated pediatric patients. Continuous variables are reported as median (interquartile range). A, a = $p<0.005$ or $p<0.05$ versus HIV-negative controls, respectively; B, b = $p<0.005$ or $p<0.05$ versus HAART-naive, respectively; D, d = $p<0.005$ or $p<0.05$ versus EFV, respectively; E, e = $p<0.005$ or $p<0.05$ versus NVP, respectively.

	HAART Naïve (n = 45)		Efavirenz (EFV) (n = 90)		Nevarapine (NVP) (n = 80)		LPV/r (n = 19)	
Demographics								
Age (yrs)	11 (9 - 14)		13 (10 - 15)		11 (9 - 14)		13 (11 - 15)	
Male ratio [# (%)]	20 (44%)		41 (46%)		40 (50%)		12 (63%)	
Body Composition								
BMI (kg/m^2)	16 (15 - 18)		16 (14 - 18)		16 (15 - 18)		16 (15 - 18)	
WHR ( )	0.85 (0.82 - 0.90)		0.85 (0.82 - 0.89)		0.87 (0.83 - 0.91)		0.87 (0.85 - 0.90)	
Skinfold Thickness (mm)								
Tricep	5.7 (3.8 - 7.2)		5.0 (3.6 - 6.4)		4.7 (4.0 - 6.2)		4.3 (3.5 - 7.1)	
Bicep	3.1 (2.6 - 4.0)		2.7 (2.1 - 3.6)	a	2.6 (2.1 - 3.3)	A	3.1 (2.4 - 4.8)	
Suprailiac	3.1 (2.4 - 4.2)		3.3 (2.4 - 4.7)		3.1 (2.4 - 4.0)		3.3 (2.8 - 3.9)	
Sub-scapula	6.0 (4.0 - 7.4)		6.2 (4.3 - 9.7)		5.3 (4.0 - 6.7)		5.0 (4.5 - 6.6)	
Trunk:arm	1.0 (0.8 - 1.3)		1.2 (1.0 - 1.6)		1.1 (0.9 - 1.5)		1.0 (0.9 - 1.3)	
HIV / HAART History								
Current CD4+ count	456 (378 - 608)		575 (412 - 744)	a	639 (460 - 902)	A,b	554 (336 - 776)	
Yrs on HAART			4.5 (3.0 - 5.7)		3.4 (1.8 - 5.5)	b	6.1 (5.5 - 6.3)	B,C
Yrs on Current Regimen			4.2 (2.3 - 5.4)		3.1 (1.7 - 5.5)		3.1 (2.0 - 3.6)	b
Current NRTI backbone								
d4T+3TC [# (%)]	--		33 (37%)		31 (39%)		2 (11%)	
AZT+3TC [# (%)]	--		51 (57%)		48 (60%)		1 (5%)	
ABC+DDI [# (%)]			0 (0%)		0 (0%)		15 (79%)	
Other [# (%)]	--		6 (7%)		1 (1%)		1 (5%)	
Cardiovascular Metrics								
Heart Rate (bpm)	81 (71 - 89)		81 (73 - 87)		82 (74 - 91)		69 (65 - 87)	
Brachial Artery SBP (mmHg)	103 (96 - 108)		100 (93 - 108)		100 (94 - 107)		105 (99 - 111)	
Brachial Artery DBP (mmHg)	62 (58 - 71)		61 (56 - 67)		63 (59 - 68)		63 (57 - 73)	
Brachial Artery MP (mmHg)	76 (72 - 82)		74 (69 - 80)		76 (72 - 80)		78 (72 - 83)	
Brachial Artery PP (mmHg)	38 (32 - 43)		38 (33 - 44)		37 (30 - 43)		41 (34 - 46)	
Pulse Wave Velocity (m/s)	4.6 (4.1 - 5.0)		4.7 (4.3 - 5.3)		4.6 (4.2 - 5.1)		5.2 (4.6 - 5.9)	a,b,C
Flow-Mediated Dilation (%)	8.6 (5.4 - 13.6)		6.4 (4.1 - 10.0)		7.9 (4.1 - 12.1)		9.6 (5.0 - 12.2)	
cIMT (microns)	45 (42 - 47)		45 (43 - 48)		46 (42 - 50)		47 (45 - 51)	
Modulus (kPa)	35 (29 - 42)		38 (30 - 45)		38 (28 - 45)		43 (32 - 51)	
Laboratory Analysis								
Metabolic Parameters								
Glucose (mg/dL)	83 (76 - 87)		86 (79 - 92)	a	82 (77 - 87)	b	81 (74 - 86)	
TC (mg/dL)	128 (110 - 157)		161 (134 - 186)	A	157 (135 - 183)	A	199 (173 - 244)	A,B,C
TG (mg/dL)	90 (71 - 135)		104 (76 - 143)		99 (80 - 127)		146 (120 - 249)	A,B,C
HDL-c (mg/dL)	37 (33 - 42)		45 (40 - 52)	A	48 (43 - 55)	A	40 (33 - 50)	c
LDL-c (mg/dL)	70 (59 - 94)		97 (70 - 111)	A	91 (75 - 115)	A	144 (98 - 174)	A,B,C
TC:HDL	3.8 (3.1 - 4.1)		3.5 (3.1 - 4.3)		3.2 (2.7 - 4.1)		4.8 (3.7 - 6.1)	A,B,C

3.2.2.3 Blood pressure, pulse wave analysis, and pulse wave velocity

Adult population: The B-SBP was lower in EFV-treated compared to NVP-treated subjects and brachial artery pulse pressure (PP) was lower in EFV-treated compared to NVP- and LPV/r-treated subjects (Table 3.3). PWA predicted that the aortic PP was higher in the NVP- and LPV/r-treated compared to the HAART-naïve and EFV-treated subjects; aortic PP was higher in HIV-negative compared to HAART-naïve subjects. PWV was significantly lower in NVP-treated compared to EFV-treated and LPV/r-treated subjects, indicating arterial stiffening of the central vasculature (Figure 3.1). No differences were observed in SBP, DBP, MP, or PP across pediatric groups.

Pediatric population: No differences were observed in SBP, DBP, MP, or PP across groups. PWV was significantly higher in LPV/r-treated subjects compared to all other groups.

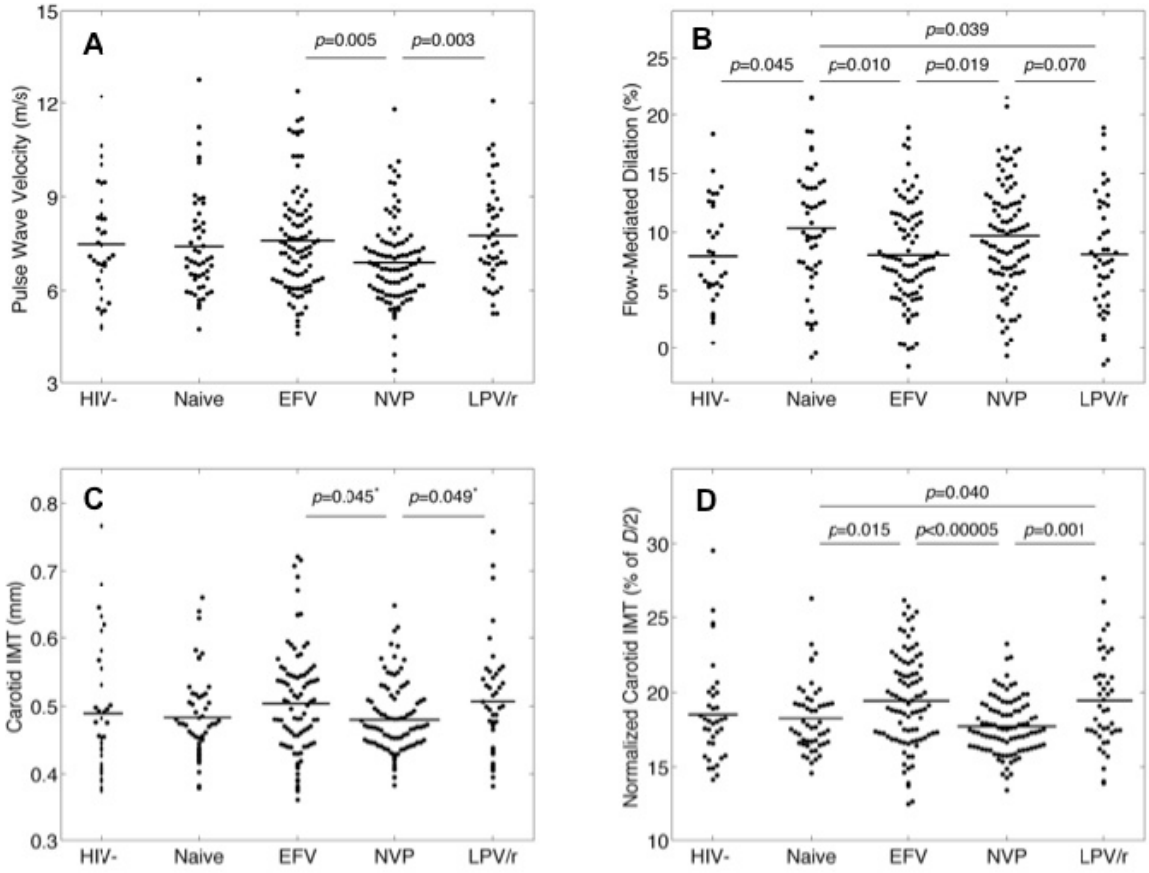

Figure 3.1. Preclinical markers of atherosclerosis are elevated in EFV-treated and LPV/r-treated adult subjects compared to HAART-naïve and NVP-treated. Wilcoxon rank sum test *p*-values are shown. *Note: Although the pairwise Wilcoxon rank sum test showed differences in cIMT between EFV- and LPV/r-treated and NVP-treated subject, ANOVA yielded a $p=0.12$, which is above the defined criteria of $p<0.05$ for statistical significance. When normalized to carotid artery diameter ($cIMT^{norm} = cIMT/(D/2)$, where D = carotid diameter), EFV- and LPV/r-treated subjects exhibited significantly increased values compared to NVP-treated and HAART-naïve subject.

3.2.2.4 Flow-mediated dilation

Adult population: The peak FMD was observed at 60 seconds post-occlusion (not shown). FMD at 60 seconds post-occlusion was reduced in EFV-treated and LPV/r-treated compared to HAART-naïve subjects and in EVF-treated compared to NVP-treated subjects.

Pediatric population: The peak FMD was observed at 60 seconds post-occlusion (not shown). FMD was similar across groups.

3.2.2.5 Carotid artery geometry and properties

Adult population: The carotid artery diameter was smaller in NVP- compared to EFV- and LPV/r-treated subjects, both in diastole and systole. No significant differences in the cIMT were observed across groups. When normalized to diameter, however, $cIMT^{norm}$ was significantly increased in EFV- and LPV/r-treated compared to NVP-treated and HAART-naïve subjects. The medial stress was lower in EFV- and LPV/r-treated compared to NVP-treated subjects and lower in EFV-treated compared to HIV-negative and HAART-naïve subjects. No differences were observed in the Peterson's modulus, compliance, or cyclic strain over the cardiac cycle across adult groups.

Pediatric population: No differences were observed in cIMT. No differences were detected in the Peterson modulus, compliance (not shown), or the distensibility or compliance coefficients (not shown) over the cardiac cycle across groups.

Table 3.3. Cardiovascular metrics for HIV-1-negative, HIV-1-positive HAART-naïve, and HIV-1-positive HAART-treated adults. Continuous variables are reported as median (interquartile range). A, a = p<0.005 or p<0.05 versus HIV-negative controls, respectively; B, b = p<0.005 or p<0.05 versus HAART-naive, respectively; D, d = p<0.005 or p<0.05 versus EFV, respectively; E, e = p<0.005 or p<0.05 versus NVP, respectively.

End-point	HIV-Negative (n= 36)	HAART Naïve (n= 51)	Efavirenz (EFV) (n= 91)	Nevarapine (NVP) (n= 95)	Lopinavir/r (LPV/r) (n= 44)
Cardiovascular Metrics					
Heart Rate	**66** (64 - 74)	**72** (65 - 79)	**70** (65 - 78)	**71** (65 - 78)	**69** (63 - 73)
Blood Pressure					
Brachial SBP [mmHg]	**120** (112 - 132)	**112** (108 - 123)	**112** (104 - 123) [a]	**117** (107 - 130) [d]	**119** (105 - 131)
Brachial DBP [mmHg]	**73** (68 - 81)	**70** (66 - 79)	**71** (63 - 78)	**72** (67 - 82)	**70** (66 - 79)
Brachial MP [mmHg]	**90** (83 - 99)	**85** (82 - 95)	**86** (78 - 95)	**89** (82 - 99)	**90** (80 - 101)
Brachial PP [mmHg]	**46** (40 - 54)	**43** (37 - 49)	**42** (38 - 46) [a]	**45** (39 - 52) [d]	**45** (38 - 56) [d]
Pulse Wave Analysis					
Aortic SBP [mmHg]	**110** (101 - 121)	**103** (98 - 114)	**103** (96 - 113)	**109** (98 - 122)	**112** (97 - 123)
Aortic DBP [mmHg]	**75** (69 - 82)	**71** (67 - 81)	**72** (64 - 79)	**73** (68 - 83)	**71** (67 - 81)
Aortic MP [mmHg]	**90** (83 - 98)	**85** (82 - 95)	**86** (78 - 95)	**89** (82 - 99)	**90** (80 - 101)
Aortic PP [mmHg]	**34** (30 - 42)	**32** (26 - 38)	**31** (28 - 36) [a]	**34** (29 - 42) [b,d]	**34** (31 - 47) [b,d]
AP [mmHg]	**8** (5 - 13)	**8** (6 - 14)	**8** (5 - 11)	**10** (6 - 14)	**10** (6 - 16)
Aix	**27** (15 - 34)	**25** (20 - 35)	**26** (20 - 33)	**27** (20 - 35)	**28** (21 - 38)
AIx-75	**26** (12 - 33)	**25** (19 - 35)	**26** (17 - 32)	**27** (19 - 33)	**28** (19 - 34)
Pulse Wave Velocity [m/s]	**7.1** (6.3 - 8.4)	**7.0** (6.3 - 8.2)	**7.4** (6.3 - 8.4)	**6.8** (6.0 - 7.5) [D]	**7.4** (6.8 - 8.7) [E]
Baseline Diameter [mm]	**3.04** (2.83 - 3.40)	**2.87** (2.63 - 3.19)	**2.98** (2.75 - 3.26)	**3.07** (2.81 - 3.41)	**2.88** (2.69 - 2.69)
Dilated Diameter [mm]	**3.29** (3.07 - 3.56)	**3.22** (2.94 - 2.94)	**3.22** (2.99 - 3.51)	**3.33** (3.07 - 3.76)	**3.20** (2.91 - 2.91)
FMD [%]	**6.5** (5.0 - 12.4)	**10.0** (7.0 - 13.9) [a]	**7.7** (4.8 - 11.2) [b]	**9.2** (6.6 - 12.5) [d]	**7.6** (4.5 - 12.2) [b]
Common Carotid Artery					
Diameter [mm]	**5.17** (4.94 - 5.52)	**5.27** (5.02 - 5.58)	**5.16** (4.92 - 5.51)	**5.42** (5.08 - 5.69) [D]	**5.21** (4.90 - 5.49) [e]
c-IMT [mm]	**0.47** (0.41 - 0.54)	**0.47** (0.44 - 0.51)	**0.50** (0.44 - 0.54)	**0.47** (0.44 - 0.51)	**0.50** (0.46 - 0.54)
c-IMT norm [%]	**18.0** (16.4 - 19.8)	**17.6** (16.6 - 19.3)	**19.2** (17.2 - 21.7) [b]	**17.5** (16.3 - 18.9) [D]	**19.0** (17.4 - 21.1) [b,E]
Medial stress [kPa]	**55** (49 - 60)	**55** (49 - 61)	**50** (45 - 58) [a,b]	**57** (52 - 62) [D]	**51** (43 - 59) [e]
Properties					
Modulus [kPa]	**57** (42 - 81)	**50** (43 - 74)	**52** (43 - 66)	**55** (47 - 70)	**61** (51 - 75)
Compliance [MPa^{-1}]	**20** (12 - 24)	**20** (14 - 24)	**19** (15 - 23)	**18** (14 - 22)	**17** (14 - 20)
Cyclic strain [ ]	**8.3** (7.4 - 9.8)	**7.5** (6.7 - 9.2)	**8.0** (6.8 - 9.5)	**8.4** (7.0 - 10.2)	**8.8** (6.9 - 9.7)
Blood Sample Analysis					
Metabolic Parameters					
Glucose [mg/dL]	**93** (85 - 100)	**88** (83 - 97)	**94** (88 - 103)	**89** (83 - 96) [D]	**89** (83 - 95) [D]
TC [mg/dL]	**184** (161 - 230)	**180** (152 - 206)	**195** (175 - 229) [b]	**201** (175 - 239) [B]	**216** (181 - 240) [b]
TG [mg/dL]	**90** (74 - 153)	**131** (104 - 155)	**147** (109 - 196) [A]	**146** (102 - 185) [a]	**208** (149 - 242) [A,B,D,E]
HDL-c [mg/dL]	**53** (46 - 59)	**43** (39 - 54) [A]	**46** (40 - 56) [a]	**49** (41 - 60) [b]	**45** (38 - 53) [A,e]
LDL-c [mg/dL]	**106** (91 - 149)	**108** (91 - 140)	**123** (101 - 152)	**126** (95 - 155)	**129** (108 - 160) [b]
TC:HDL ratio	**3.5** (3.1 - 4)	**4.3** (3.7 - 4.8) [a]	**4.3** (3.6 - 5.1) [A]	**4.2** (3.4 - 5.2) [a]	**4.5** (4.1 - 5.7) [A,b,e]
Inflammatory Markers					
hs-CRP [ug/mL]	**3.1** (1.5 - 6.6)	**3.6** (1.8 - 14.9)	**8.1** (4.2 - 18.3) [A,b]	**3.9** (2.0 - 14.8) [d]	**5.4** (2.4 - 15.9) [a]
s-ICAM [ng/mL]	**521** (454 - 602)	**711** (574 - 937) [A]	**651** (509 - 914) [A]	**657** (526 - 914) [A]	**651** (504 - 843) [A]
s-VCAM [ng/mL]	**651** (548 - 977)	**1114** (768 - 1952) [A]	**806** (593 - 1036) [B]	**845** (649 - 1083) [a,b]	**1011** (606 - 1409) [a]
Lepitin [ng/mL]	**23** (15 - 31)	**23** (16 - 43)	**16** (11 - 24) [a,B]	**18** (12 - 27) [b]	**18** (14 - 31)

3.2.2.6 Plasma metabolic parameters

Adult population: Fasting glucose was elevated in EFV-treated compared to NVP- and LPV/r-treated subjects. Total cholesterol (TC) was elevated in all HAART-treated groups compared to HAART-naïve subjects. Triglycerides (TG) were elevated in all HAART-treated groups compared to HIV-negative subjects and in LPV/r-treated subjects

compared to all other groups. HDL was lower in HAART-naïve and EFV- and LPV/r-treated compared to HIV-negative subjects and in HAART-naïve and LPV/r-treated compared to NVP-treated subjects. LDL was higher in LPV/r-treated compared to HAART-naïve subjects. TC to HDL ratio was elevated in all HAART-treated groups and HAART-naïve compared to HIV-negative subjects and in LPV/r-treated compared to HAART-naïve and NVP-treated subjects.

Pediatric population: Fasting glucose was elevated in EFV-treated compared to HAART-naive and NVP-treated subjects. Total cholesterol and LDL were elevated in all HAART-treated groups compared to HAART-naïve subjects and further elevated in LPV/r-treated versus EFV- and NVP-treated subjects. HDL was elevated in EFV- and NVP-treated subjects compared to HAART-naïve subjects and in NVP-treated versus LPV/r-treated subjects. TC:HDL ratio and triglycerides were elevated in LPV/r-treated subjects compared to all other groups.

3.2.2.7 Inflammatory markers and adipokines

Adult population: hs-CRP was elevated in EFV-treated compared to HIV-negative, HAART-naïve, and NVP-treated subjects and in LPV/r-treated compared to HIV-negative subjects. sICAM-1 was elevated in all HIV-positive groups, compared to HIV-negative subjects. sVCAM-1 was elevated in HAART-naïve, NVP-treated, and LPV/r-treated compared to HIV-negative subjects and in HAART-naïve subjects compared to EFV- and NVP-treated subjects. Leptin was lower in EFV- and NVP-treated groups compared to HAART-naïve subjects and in EFV-treated compared to HIV-negative subjects.

3.2.2.8 Complete blood count

Adult population: No differences were observed in the number of percentages of white blood cells (WBC) or distribution of WBC classes across groups. Red blood cell markers suggest a shift towards a more anemic state in HAART-treated and, to a lesser degree, HAART-naïve subjects (Table A.1). Namely, red blood cell count was lower and mean corpuscular volume, mean corpuscular hemoglobin, and red blood cell distribution width-standard deviation were higher in all HAART-treated groups compared to HIV-negative and HAART-naïve subjects and hemoglobin and hematocrit were lower in all HAART-treated groups and HAART-naïve subjects compared to HIV-negative subjects. (Note: $p = 0.06$ comparing hemoglobin between EFV-treated and HIV-negative subjects.) Platelet count and plateletcrit were elevated in EFV-treated subjects compared to all other HIV-positive groups; platelet count was also higher in EFV-treated and plateletcrit lower in NVP-treated subjects compared to HIV-negative subjects.

3.2.2.9 Correlation and regression analysis

Adult population: Multivariable regression of data from all HAART treated subjects showed that PWV was associated with age, current EFV and LPV/r use, heart rate, B-SPB, triglycerides, LDL, and hsCRP (Table 3.4). FMD was associated with age, HIV duration, WHR, and glucose. cIMT was associated with age, current EFV use, skinfold thickness, and blood pressure.

Pediatric population: Multivariable regression showed that PWV was associated with current LPV/r-treatment, age, BMI, heart rate, and FMD (Table 3.5). Note, too, that the addition of other potentially important variables, such as total cholesterol, and

TC:HDL, which were included in preliminary model analysis, were not shown not to be significant, and thus, removed from the final model.

Table 3.4. Correlation analysis and multivariable regression model for PWV, FMD, and cIMT versus key study parameters. ρ = Spearman Rank Correlation Coefficient, P = p-value for Spearman correlation, β = model parameters, SE(β) = standard error of model parameters, p = p-value for multivariable regression for that parameter.

	Pulse Wave Velocity					Flow-mediated Dilation					Carotid Intima-media Thickness				
	Correlation		Multivariable Regression Model			Correlation		Multivariable Regression Model			Correlation		Multivariable Regression Model		
	ρ	*P*	β	SE(β)	*p*	ρ	*P*	β	SE(β)	*p*	ρ	*P*	β	SE(β)	*p*
Demographics															
Age	0.531	<0.001	0.0425	0.0151	0.006	-0.163	0.014	-0.00137	0.000564	0.017	0.412	<0.001	0.000240	7.582E-05	0.002
Sex	0.151	0.022	--	--	--	-0.15	0.023	--	--	--	0.164	0.013	--	--	--
HIV / HAART History															
CD4 count	-0.154	0.020	--	--	--	0.0429	0.52	--	--	--	0.0314	0.64	--	--	--
log10(VL)	0.066	0.32	--	--	--	-0.011	0.87	--	--	--	0.0531	0.42	--	--	--
Year since HIV+	0.189	0.004	--	--	--	-0.0105	0.87	-0.00357	0.00167	0.035	0.104	0.12	--	--	--
HAART duration	0.228	<0.001	--	--	--	0.0119	0.86	--	--	--	0.140	0.034	--	--	--
Current EFV	0.121	0.067	1.14	0.277	<0.001	-0.0987	0.14	--	--	--	0.0972	0.14	0.0257	0.0122	0.038
Current LPV/r	0.132	0.047	1.05	0.305	<0.001	-0.0471	0.48	--	--	--	0.0744	0.26	--	--	--
Body Composition															
BMI	0.107	0.11	--	--	--	0.027	0.68	--	--	--	0.109	0.1	--	--	--
WHR	0.313	<0.001	--	--	--	-0.187	0.005	-0.15	0.0647	0.023	0.171	0.009	--	--	--
Trunk:Arm	0.140	0.034	--	--	--	-0.152	0.022	--	--	--	0.105	0.11	0.00138	0.000517	0.009
Cardiovascular Metrics															
Heart Rate	0.204	0.002	0.0278	0.0125	0.028	0.0741	0.26	--	--	--	-0.0711	0.28	--	--	--
B-SBP	0.567	<0.001	0.0332	0.00662	<0.001	-0.147	0.026	--	--	--	0.311	<0.001	6.43E-05	3.14E-05	0.043
AIx75	0.408	<0.001	--	--	--	0.0978	0.14	--	--	--	0.146	0.027	--	--	--
PWV						-0.113	0.088	--	--	--	0.337	<0.001	--	--	--
FMD	-0.113	0.09	--	--	--						-0.111	0.093	--	--	--
cIMT	0.337	<0.001	--	--	--	-0.111	0.093	--	--	--					
Blood Sample Analysis															
Metabolic Parameters															
Glucose	0.130	0.05	--	--	--	-0.0671	0.31	-0.000615	0.000288	0.035	0.0915	0.17	--	--	--
TG	0.145	0.03	0.0018	0.000888	0.046	-0.084	0.21	--	--	--	0.0274	0.68	--	--	--
HDL-c	0.00364	0.96	--	--	--	0.0049	0.94	--	--	--	0.0954	0.15	--	--	--
LDL-c	0.259	<0.001	0.0063	0.00311	0.046	-0.0212	0.75	--	--	--	0.185	0.005	--	--	--
Inflammatory Markers															
VCAM	-0.125	0.06	--	--	--	0.0739	0.27	--	--	--	-0.103	0.12	--	--	--
ICAM	-0.113	0.09	--	--	--	0.134	0.042	--	--	--	-0.118	0.0756	--	--	--
Leptin	-0.0293	0.66	--	--	--	0.127	0.055	--	--	--	-0.0282	0.67	--	--	--
hs-CRP	0.300	<0.001	0.0209	0.00799	0.0106	-0.0531	0.42	--	--	--	0.0820	0.22	--	--	--
			Adjusted R2 = 0.604					***Adjusted R2 = 0.168***					***Adjusted R2 = 0.277***		

Table 3.5. Correlation analysis and multivariable regression model for pulse wave velocity versus key study parameters in a pediatric population.

	Correlation		Multivariable Regression Model		
	ρ	P	β	SE(β)	p
Demographics					
Age (yrs)	0.402	1.0E-08	0.0822	0.0205	8.8E-05
Sex	-0.014	0.84	--	--	--
Body Composition					
BMI (kg/m^2)	0.342	1.5E-06	0.0609	0.0264	0.023
WHR ( )	-0.017	0.81	--	--	--
Trunk:arm	0.195	0.0073	-	-	-
HIV/HAART History					
Current CD4+ count	-0.131	0.072	-	-	-
Yrs on HAART	0.150	0.039	-	-	-
Current EFV Treatment	0.024	0.74	--	--	--
Current NVP Treatment	-0.146	0.046	-	-	-
Current LPV/r Treatment	0.199	0.0061	0.572	0.161	0.00051
Cardiovascular Metrics					
Heart Rate (bpm)	0.120	0.10	0.0159	0.00384	5.4E-05
Brachial Artery SBP (mmHg)	0.358	4.4E-07	-	-	-
Flow-Mediated Dilation (%)	-0.079	0.28	-2.034	0.942	0.032
cIMT (microns)	-0.049	0.50	--	--	--
Blood Metabolic Parameters					
Glucose (mg/dL)	0.044	0.55	--	--	--
TG (mg/dL)	0.108	0.14	-	-	-
HDL-c (mg/dL)	-0.001	0.99	--	--	--
LDL-c (mg/dL)	0.215	0.0030	-	-	-
				Adjusted R2 =	0.269

3.2.3 Discussion

3.2.3.1 Preclinical markers of atherosclerosis

Adult population

There are numerous studies that associate specific antiretroviral drugs with early onset of atherosclerosis. Protease inhibitors (PI's) have been the most widely implicated class of antiretroviral drugs associated with atherosclerosis and have been correlated with increased c-IMT [84, 85], impaired FMD [86-88], dyslipidemia [89], atherosclerosis [7, 90], and myocardial infarction [91], but others have reported contradictory results [92-96]. Non-nucleoside reverse transcriptase inhibitors (NNRTIs) have been associated with

elevated cholesterol levels and triglycerides [7], with EFV associated with higher total cholesterol and triglyceride levels than NVP [89]. Less is known about the association between NNRTIs and c-IMT, FMD, and arterial stiffness.

Increased arterial stiffness is a key predictor of future cardiovascular events [180] and is elevated in HIV-positive populations [71-74]. van Vonderen et al. report decreased distensibility and compliance coefficients in carotid, femoral, and brachial arteries in HIV-positive subjects, with no differences between HAART-naïve and HAART-treated subjects. In a longitudinal study, van Vonderen et al. showed a *decrease* in carotid arterial stiffness, but increase in femoral artery stiffness (i.e., a decrease in distensibility and compliance coefficients) after 24 months of AZT+3TC+LPV/r treatment, with similar trends in NVP+LPV/r treatment [71]. The current report shows that central arterial stiffness measured via PWV was higher in adult EFV- and LPV/r-treated subjects, compared to NVP-treated subjects. No differences were observed in the carotid artery elastic modulus, compliance, or the distensibility or compliance coefficients (not shown) across groups. Note that arterial stiffening in aorta, but not CCA's, is consistent with recent findings in a mouse model of AZT treatment [12].

Arterial stiffness appears to increase with HAART [71, 73, 74] and is associated with immune cell activation and senescence [72] and may be independent of lipodystrophy [181]. In the current study, PWV was associated with EFV and LPV/r use, traditional cardiovascular risk factors (age, heart rate, B-SBP), dyslipidemia (triglycerides and LDL), and systemic inflammation (hsCRP). Taken together, the current study and previous studies from the literature suggest that both HIV infection and HAART play a role in arterial stiffening, with differing effects at different locations in the vasculature.

Impaired brachial artery FMD is a non-invasive indicator of endothelial dysfunction and is associated with elevated cardiovascular risk in the general population [182]. Impaired FMD is also widely reported in HIV-infected populations and appears to be associated with both viral RNA levels [183, 184] and HAART [75-77]. Although not significantly different than pre-HAART values, Gupta *et al*. reports a significant decrease in FMD in EFV-treated compared to PI-treated subjects after 12-months of treatment [77]. Impaired FMD has been associated with lipodystrophy [52]; the association between FMD and dyslipidemia with HIV, however, is debatable [75]. Our data show that EFV- and LPV/r-treated adult subjects exhibit lower FMD, compared to NVP-treated and HAART-naïve subjects. Multivariant regression shows that FMD was associated with age, duration of HIV, WHR, and fasting blood glucose levels.

Increased cIMT has been widely reported in HIV-infected populations [51, 71, 78, 183, 185-187], is strongly associated with all-cause death in HIV patients [188], and appears to be associated with both HIV infection and HAART regimen [78, 185]. PI's have been implicated [189] as a mediator of increased cIMT, and cIMT has been associated with immune cell activation [190, 191], systemic inflammation [188, 191, 192], and Framingham risk [193]. Our data show nominally higher cIMT in EFV- and LPV/r-treated subject; however, increased cIMT only becomes significant when normalized to *D*/2. Multivariant regression showed that cIMT was associated with current EFV use, traditional cardiovascular risk factors (age and B-SBP), and lipodystrophy (Trunk:Arm).

Our results show elevated markers of atherosclerosis in EFV- and LPV/r-treated subjects, compared to HAART-naïve and NVP-treated groups. However, there are

several compounding factors at play that contribute to this observation. First, the years since HIV diagnosis in the HAART-treated group is nearly double that of the HIV-naïve group. However, the NVP group had a longer duration of HIV infection, compared to the EFV group. Second, more subjects in the EFV- and LPV/r-treated groups were taking an NRTI-backbone of TDF+3TC, compared to the NVP-treated group, which had more subjects taking AZT+3TC. The role of AZT in arterial stiffening, endothelial dysfunction, and cIMT is well documented [12, 82, 194]. We included TDF and AZT in early iterations of our multivariable regression model; due to their low association with arterial stiffness, cIMT, and FMD, TDF and AZT were considered key predictors of these markers and were subsequently eliminated from the final model. Clinical evidence for atherosclerosis associated with NRTIs is often indirect and difficult to define because NRTIs are typically not prescribed as monotherapy and cardiovascular effects are often attributed to other components of HAART (namely PIs). Nevertheless, recent exposure to abacavir, didanosine, and tenofovir in adult populations was associated with increased risk of heart failure [195-198]; however, these findings are controversial [199]. Abacavir has been associated with impaired FMD [52]. Experimental models, including those from our group, clearly show that AZT, induces endothelial dysfunction [194, 200] and increased c-IMT and arterial stiffness [12].

Data from the literature suggest that HIV, independent of HAART, can induce cardiovascular disease [187, 201, 202]. Post-mortem analyses reveal coronary arteriopathy [54, 203], pulmonary arteriopathy [203], major atherosclerotic lesions [55, 203] and cerebral aneurysms [204] in HIV-positive patients not treated with HAART. A long-term multi-institution analysis concluded that cessation of HAART in HIV-positive

patients increased their short-term risk of developing cardiovascular disease [201]. Viral load correlated inversely with endothelium-dependent FMD without any relation to HAART regimens [205]; thus, viral load is a significant predictor of impaired FMD [96]. HIV infected, HAART-naïve patients exhibited elevated c-IMT and impaired FMD [202] and HIV-infected children had significantly reduced FMD and increased arterial stiffness of the carotid artery compared to non-infected children, with no significant differences between HAART treated and HAART naïve subjects [206]. Lorenz et al. concluded that both HAART and HIV-infection are independent risk factors for the development of atherosclerosis in adults [207]. They show that c-IMT of the carotid bifurcation was 25% higher in HIV positive / HAART-naïve patients compared to uninfected controls, but observed significantly greater c-IMT of the carotid bifurcation and the common carotid artery due to HAART treatment in HIV positive subjects. Although c-IMT, FMD, and arterial stiffening are affected by HIV infection, it appears that HIV infection only introduces mild dyslipidemia [202, 208, 209].

Pediatric population

Increased arterial stiffness and c-IMT and impaired FMD are key predictors of future cardiovascular events and are elevated in pediatric HIV-positive populations [192, 209-212]. Bonnet et al. reported elevated common carotid arterial stiffness and impaired brachial artery FMD HIV-infected children (pooled HAART-treated and HAART-naïve), compared to HIV-negative controls, with no differences in cIMT; no differences were observed between treated and treatment-naïve subjects or between subjects with or without dyslipidemia. McComsey et al. and Ross et al. report elevated cIMT among HIV-infected, HAART-treated subjects, compared to HIV-negative controls and that the

duration of HAART, CD4 count, and markers of inflammation were among the key predictors of cIMT [192, 211, 212]. Charakida et al. showed the cIMT was elevated and FMD reduced in HIV-infected children, particularly those taking a protease inhibitor-containing regimen [209].

The current report shows that central arterial stiffness measured via PWV was elevated in LPV/r-treated subjects, compared to HAART-naïve and EFV- and NVP-treated subjects. Although central arterial stiffness was increased, no differences were observed in the common carotid artery elastic modulus, compliance, or the distensibility or compliance coefficients. We did not observe differences in cIMT across groups, but note a subtle trend of increased cIMT in LPV/r-treated subjects, compared to HAART-naïve and EFV- and NVP-treated subjects. Given that the primary end-point of the study was PWV, this study was not powered for c-IMT or FMD; thus, firm conclusions regarding this possible trend in c-IMT cannot be made from these results. No differences or trends in FMD were observed across groups.

Multivariable regression showed that current LPV/r use was an independent predictor of PWV in HAART-treated subjects. Despite no differences in FMD across groups, multivariable regression showed FMD as a key predictor of PWV. This was a surprising finding, given that the strength of the correlation between FMD and PWV was not strong (p=0.28). Note, that when heart rate (or FMD) are eliminated from the model, systolic blood pressure arises as a key predictor rather than FMD (or heart rate), illustrating the co-linearity of these parameters. PWV was also associated to the traditional risk factors, age and BMI.

3.2.3.2 Metabolic disorders

Adult population

Alterations in plasma lipid profiles have been reported in both HAART-naïve and HAART-treated subjects that are characterized by increased TG's and decreased HDL; increased total cholesterol and LDL are also reported and PI-containing regimens are generally associated with a less favorable lipid profile compared to PI-sparing regimens [89, 213]. Our results are consistent with these observations, with both HAART-naïve and HAART-treated subjects showing less favorable lipid profiles than HIV-negative subjects, and PI-treated subjects exhibiting worse lipid profiles than other HIV-positive groups.

HIV-associated lipodystrophy is characterized by peripheral lipoatrophy and central lipohypertrophy, and are often associated with disorders in glucose metabolism, insulin resistance, dyslipidemia, altered cytokine and adipokine production, and markers of cardiovascular disease [214, 215]. Self-reported observations of fat redistribution in the present study suggest similar trends, with a significant fraction of HAART subjects reporting observed decreases in peripheral fat and an increase in central fat. In addition, NVP-treated subjects reported increase in fat in their face, arms, and legs. Skin-fold thickness measurements support these self-reports, with EFV-, NVP-, and LPV/r-treated subjects having higher Trunk/arm ratios compared to HIV-negative and HAART-naïve subjects. Note that the trunk skin-fold thickness measurement did not suggest central lipohypertrophy, as superiliac and sub-scapula values were generally lower or not significantly different in HAART-treated compared to non-HAART-treated subjects.

Pediatric population

Dyslipidemia and lipodystrophy [216-221] are widely reported in HIV-infected children and adolescents and generally show elevated total cholesterol, LDL, and triglycerides and reduced HDL with HAART treatment, with elevated dyslipidemia in protease treatment. Our results are consistent with these findings, showing proatherogenic lipid profiles with HAART treatment, particularly in the LPV/r group. Our results for BMI, WHR, and skin-fold thickness show little evidence of differences in these markers of lipodystrophy across HAART-treatment and HAART-naïve groups.

3.2.3.3 Inflammatory markers and adipokines

hsCRP is a key predictor of future cardiovascular events in the general population [222-224], is widely reported to be elevated in HIV populations [51, 192, 225-232] (noting contradictory reports [72, 183, 233]), and is associated with all-cause death in HIV patients [188]. Most studies show little or no HAART dependency [71, 77, 184, 228, 234] and hsCRP appears to be independent of lipodystrophy [235]. Our results show that hsCRP is elevated in EFV-treated subjects compared to HIV-negative, HAART-naïve, and NVP-treated subjects and elevated in LPV/r-treated subjects compared to HIV-negative subjects and that hsCRP is a key predictor of PWV.

sVCAM-1 and sICAM-1 are plasma biomarkers that have been associated with the initiation and progression of atherosclerosis [236] and are commonly associated with HIV infection [228, 232, 233, 237]. Following initiation of HAART, values decrease from pre-HAART levels, but remain higher than HIV-negative controls [71, 77, 228, 238]. Our results are consistent with these findings, with sVCAM-1 and sICAM-1 levels elevated in HAART-naïve and, to a lesser degree, in HAART-treated subjects compared

to HIV-negative subjects, but no correlation between sVCAM-1 or sICAM-1 levels and PWV, FMD, or cIMT were found.

Adipokines such as adiponectin and leptin have been studied intensively for their relation to obesity, insulin resistance, and hyperglycemia and as potential proatherogenic mediators [239, 240]. Low leptin and adiponectin levels are more common in persons with HIV and correlate with lipodystrophy [225, 232, 235, 241]. Our results show reduced leptin levels with HAART treatment, but no correlation between leptin levels and PWV, FMD, or cIMT were found.

3.2.3.4 Study limitations

Adult population

This study has several limitations. The cross-sectional design of this study does not allow for a causal relationship between specific antiretroviral drugs and the markers studied. As is often the case, there were challenges in recruiting a representative HIV-negative control group. Controls were recruited by word of mouth at Black Lion hospital, and some recruits may have been referred from the Cardiac clinic. This may explain, in part, why the preclinical markers of atherosclerosis were nominally, albeit not significantly higher (except for FMD), in the controls versus NVP-treated and HAART-naïve groups. Although the normalization of the cIMT was motivated to normalize values across a broad range of patients and showed significant differences across groups, although the more traditional 'raw' cIMT data followed similar trends, the raw data did not show significant differences. Also, the cIMT images were taken from a single profile view, rather than the average of several orthogonal views and the FMD protocol did not include nitroglycerine to quantify the endothelial independent vasodilation. Taken

together, we believe these limitations do not significantly bias the conclusions of this study.

Pediatric population

This study has several limitations. The cross-sectional design of this study does not allow for a causal relationship between specific antiretroviral drugs and the markers studied. The lack of a HIV-negative control group makes it harder to assess the impact of HIV infection, itself, versus the role of HAART regimens. The cumulative duration of HAART was larger in LPV/r-treated subjects, compared to EFV- and NVP-treated subjects. The longer duration of treatment could play a role the observed elevation in PWV; note, however, that the multivariable regression did not identify cumulative HAART duration as a significant variable. Note, too, that LPV/r is a second line therapy; thus, these patients have had some immunologic failure, which may be associated with a longer history of systemic inflammation or immune dysfunction that led to the observed increase in arterial stiffness. Also, NRTI backbones for the LPV/r-treated subjects were primarily ABC and ddI. ABC has been implicated as a potential contributor to cardiovascular risk and may be playing a role in the current study [52, 198, 242]. These results delineate the need for additional longitudinal studies to confirm such causal relationship between specific antiviral treatment and atherosclerosis in this population. Taken together, we believe these limitations do not significantly bias the conclusions of this study. Note, too, that plasma HIV RNA analysis was performed on 23% of the study participants; given this low coverage, viral load was not included in the results.

In closure, this report suggests that current LPV/r use (typically in combination with ABC and ddI) may play a role in the development of HIV-associated preclinical

markers of atherosclerosis in pediatric subjects. The data presented herein are consistent with previous results, in that HAART-treated subjects exhibit arterial stiffening, elevated cholesterol, LDL, TC:HDL ratio and triglycerides. This cross-sectional study delineates the need for additional longitudinal and mechanistic studies to establish a causal relationship between LPV/r-treatment and atherosclerosis in this population and the underlying mechanisms of atherogenesis and the progression of atherosclerosis.

3.3 Hypothesis 2[4]: EFV treatment will lead to arterial stiffening but not atherosclerotic plaque progression in a mouse model of atherosclerosis

To test this hypothesis, ApoE$^{-/-}$ mice were treated with various concentrations of EFV or vehicle for either 35 or 70 days, and geometry and mechanical properties as well as atherosclerotic plaque progression will be analyzed in the abdominal and thoracic aorta, respectively. The goal of testing this hypothesis is to better inform the guidelines for treatment and care of HIV-infected patients as well as establish a novel framework for future investigations of mechanisms driving HAART-induced vascular remodeling.

3.3.1 Methods and Materials

3.3.1.1 Animals and diet

Male ApoE$^{-/-}$ mice bred on a C57 background were obtained at 6 weeks of age from Jackson Laboratories (Bar Harbor, ME) and kept on a 12-hour light/dark cycle in a

[4] Caulk AW, Soler J, Platt MO, Gleason RL. Efavirenz treatment leads to arterial stiffening in apolipoprotein E-null mice. Submitted to J Biomechanics. Mar 2015.

temperature-controlled room at 22°C. The animals were housed and cared for according to the guidelines set forth the by the National Institutes of Health for the care and use of experimental animals. All experimental procedures were reviewed and approved by the Georgia Tech Institutional Animal Care and Use Committee (IACUC).

Mice were kept on a high-fat diet from Teklad, Inc. (TD88137) consisting of a caloric content of 0.15% cholesterol and 42% fat and given water ad libitum. The ingredients to the diet are as follows: 195 g high protein casein, 3 g DL-methionine, 341.46 g sucrose, 150 g corn starch, 210 g anhydrous milkfat, 1.5 g cholesterol, 50 g cellulose, 35 g mineral mix (AIN-76), 4 g calcium carbonate, 10 g vitamin mix, and 0.04 g ethoxyquin.

3.3.1.2 Drug administration

Efavirenz (EFV) was obtained from Toronto Research Chemicals, Inc. (catalog no. E425000) in powder form. Because EFV has low solubility in water, it is normally reconstituted in methanol. However, to prevent unwanted side effects during long-term daily administration in mice, EFV was reconstituted in deionized water (1 mg/mL for 1X doses and 10 mg/mL for 10X doses) and repeatedly sonicated until the powder was visibly evenly distributed throughout the solution. To ensure uniform distribution upon administration, the solution was briefly spun in a vortex mixer prior to administration to evenly distribute any powder that had settled to the bottom of the solution.

Mice were administered EFV (n = 6) at 10X relative to the normal human dosage (75 mg/kg) or water (n = 6) daily for 5 weeks. To facilitate comparison for concentration- and time-dependent evaluation in plaque development, animals were given a 1X dose of EFV for 5 weeks (n = 6) or 10 weeks (n = 6). Water controls from the 10X study were

used for comparison in the 5 week study as volume of vehicle delivered was equal in control and experimental groups, and additional animals were treated with water for 10 weeks to serve as additional controls (n = 8). In total, 32 animals were used for this study. Animals were weighed on a weekly basis, and volumes of EFV were administered based on the weekly weight measurements. For example, a mouse weighing 0.020 kg would receive 0.15 mL of EFV solution. Note that the dilutions of EFV were achieved in such a way as to make volume administrations identical regardless of whether the concentrations were 1X or 10X. Control mice were treated with comparable volumes of water. Drug administrations were performed using oral gavage. Briefly, the mice were lightly anesthetized with gas isoflurane, and a 30 gauge ball-point syringe was inserted into the esophagus until reaching the stomach. Once the drug was administered, mice were monitored until they regained consciousness to ensure that the airway was not obstructed during the administration.

3.3.1.3 Cylindrical biaxial mechanical testing

Following exsanguination, suprarenal abdominal aortas were excised from the region approximately 1-2 mm proximal to the celiac artery and immediately distal to the renal arteries. Vessels were carefully cleaned of all perivascular tissue, and all branches were tied using 8-0 silk suture. Vessels were mounted on a custom biaxial testing device [243] and maintained in physiologic buffered saline solution (PBS) containing sodium nitroprusside to prevent force generation from the smooth muscle cells and ensure that testing was performed in a fully passive state. Unloaded length and diameter were determined visually using LabView, and the vessels were preconditioned by ramping the luminal pressure from 0 to 160 mmHg at axial stretch values of 1.3, 1.4, 1.5, 1.6, 1.7, and

1.8, where the stretch λ is defined by the ratio of the loaded length to the unloaded length. Vessels were then subjected to three loading cycles of pressure values from 0 to 160 mmHg at each of the previously mentioned stretch values in order to generate pressure / diameter curves. Fluid level in the bath of the device was monitored to identify the presence of leaks in the vessels. Any vessels with substantial leaks were not considered in the analysis of vessel mechanical properties, resulting in 4 control samples and 5 EFV-treated samples being included in stiffness analysis. All mechanical tests were performed within 4 hours of excision. Following mechanical testing, aortas were embedded in optimum cutting temperature compound (OCT) in an unloaded state and stored for histological analysis and quantification of cathepsin activity.

3.3.1.4 Quantification of compliance and *in vivo* axial stretch

Arterial stiffness was quantified by calculating the compliance, defined as $C = (\Delta D/D)/\Delta P$. Diameter measurements were separated into bins by pressure at an interval of 10 mmHg and averaged according to each bin. Compliance calculations were performed using binned measurements of pressure and diameter.

Estimation of the *in vivo* axial stretch of arteries has previously been performed by determining the intersection point of various axial force vs. axial stretch curves under isobaric conditions. Data from biaxial mechanical testing of aortas was utilized by rearranging the binned data from arterial stiffness calculations such that axial force measurements were grouped by pressure rather than axial stretch. Therefore, each isobaric curve had at most 6 data points corresponding to a single pressure value and 6 axial stretch values. Second-order polynomials were fit to all isobaric curves, and the

intersection points of all curves were calculated and averaged in order to estimate the *in vivo* axial stretch.

3.3.1.5 Measurement of intima-media thickness

Abdominal aortas were sectioned at a thickness of 7 μm and stained for hematoxylin and eosin. Sections were imaged using a Nikon bright-field microscope and processed using a custom MATLAB script for determining the thickness of the intima-media layer. Briefly, each image was loaded into the script, and the adventitia/media interface as well as the luminal surface were traced. The average inner and outer diameter were then determined from the measured circumferences, and the thickness of the intima-media was calculated as the difference between the average inner and outer radius.

3.3.1.6 Determination of plaque coverage

Vessels for determination of plaque progression were excised following either 5 weeks or 10 weeks of EFV administration. Thoracic aortas were removed from just below the aortic arch to the diaphragm, carefully cleaned of perivascular tissue, and fixed in 10% buffered formalin. Aortic arches were removed from immediately distal to the sinus to immediately proximal to the thoracic aorta. Note that one aortic arch from the control group was excluded from analysis due to plaque disruption during excision. Vessels were cut longitudinally and pinned en face in a petri dish. A digital picture of each vessel was acquired using a Marlin F131B camera (Allied Vision Technologies). Images were analyzed for plaque coverage using ImageJ software (NIH, Bethesda, MD) following previously published methods [244]. Plaque coverage was calculated twice for each image by the same observer, and the results were averaged to determine the final value of plaque coverage.

3.3.1.7 Statistical analysis

All data were analyzed using a student's unpaired *t*-test with equal variance, and significance was determined by *p* values less than 0.05. Data were expressed as the mean ± SEM. Additionally, statistical analysis of plaque progression following 5 weeks of treatment was performed using a one-way ANOVA followed by a Tukey post-hoc *t*-test to compare control data, 1X, and 10X EFV data.

3.3.2 Results

3.3.2.1 EFV treatment alters mechanical behavior in abdominal aortas

Suprarenal abdominal aortas from mice treated with water or 10X EFV for 5 weeks were subjected to biaxial cylindrical mechanical testing in which pressure was ramped under fixed length conditions of λ = 1.3, 1.4, 1.5, 1.6, 1.7, and 1.8. Diameter and axial force measurements from each stretch value were binned according to corresponding pressure values at an interval of 10 mmHg. Compliance was quantified for each stretch value and for each bin. Diameter measurements and compliance calculations revealed a trend towards a slight increase in stiffness at axial stretch values of λ = 1.6 and above in EFV-treated mice compared to controls (Figure 3.2).

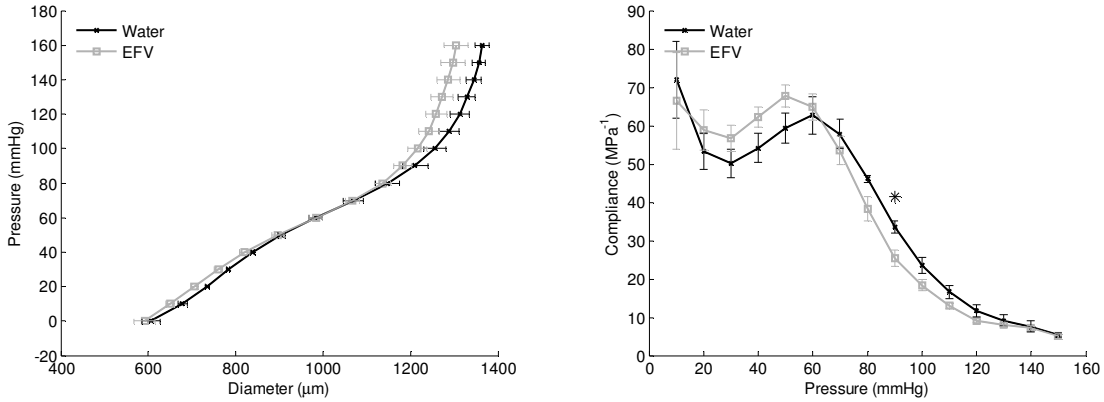

Figure 3.2. Mechanical testing results from suprarenal abdominal aortas from water-treated and EFV-treated mice. (Left) Pressure-diameter testing results are shown for an axial stretch value of 1.7. (Right) Calculations of compliance for aortas under a range of pressure values at a fixed length of $\lambda = 1.7$. EFV-treated vessels had decreased compliance compared to water-treated controls at 90 mmHg. (*) Denotes $p < 0.05$.

Statistical significance was achieved for compliance values at 90 mmHg at $\lambda = 1.6$ and 1.7 as well as 80 mmHg at $\lambda = 1.8$. Various stiffness values at pressures between 80 and 120 mmHg exhibited near significance with p values reaching less than 0.1 at stretch values of 1.6 and above. Axial force vs. pressure curves were shifted downward from vessels treated with EFV (Figure 3.3). Force values between 0 and 70 mmHg showed statistically significant differences ($p < 0.05$) at all stretch values and in some cases reached significance for pressure values of 80 or 90 mmHg. Similarly, axial force vs. axial stretch ratio curves were used to determine the *in vivo* axial stretch of each vessel. The average *in vivo* stretch of control arteries was 1.709 ± 0.017, and the average *in vivo* stretch of EFV-treated arteries was 1.649 ± 0.034. While EFV treatment appeared to decrease the *in vivo* stretch, the differences were not statistically significant ($p = 0.186$).

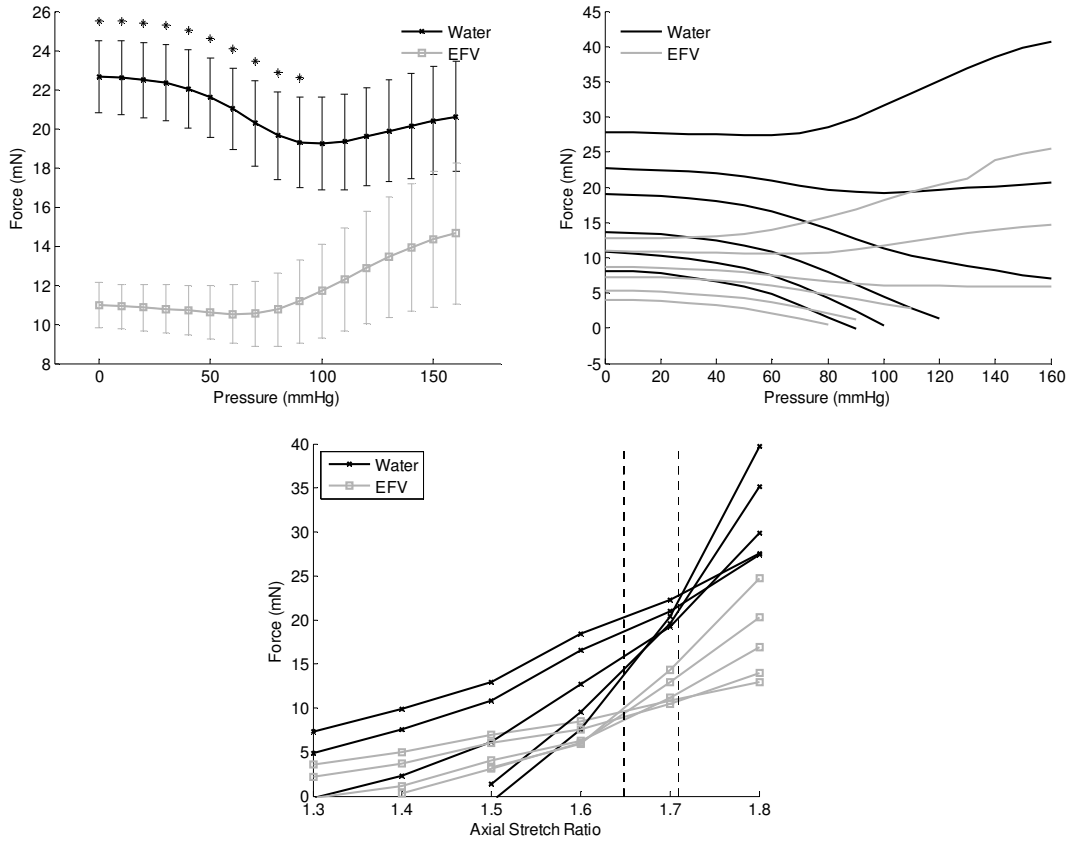

Figure 3.3. Axial force vs. pressure measurements of suprarenal abdominal aortas from water- and EFV-treated mice. (Top left) Axial force vs. pressure of aortas at an axial stretch of 1.7 from water- (black) and 10X EFV-treated (grey) mice. Force values are significantly lower in the EFV-treated group at pressure values up to 90 mmHg. Asterisks denote $p<0.05$. (Top Right) Force values from all axial stretch conditions are reported in black for controls and grey for EFV-treated vessels. Note that the curves are shifted downwards for the EFV-treated group. (Bottom) Average axial force vs. axial stretch curves depicting *in vivo* axial stretch values of water- and EFV-treated mice. Vertical dotted lines denote the *in vivo* axial stretch values for each group. Note the intersection point of the curves from EFV-treated samples is lower than that of water-treated samples.

3.3.2.2 EFV treatment does not affect thickness of the aortic wall

Suprarenal abdominal aortas from mice treated with water or 10X EFV for 5 weeks were embedded in OCT following mechanical testing and stained with hematoxylin and eosin. Aortic IMT was 22.36 ± 2.44 μm in water-treated mice vs. 21.13

± 1.63 µm in EFV-treated mice (Figure 3.4). The differences were not statistically significant.

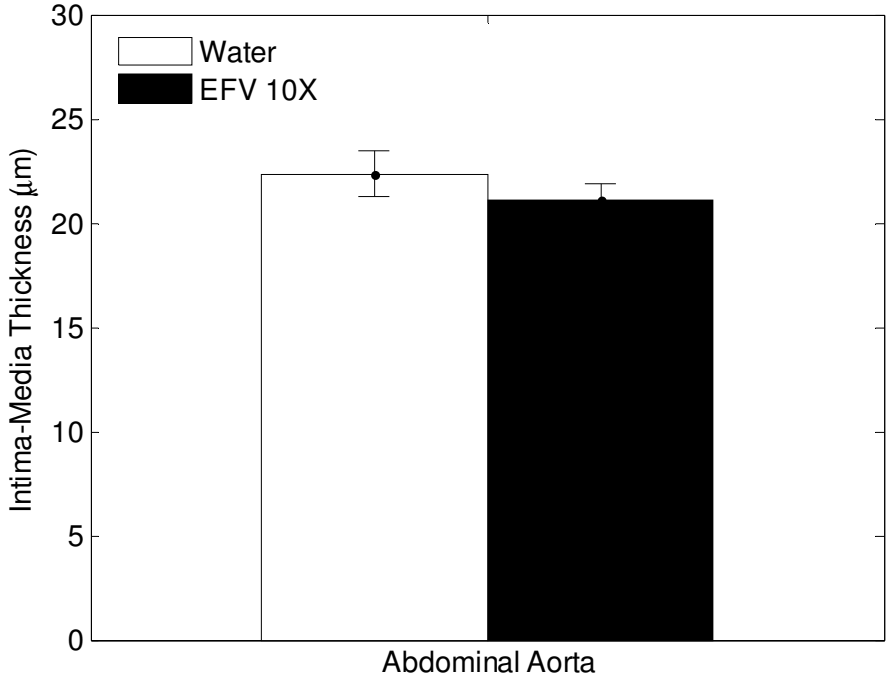

Figure 3.4. Suprarenal abdominal aorta intima-media thickness measurements from mice treated with water or 10X EFV for 5 weeks. No differences were observed in aortic IMT between groups.

3.3.2.3 EFV treatment does not accelerate plaque progression in dose- or time-dependent manners

ApoE$^{-/-}$ mice were treated with water, 1X EFV, or 10X EFV for 5 weeks and water or 1X EFV for 10 weeks, and the thoracic aorta and aortic arch were subsequently removed, cleaned, and opened en face for imaging. Plaque coverage was determined as a percent of the total luminal area. EFV-treated mice had a higher percentage of plaque coverage than water-treated mice in the thoracic aorta and the aortic arch after 5 weeks of treatment with 1X EFV compared to controls; however the trends were not significant.

Interestingly, the trend was reversed in both the thoracic aorta and the arch with a 10X treatment (Figure 3.5). Differences between EFV-treated vessels and controls were not different following 10 weeks of treatment with 1X EFV and water. All results for plaque coverage can be seen in Table 3.6.

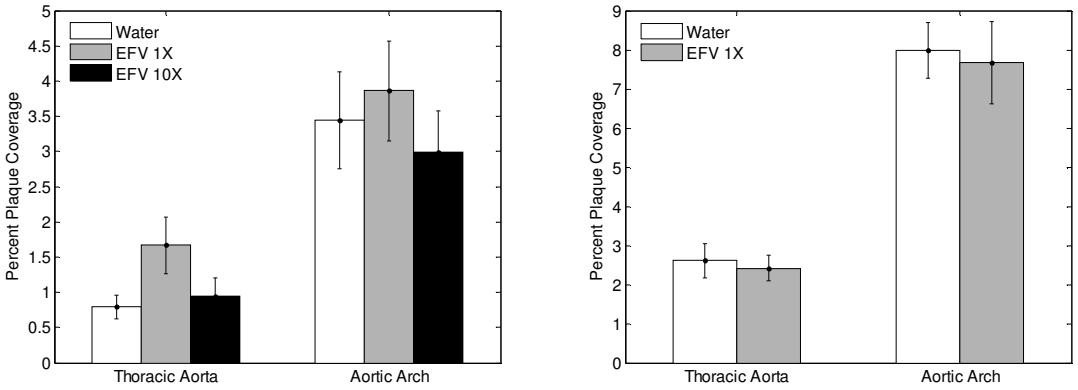

Figure 3.5. Percent plaque coverage in various arterial segments from water- and EFV-treated mice. (Left) Plaque coverage in mice treated with water (*n*=6, one excluded from arch analysis), 1X EFV (*n*=6), or 10X EFV (*n*=6) for 5 weeks. Note that the 1X EFV group has an increasing trend compared to the control group, but the 10X EFV group has less plaque than the 1X group. No significant differences were observed. (Right) Plaque coverage in mice treated with water (*n*=8) or 1X EFV (*n*=6) for 10 weeks. Plaque coverage was increased compared to respective groups treated for 5 weeks, but no differences were observed between groups treated for 10 weeks.

Table 3.6. Calculated values of plaque coverage in thoracic aortas and aortic arches from various water- and EFV-treated mice. Note that in the 5-week treatment groups, control values for the 1X EFV group were also used as controls for the 10X EFV group because the volume of water delivered was the same regardless of the concentration of EFV.

	5 week 1X treatment	5 week 10X treatment	10 week 1X treatment
Thoracic aorta plaque coverage (%)			
Water-treated	0.79 ± 0.17	0.79 ± 0.17	2.61 ± 0.43
EFV-treated	1.67 ± 0.4	0.95 ± 0.25	2.42 ± 0.32
Aortic arch plaque coverage (%)			
Water-treated	3.44 ± 0.69	3.44 ± 0.69	7.98 ± 0.71
EFV-treated	3.86 ± 0.71	2.99 ± 0.58	7.67 ± 1.06

3.3.3 Discussion

The role of HAART treatment in the development of early onset cardiovascular disease has become the focus of much attention given the increased life expectancy and increase in non-AIDS-related comorbidities in HIV-positive populations. Various classes of antiretroviral drugs have been implicated to different extents in the development of precursors of CVD [7]. Of specific interest is the development of arterial stiffening and increased vessel wall thickness as these are commonly used subclinical markers of atherosclerosis. Clinical studies have shown HAART-induced changes in carotid IMT [48], arterial stiffening [49, 176], and progression of endothelial dysfunction in HIV-positive patients [9, 52, 53]. Our lab has previously shown development of arterial stiffening and increased intima-media thickness in mice treated with azidothymidine (AZT), one of the most common NRTIs in HIV treatment [12]. Other labs have shown similar atherogenic results in mice treated with various antiretroviral drugs [80, 81, 83, 165, 166]. However, NNRTIs such as EFV have received less attention compared to their NRTI relatives. Despite ample clinical implications of NNRTIs in the alterations of lipid profiles [7, 173] and recent reports of their role in CVD development [9], only a handful of laboratory studies have investigated the role of NNRTIs in the progression of atherosclerosis [8, 10, 11, 175]. Consequently, we performed long-term in vivo studies to examine the effects of EFV on the development of commonly investigated preclinical markers of atherosclerosis as well as late-stage atherosclerosis in an atherogenic mouse model.

ApoE$^{-/-}$ mice were given bolus doses of EFV daily via oral gavage for 35 days in order to study the effects of the drug on the development of arterial stiffening and

thickening of the arterial wall. Compliance values were significantly different at the highest stretch values in the range of 80-90 mmHg. Previous studies have suggested that in vivo axial stretch values of normal murine carotid arteries lie in the range of 1.6-1.9 depending on the strain of the mouse [178, 245], thus implicating higher values of axial stretch as being the most physiologically relevant in analysis. Our results show significant increases in arterial stiffening of the abdominal aorta at physiologic values of axial stretch and blood pressure, indicating a possible role of EFV in the development of arterial stiffening. This finding corroborates results reported in hypothesis 1 in which arterial stiffening was associated with EFV treatment in the aorta but not in the carotid arteries. Additionally, axial force values were consistently decreased at pressure values between 0 and 70 mmHg, and there was a non-significant trend towards a decreased *in vivo* axial stretch ratio. Although modulus calculations were not different in these ranges, the force measurements still suggest a role of EFV in maladaptive vascular remodeling. Previous studies have shown that arterial remodeling is dependent on axial length and directly affects longitudinal tension in arteries [115, 177, 178]. Indeed, studies have shown a decrease in axial force in a mouse model of fibulin-5 deficiency as well as a model of AZT treatment [12, 245], and one study demonstrated a decrease in the *in vivo* axial stretch ratio with no accompanied change in pressure-diameter behavior in a mouse model of abdominal aortic aneurysm [179]. Thus, the change in mechanical behavior seen following EFV-treatment may be an indicator of early vascular remodeling leading to dysfunction. Additionally, the alteration of axial force may even be a marker that precedes circumferential stiffening that is normally measured in the clinic.

Changes in aortic geometry have been reported due to treatment with AZT [12, 83], and changes in carotid geometry have recently been associated with EFV treatment in a cross-sectional study (hypothesis 1). Aortic intima-media thickness was evaluated in mice treated with water or 10X EFV for 5 weeks. No significant differences were observed, suggesting that EFV plays no role in short-term thickening of the aortic wall. However, given the changes in mechanical behavior following 10X EFV treatment for 5 weeks, the possibility of macroscopic remodeling following a longer treatment regimen cannot be discounted and warrants further investigation.

Plaque progression was analyzed as a function of duration of treatment as well as bolus concentration. For 5 weeks of treatment, 3 groups were analyzed: a control group, a group treated with 1X EFV, and a group treated with 10X EFV. Analysis was performed for thoracic aortas as well as aortic arches. Interestingly, plaque coverage tended to increase most in the 1X treated group rather than the 10X treated group in both vessel types. However, following a one-way ANOVA, no differences were observed between groups in either vessel type. Vessels from mice treated for 10 weeks with water or 1X EFV were also analyzed. Plaque coverage in all vessels was increased compared to each respective 5-week-treated group; however, differences between controls and EFV-treated mice at 10 weeks were not existent. Tohyama et al. showed that EFV treatment has a beneficial effect on reverse cholesterol transport and leads to a transient increase in HDL-c in hA-I transgenic mice [175]. Such a finding may explain both the transient increase in plaque coverage of 1X EFV-treated mice compared to controls; however other studies have demonstrated no effect of EFV on cholesterol efflux from macrophages [246] or negative effects of EFV on lipid content in hepatic cells [11], so available results are

conflicting. The differential effects of EFV seen in this study (neutral or beneficial effects on plaque progression and deleterious effects on vascular remodeling) may be explained by different mechanisms acting along various pathways. Additional studies should be performed investigating the mechanisms of EFV-induced disease progression in vivo.

It should be noted that the mice analyzed in this study were 11 or 16 weeks old upon completion of the study. In general, analysis of plaque progression requires that mice be much older as measureable plaque progression may normally occur as late as 30-40 weeks of age. This study was aimed primarily at identifying accelerated development of preclinical markers of atherosclerosis; thus, younger mice were chosen in order to attenuate aging effects in the vasculature. Consequently, plaque coverage was low, consistently less than 10% in all vessels at all time points and often as low as 1%. Difficulties arise in the interpretation of these results due to the low signal-to-noise ratio. A more in-depth analysis of plaque progression at later developmental stages would be useful in future studies.

Previous animal studies focusing on effects of EFV related to CVD have utilized concentrations comparable to our 1X group (approximately 10 mg/kg). However, differences in pharmacokinetic profiles between species following EFV administration have been shown in multiple studies (compare [247] and [248]) that suggest higher dose requirements in rodents to achieve plasma concentrations comparable to those in humans, leading us to utilize higher concentrations for our investigation of EFV-induced vascular remodeling. Additionally, many of these studies have simply included the substance in the food and estimated the dose based on consumption. Our study employs a more accurate methodology by providing a daily dose of EFV via oral gavage. The solubility

of EFV in water is low, and we consequently utilized sonication to ensure that the drug was evenly distributed in the medium; however, accuracy in concentration delivered to the animals is still lost in this case. Some have shown improved bioavailability of EFV using polymeric micelles for encapsulation [249], and this may be employed in future studies for increased accuracy in drug delivery to the animals.

Additional limitations of this study arise in the use of an animal model that does not accurately recapitulate the physiologic environment of HIV-positive patients receiving HAART. These patients receive a cocktail of three drugs of various classes and remain chronically infected with HIV. Mouse models are useful in the context of identifying specific contributors to HAART-induced CVD; however, the additive effects of chronic infection and combined therapy are lost when utilizing animal models. Regardless, emerging clinical data surrounding EFV use and CVD progression highlights the need to better characterize the effects of EFV use on the vasculature, and the mouse model employed in this study provides such an opportunity.

These data taken together suggest that EFV may play a role in early vascular remodeling contributing to HAART-induced cardiovascular disease but does not independently contribute to late-stage atherosclerosis. Validation of a mouse model of EFV-induced preclinical markers of cardiovascular disease provides a platform for future studies investigating the specific mechanisms behind HAART-induced atherosclerosis.

CHAPTER 4

MECHANICALLY-MEDIATED REMODELING OF LYMPHATIC TISSUE AS A DRIVER FOR LYMPHEDEMA

4.1 Introduction

The lymphatic system is a robust network of vessels that plays a critical role in many functions including immune cell trafficking, transport of lipids from the gut to the bloodstream, and tissue fluid balance [250]. Each of these functions is directly dependent on the ability of lymphatic vessels to spontaneously and rhythmically contract to transport fluid against an unfavorable pressure gradient, a function which, if impaired, leads to lymphedema [123]. It is well known that the mechanical environment contributes significantly to their overall contractile function, leading many to study the relationship between intrinsic contractile function and mechanical cues such as magnitude and direction of flow, inlet and outlet pressure, or pressure gradient [13, 14, 141, 147]. Also directly related to contractile function is the ability of the vessel to distend appropriately in response to mechanical loading, and there have consequently been many studies characterizing the active and passive mechanical behavior of lymphatic vessels [126, 146, 153, 251]. Confocal microscopy has also been reported to characterize the microstructure of the vessel in order to provide motivation behind the mechanical responses of the vessels [150, 153].

Mechanically-mediated growth and remodeling is a well-documented phenomenon in biological tissue and is especially well-characterized in the field of vascular mechanics. However, growth and remodeling data relating to the lymphatic

vasculature is strikingly absent. Correlation between geometric changes in collecting lymphatic vessels and progression of lymphedema have only recently been reported in cancer patients [16], suggesting a possible role for growth and remodeling as an impetus for the development of lymphedema, but the mechanisms driving such remodeling are still vastly under-characterized. Models of growth and remodeling in the vascular literature suggest homeostatic shear and hoop stress states that drive remodeling behavior, thus implicating flow and pressure, respectively, as critical mediators of the process [117, 119, 121, 252]. Many fluid-structure interaction (FSI) models have been published that predict flow patterns (and consequently wall shear stress) in lymphatic vessels, but the solid mechanical properties are generally modeled empirically or without consideration for the nonlinear, anisotropic behavior of the material [152, 153, 156, 158, 159], thus reducing the accuracy of hoop stress calculations obscuring the value of potential models of mechanically-mediated lymphatic growth and remodeling. There is a pressing need for a predictive microstructurally-motivated mathematical model that captures the key characteristics of the mechanical response, namely the material non-linearity and anisotropy, in the framework of finite elasticity. Such a model represents a key step in exploiting important biomechanical frameworks for FSI and soft tissue growth and remodeling and holds the potential to advance our understanding of lymphatic function, dysfunction, and disease progression.

The purpose of this study is to develop a predictive mathematical model for passive and contractile mechanical behavior of the rat thoracic duct. We adapted our custom biaxial testing device [243] to support biaxial biomechanical testing and multiphoton microscopy of rat lymphatic vessels and performed parameter estimation

from these data for a four fiber family constitutive model and active contractile model. We describe here the incorporation of that model into an FSI model using Poiseuille flow assumptions and illustrate the role of various mechanical factors on growth and remodeling of a single lymphangion using the developed FSI model in conjunction with a simple model of volumetric growth. These illustrations motivate the need for specific experimental data to better understand the role of mechanics in lymphatic dysfunction as well as highlight key parameters that may play a role in mechanically-mediated development of lymphedema.

4.2 Milestone 1[5]: Quantify the active and passive mechanical properties of rat thoracic ducts using a microstructurally-motivated constitutive model in the context of finite elasticity.

The goal of this milestone is to characterize the mechanical behavior of rat thoracic ducts using standard biaxial biomechanical testing techniques and applying known constitutive models that account for collagen fiber angle orientation and muscle cell contraction.

---

[5] Caulk AW, Nepiyushchikh ZV, Shaw R, Dixon JB, Gleason RL. Quantification of the passive and active biaxial mechanical behavior and microstructural organization of rat thoracic ducts. Revised and resubmitted to J Roy Soc Interface. Mar 2015.

4.2.1 Methods and Materials

4.2.1.1 Vessel isolation

Male Sprague-Dawley rats (300 – 350 g) were obtained from Jackson Laboratories (Bar Harbor, ME) and kept on a 12-hour light/dark cycle in a temperature-controlled room at 22°C. The animals were housed and cared for according to the guidelines set forth the by the National Institutes of Health (NIH) for the care and use of experimental animals. All experimental procedures were reviewed and approved by the Georgia Tech Institutional Animal Care and Use Committee (IACUC). Rats were anesthetized with a combination of diazepam (2.5 mg/kg body weight) and droperidol/fentanyl (0.3 mg/kg). Both drugs were administered via intramuscular injection. After the animals reached a surgical plane, the chest cavity was opened and the thoracic duct was visualized by removing surrounding tissue and organs. Care was taken to excise the vessel from the same location each time; however, priority was given to identifying a location that was without valves or branches in order to simplify the modeling process. The vessel was carefully excised and placed in physiologic saline solution (PSS) consisting of the following constituents (in mM) at room temperature: 145.0 NaCl, 4.7 KCl, 2.0 $CaCl_2$, 1.17 $MgSO_4$, 1.2 NaH_2PO_4, 5.0 dextrose, 2.0 sodium pyruvate, 0.02 EDTA, and 3.0 MOPS (pH = 7.4 at 37°C). For passive mechanical tests, vessels were placed in Ca^{2+}-free PSS, which contained all of the same constituents as PSS with the exception of replacing $CaCl_2$ with 3.0 mM EDTA. Vessels were mounted on opposing cannula in a bath of PSS and carefully cleaned of all perivascular tissue. All chemicals were obtained from Sigma-Aldrich (St. Louis, MO).

4.2.1.2 Biomechanical testing

Single thoracic duct lymphangions (n = 6), excluding valves, were mounted on opposing glass cannula using silk suture (Figure 4.1) within a custom computer-controlled biaxial testing device [243] in PSS in a temperature controlled incubator at 37°C. The unloaded length was at least 10 times the unloaded radius and data were collected near the midpoint between mounting suture to sufficiently attenuate end effects during testing and isolate the mechanical response of a central region of the vessel. Vessels were visualized using an inverted microscope (2.5X magnification) and digital camera (Allied Vision Technologies, Marlin F-033B) while controlling the transmural pressure and axial length and recording the outer diameter and axial force measurements. Inlet and outlet pressure were measured using inline pressure transducers (Honeywell FPG 060-E418-11) and transmural pressure was calculated as the average of the inlet and outlet pressure. Outer diameter was recorded using an edge detection subroutine in Labview, axial length was controlled using linear actuators (Newport Precision LTA series) connected to the cannula, and axial force measurements were measured using a 50 g load cell (Delta Metrics 99-2636-050G). Vessels were pressurized to just above 0 cmH_2O in order to prevent collapse, and the unloaded length and diameter of each vessel was determined using a custom program in LabView. Vessels were then axially stretched to 30% beyond the unloaded length (λ = 1.3), pressurized to 3 cmH_20, and given 30-60 minutes to equilibrate to 37°C in order to establish contractility.

Figure 4.1. Typical image of a rat thoracic duct mounted for mechanical testing at an axial stretch of 1.3. Vessels were mounted such that the unloaded length was at least 10 times the unloaded radius in order to sufficiently attenuate end effects during testing.

Prior to data collection for this study, preliminary experiments were performed on five vessels to establish the experimental testing protocol. Axial force versus transmural pressure and transmural pressure versus diameter behavior demonstrated little variation for axial stretch values below 1.3; thus, the lower limit of axial stretch was chosen as 1.3. For axial stretches above 1.6, transmural pressure vs. diameter behavior became nearly linear, suggesting that collagen fibers had possibly become maximally engaged. After this transition to linear behavior, no differences were observed in transmural pressure vs. diameter behavior other than a reduction in diameter and increased slope. Thus, the upper limit of axial stretch for the testing protocol was chosen as 1.6. Also, from these preliminary experiments, vessels exhibited contractile amplitudes >25% of unloaded diameter at 3 cmH_2O and an axial stretches of 1.30; thus, vessels that exhibited a contractile amplitude of <25% of the unloaded diameter were not considered representative (e.g., due to damage during isolation and mounting) and excluded from analysis. Note that the maintenance of basal tone was not evaluated as an exclusion criterion.

Once contractility was established, isobaric contractile function was assessed at transmural pressures of 3, 6 and 9 cmH_2O. At each transmural pressure, the vessel was given a period of 5-10 minutes for equilibration. The same procedure was repeated for axial stretches of λ = 1.4 and 1.5. Temporal changes in end diastolic and systolic diameters were observed following changes in loading conditions; thus, data for analysis was taken only after the minimum and maximum diameters reached steady-state conditions.

After contractile function was assessed at fixed pressure, the PSS in the bath and the system was replaced with Ca^{2+}-free PSS, which contained all of the same constituents as PSS with the exception of replacing $CaCl_2$ with 3.0 mM EDTA, to inhibit vessel contractility and quantify the 'passive' mechanical response. Vessels were preconditioned by ramping the transmural pressure from 0 to 15 cmH_2O at axial stretch values of λ = 1.30, 1.35. 1.40, 1.45, 1.50, 1.55, and 1.60. Note that an axial stretch value of λ = 1.6 was excluded from passive testing in two samples because transmural pressure vs. diameter behavior transitioned to a linear shape at a stretch of 1.55, thus precluding the need test at higher values of axial stretch. Following preconditioning, vessels were subjected to three loading cycles of transmural pressure values from 0 to 15 cmH_2O at axial stretches identical to those during preconditioning. Plots depicting transmural pressure vs. diameter and axial force vs. pressure were generated for all fixed length conditions. Axial force versus axial length data were generated for conditions of fixed transmural pressure. Axial force data was retrieved for values of transmural pressure at intervals of 1 cmH_2O for each value of axial stretch, resulting in up to 16 curves each with 6 data points.

4.2.1.3 Multiphoton imaging

The testing device was placed on an LSM 710 META inverted confocal microscope (Zeiss) to visualize the microstructure across the entire wall of live, unfixed lymphatic vessels [112]. The vessels were imaged using a 40X / 1.3NA immersion objective (Zeiss). The vessel, maintained in Ca^{2+}-free PSS, was excited with an 800 nm two-photon laser, and collagen was visualized by detecting its second harmonic generation around 400 nm. Elastin emissions were detected by setting the META filter to a 500-550 nm bandpass configuration and using 488 nm excitation [253].

Z-stacks were collected under three loading conditions: a low-load condition (p = 3 cmH_2O, λ = 1.3), a medium-load condition (p = 9 cmH_2O, λ = 1.45), and a high-load condition (p = 20 cmH_2O, λ = 1.6 or maximum during passive testing). Orthogonal views of these z-stacks were then used to calculate vessel thickness in a loaded configuration. Unloaded vessel thickness was calculated from these values for each of the three conditions, assuming incompressibility, and the unloaded thicknesses used in modeling were calculated as the average of the unloaded thickness values determined from each of the three loading conditions.

4.2.1.4 Quantification of collagen organization

The angular distribution of collagen fibers was quantified for each optical slice of the z-stacks using a custom MATLAB® program that utilizes a fast Fourier series algorithm as described previously [110]. Using a fast Fourier transform, a power spectrum was generated in order to provide a histogram of the frequency intensities between -90° and 90° at 4° increments (reported as “Normalized Intensity”). Note that an

angle of 0° corresponds to an orientation in the axial direction. The mean fiber angle distribution was determined by taking an average of each bin across all slices in a z-stack.

4.2.1.5 Constitutive modeling

We modeled the lymphatic vessels as an incompressible, thin-walled cylinder in the framework of finite elasticity such that the Cauchy stress can be defined by equation (4.1),

$$\mathbf{T} = -p\mathbf{I} + 2\mathbf{F}\frac{\partial W}{\partial \mathbf{C}}\mathbf{F}^{\mathbf{T}} \tag{4.1}$$

where $\mathbf{T}$ is the Cauchy stress, p is the Lagrange multiplier that enforces incompressibility, $\mathbf{F}$ is the deformation gradient, W is the strain energy function, and $\mathbf{C}$ is the right Cauchy-Green strain tensors. The components of the deformation gradient and the right Cauchy-Green strain tensor for inflation and extension of an axisymmetric thin-walled tube are

$$\mathbf{F} = diag(\lambda_r, \lambda_\theta, \lambda_z) \qquad \text{and} \qquad \mathbf{C} = diag\left(\lambda_r^2, \lambda_\theta^2, \lambda_z^2\right) \tag{4.2}$$

where $\lambda_r = h/H$, $\lambda_\theta = a/A$, and $\lambda_z = \ell/L$ where h, a, and ℓ, and H, A, and L are the loaded and unloaded thickness, midwall radius, and axial length, respectively.

Conservation of mass for the incompressible solid vessel wall requires that $\det[\mathbf{F}] = \lambda_r\lambda_\theta\lambda_z = 1$, which leads to the constraint,

$$h(a+h)\ell = H(A+H)L \tag{4.3}$$

Equilibrium requires that

$$T_{\theta\theta} = \frac{Pa}{h} = \hat{T}_{\theta,act} - C_{rr}\frac{\partial W}{\partial C_{rr}} + C_{\theta\theta}\frac{\partial W}{\partial C_{\theta\theta}} \tag{4.4}$$

$$T_{zz} = \frac{f_z}{\pi h(2a+h)} = -C_{rr}\frac{\partial W}{\partial C_{rr}} + C_{zz}\frac{\partial W}{\partial C_{zz}} \tag{4.5}$$

where f_z is the axial force, P is the luminal pressure, $T_{\theta\theta}$ and T_{zz} are the mean circumferential and axial components of the Cauchy stress, respectively, $\hat{T}_{\theta,act}$ is a constitutive equation that describes the stress generated from 'active' muscle cell contraction, C_{jj} $(j = r, \theta, z)$ are the in-plane components of $\mathbf{C}$ and $W = W(\mathbf{C})$ is the strain energy density function that describes the 'passive' mechanical response. Note that $f_z = f_m + P\pi a^2$ where f_m is the force measured by the load cell during testing, and the second term accounts for the end cap pressure. Due to the very small thickness of the vessel wall (average unloaded thickness of approximately 30 microns), a two-dimensional framework was utilized such that stresses in the radial direction were assumed to be negligible in comparison to circumferential and axial stress.

We considered the four-fiber family strain energy density function of Baek et al. [254] which was adapted from the original function described by Holzapfel et al. [108]; namely,

$$W = b(I_C - 3) + \sum_{k=1,2,3,4} \frac{b_1^k}{4b_2^k}\{exp[b_2^k((\lambda^k)^2 - 1)^2] - 1\} \tag{4.6}$$

where b, b_1^k, and b_2^k are material parameters, $I_C = tr(\mathbf{C}) = C_{rr} + C_{\theta\theta} + C_{zz}$ is the first invariant of $\mathbf{C}$, $(\lambda^k)^2 = C_{\theta\theta}\sin^2(\alpha^k) + 2C_{\theta z}\sin(\alpha^k)\cos(\alpha^k) + C_{zz}\cos^2(\alpha^k)$ is the stretch of the k^{th} fiber family, and α^k is the angle between the axial and fiber directions. For inflation and extension tests (given appropriate material symmetry), $C_{\theta z} = 0$, so that $(\lambda^k)^2 = C_{\theta\theta}\sin^2(\alpha^k) + C_{zz}\cos^2(\alpha^k)$. We assume that fiber families one and two correspond to fibers oriented in the circumferential and axial directions, respectively, and are therefore prescribed as opposed to calculated. We also assume material symmetry

such that, $\alpha^3 = -\alpha^4 \equiv \alpha$ and $b_1^3 = b_1^4$ and $b_2^3 = b_2^4$. Thus, equation (4.6) contains seven material parameters (b, b_1^k and b_2^k with k = 1,2,3) and one structural parameter (α).

We employed the model of Rachev and Hayashi [111] for the active stress due to muscle cell contraction; namely,

$$\hat{T}_{\theta,act} = T_{act}\lambda_\theta \left[1 - \left(\frac{\lambda_M - \lambda_\theta}{\lambda_M - \lambda_0}\right)^2\right] \tag{4.7}$$

where T_{act} is a parameter dependent on the activation of the muscle cells, λ_M is the stretch at which the muscle contraction is maximum, and λ_0 is the stretch at which muscle-induced force generation ceases. Due to both tonic and rhythmic contraction of lymphatic muscle cells, the parameter T_{act} was calculated for conditions describing the basal tone as well as the systolic contraction of the vessel, resulting in separate curves depicting maximum and minimum states of active contraction governed by equations $T_{act}^{max} = T_{act}^{bas} + T_{act}^{sys}$ and $T_{act}^{min} = T_{act}^{bas}$, where T_{act}^{bas} is the material parameter governing active stress in a diastolic state and T_{act}^{sys} is the material parameter that governs the addition of active stress during systolic contraction. Note that "maximum" here refers to a physiologic systolic state and not maximal contraction as defined by applying depolarization solution together with a strong lymphatic muscle agonist, and "minimum" refers to a physiologic diastolic (or basal) state.

T_{act}^{bas} was calculated as a function of pressure to support the observation of a myogenic response. Constant values of T_{act}^{bas} were determined for each loading condition, resulting in three values of T_{act}^{bas} and three values of pressure. A linear regression was performed on the data to determine values for parameters a and b following the form $T_{act}^{bas} = f(P) = aP + b$, thus characterizing T_{act}^{bas} (and consequently T_{act}^{max}) as a function

of pressure. In some cases, regression yielded a nearly vertical line due to almost identical maximum radii in the diastolic condition, and therefore one point was excluded from the regression so as to ensure that calculated parameters indicated a positive linear relationship between T_{act}^{bas} and pressure. Following linear regression, the MATLAB® subroutine `lsqnonlin` was used to calculate T_{act}^{bas} for a range of pressure values for the purpose of plotting theoretical curves. A minimum of $-b/a$ was imposed on the solver to prevent predictions of negative active stress.

4.2.1.6 Parameter estimation

The passive mechanical parameters and structural parameter were determined using the MATLAB® non-linear regression function `lsqnonlin` and minimizing the error function

$$e = \frac{1}{2n}\left\{\sum_{i=1}^{n}\left(\frac{P_{model}^{i} - P_{exp}^{i}}{\bar{P}_{exp}}\right)^2 + \sum_{i=1}^{n}\left(\frac{f_{model}^{i} - f_{exp}^{i}}{\bar{f}_{exp}}\right)^2\right\} \tag{4.8}$$

where n equals the number of data points acquired during biaxial testing, P_{model}^{i} and f_{model}^{i} are the model prediction of pressure and axial force values for data point n, determined from equations (4.4) and (4.5), with T_{act}=0 (and thus, $\hat{T}_{\theta,act}$=0). P_{exp}^{i} and f_{exp}^{i} are the measured pressure and axial force for data point n. $\bar{P}_{exp}$ and $\bar{f}_{exp}$ are the average pressure and axial force values over all data points.

After the passive parameters were determined via regression with the passive data, the values of T_{act}^{sys} and T_{act}^{bas} were determined by minimizing equation (4.7) to the maximal contraction occurring during systolic contraction ($T_{act} = T_{act}^{sys}$) and minimum contraction occurring during diastolic relaxation ($T_{act} = T_{act}^{bas}$) at pressure values of p =

3, 6, and 9 cmH_2O. The parameter λ_M was prescribed as the maximum circumferential stretch achieved during passive testing plus 5%. The parameter λ_0 was prescribed as 5% less than the minimum circumferential stretch achieved during active testing. These parameters were prescribed in order to capture the entire working range of active contraction. All parameter values are reported for individual samples as well as in the form of the mean ± standard error of the mean (SEM).

4.2.2 Results

4.2.2.1 Passive and active mechanical response

Average unloaded thickness was 32.2 ± 1.60 μm, the average unloaded length was 3.573 ± 0.173 mm, and the average unloaded radius was 240 ± 10.9 μm, respectively (Table 4.1); thus, the radius-to-thickness ratio of 13% in the unloaded thickness supports the thin wall assumption and the diameter-to-length ratio suggests that end effects may be neglected within a central region of the vessel (see Figure 4.1). Loaded geometry was used to determine unloaded thickness from the incompressibility assumption. Standard errors associated with the calculation of unloaded thicknesses, based on measurements from the low, medium, and high loading scenarios, averaged 2.67 μm, which is 8% of the mean unloaded thickness, and suggests that incompressibility may be a reasonable assumption. For a single value of axial stretch, the amplitude of spontaneous contractions decreased (i.e. the vessel becomes more like a conduit) as transmural pressure increased (Figure 4.2). Contractile amplitude was markedly diminished upon increasing axial stretch from λ = 1.3 to 1.5 (Figure 4.2C); contractile frequency, however, was not diminished (data not shown).

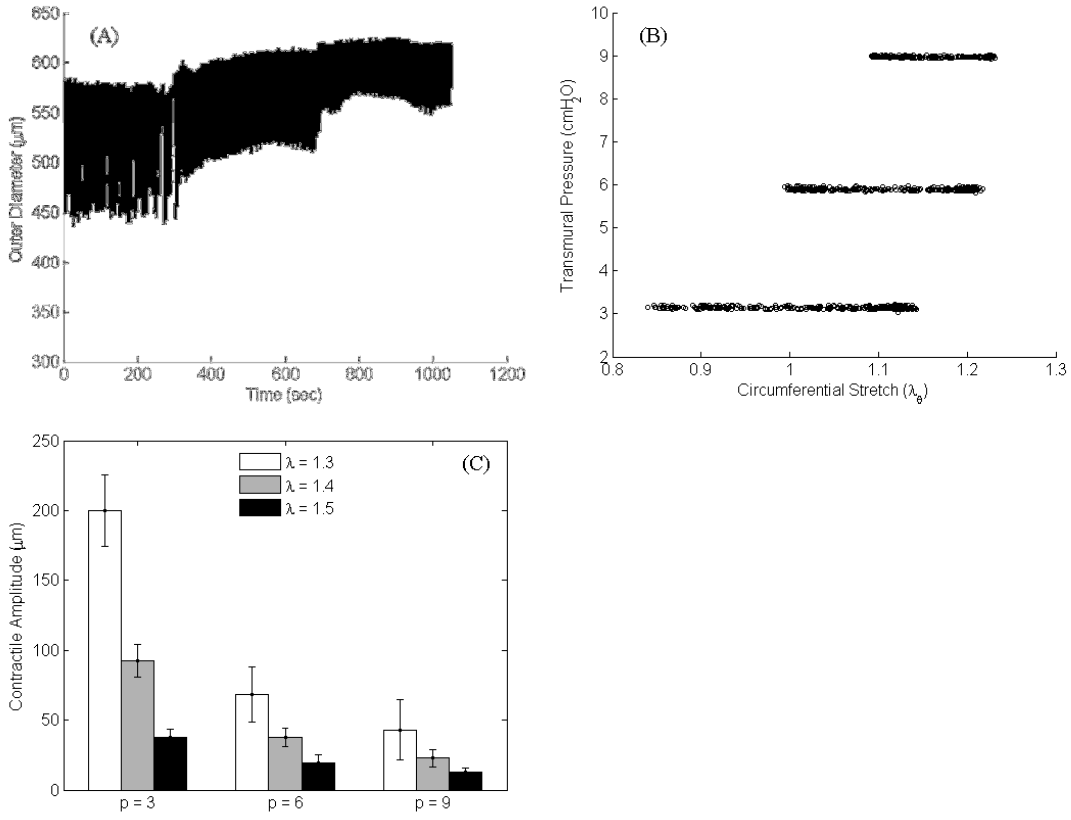

Figure 4.2. Contractile amplitude of lymphatic vessels as a function of time, transmural pressure, and axial stretch. (A) Active diameter measurements for specimen 5 reveal a time-dependent contractile response following changes in transmural pressure at an axial stretch of 1.3. (B) Transmural pressure vs. circumferential stretch for specimen 5 at an axial stretch of 1.3. Contractile amplitude decreases as transmural pressure increases. End diastolic stretch increases to a lesser degree than end systolic stretch (less than 10% vs. more than 30%, respectively). Note that this plot corresponds to the time-dependent data in panel A. Data was included only after diameter measurements reached an equilibrium following changes in loading conditions. (C) Contractile amplitude data for all specimens at 3 values of transmural pressure and 3 values of axial stretch. Note that contractile amplitude was markedly decreased at axial stretch values of 1.4 and 1.5 compared to 1.3. Data are reported as the mean ± SEM.

Table 4.1. Measurements and calculations of loaded and unloaded geometry for individual rat thoracic ducts. Vessels were mounted on a biaxial testing device and oriented in a stress-free condition. Unloaded length and outer radius were determined using a custom LabView program. Loaded thicknesses from three loading conditions were determined using confocal microscopy. The loading conditions consisted of low (p = 3 cmH_2O, λ = 1.3), mid-range (p = 9 cmH_2O, λ = 1.45), and high loading (p = 20 cmH_2O, λ = 1.6 or highest stretch value during passive testing) corresponding to h_{low}, h_{mid}, and h_{high}, respectively. Unloaded thickness (H) was calculated by applying the known loaded and unloaded geometry to the incompressibility assumption and averaging the unloaded thickness calculations from the low, mid, and high loading conditions. SEM for each calculation of the average unloaded thickness is also reported.

	L (mm)	R_o (μm)	h_{low} (μm)	h_{mid} (μm)	h_{high} (μm)	H_{ave} (μm)	SEM_H (μm)
1	3.345	252	18.2	16.0	14.8	33.7	3.56
2	3.742	200	17.1	16.0	12.5	24.9	4.12
3	4.112	220	19.4	17.1	14.8	36.8	2.75
4	4.057	230	17.1	14.8	14.8	33.1	0.76
5	3.170	260	21.7	19.4	18.2	29.6	2.92
6	3.013	280	21.7	18.2	16.0	35.0	1.89
Average	3.573	240	19.2	16.9	15.2	32.2	2.67
SEM	0.173	10.9	0.78	0.63	0.69	1.60	0.45

Passive mechanical behavior was observed and showed a stiffening response with increasing axial stretch, typical of soft tissues from the vasculature (Figure 4.3). Axial force measurements had little variation at the lower values of axial stretch but generally increased to maximum force values ranging from 4 to 15 mN at the highest stretch values. Qualitatively, isobaric axial force versus axial stretch curves consistently intersect at axial stretch values between 1.3 and 1.4; the intersection of isobaric axial force-stretch curves a characteristic response observed in blood vessels and often ascribed as the *in vivo* axial stretch [112, 255]. We did not measure the *in vivo* axial stretch of the rat thoracic ducts during excision; however, an axial stretch of 1.4 seems reasonable based on our qualitative observations.

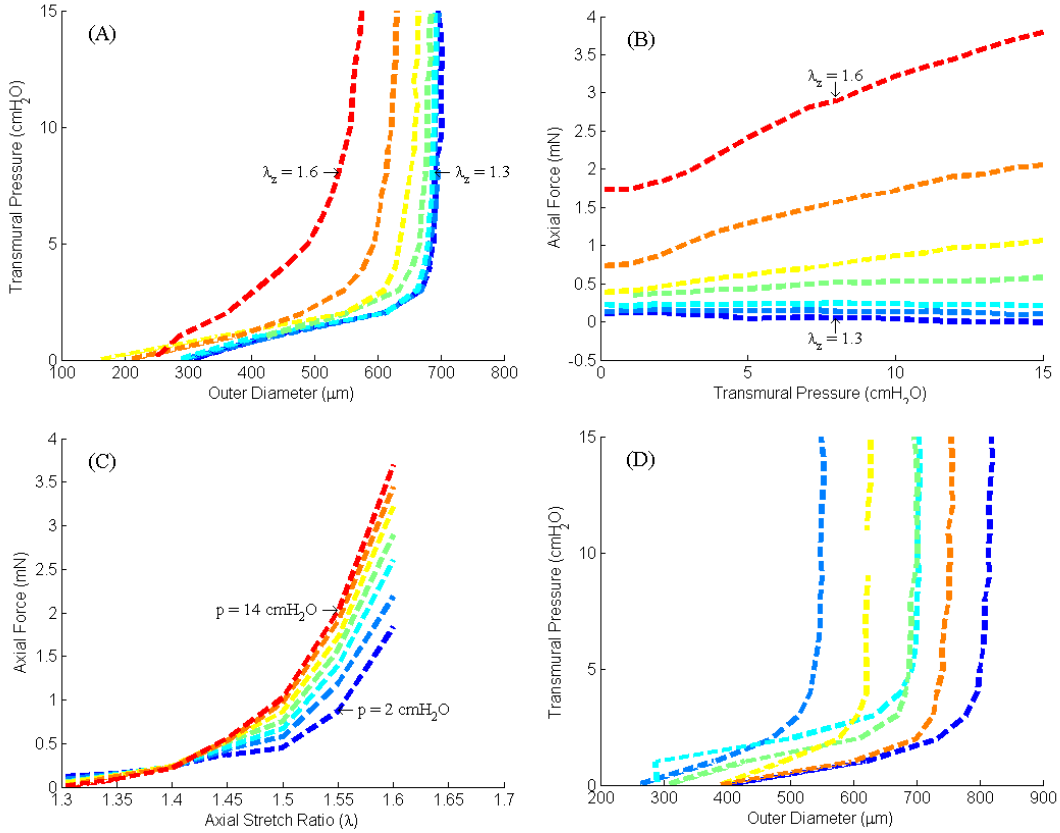

Figure 4.3. Passive mechanical testing data for specimen 4 and transmural pressure vs. diameter data for all 6 specimens at an axial stretch of λ = 1.3. Transmural pressure vs. diameter (A) and axial force vs. transmural pressure (B) show progressive stiffening as axial stretch is increased. Lowest and highest values of axial stretch are denoted by arrows. (C) Isobaric axial force vs. axial length curves for specimen 4. The The intersection point of the curves has previously been used to estimate the in vivo axial stretch of arteries. (D) Transmural pressure vs. outer diameter data for 6 thoracic ducts at an axial stretch of 1.3. Note the large variability in geometry between samples. The maximum diameter for the largest vessel is approximately 50% larger than that of the smallest vessel (~800 μm compared to ~530μm).

4.2.2.2 Material parameter calculation

Non-linear regression yielded material parameters that provided a good fit of the passive mechanical testing data (Table 4.2 and Figure 4.4). In general, the majority of the error in the passive fits appeared to occur either in the toe region of the plots where the collagen fibers become engaged or in the higher values of axial stretch in which collagen fibers appear to be constantly engaged.

Regression yielded material parameters that provided a good fit of the contractile testing data (Table 4.3 and Figure 4.5). Average errors were calculated using Equation 8, and the values associated with the active parameters T_{act}^{max} and T_{act}^{bas} were 6.6 ± 2.6% and 6.8 ± 3.4%, respectively. The parameter a provides physical insight into the dependence of the basal parameter on transmural pressure. Calculation of this parameter showed relatively consistent basal tone in all samples with the exception of specimen 5, which had very little dependence on transmural pressure. Although a myogenic response was absent from this specimen, we believe this to be an indication of the variability in lymphatic behavior rather than an outlier in the data set, since the contractility for that specimen met the inclusion criteria defined in the methods. Note also that for specimen 3, a single data point was excluded from the error calculation in the basal condition due to a skewed error calculation. The inaccuracy was affected by the large slope of the basal curve (thus a very large change in transmural pressure is required for modest changes in diameter). Eliminating this data point from the error calculation had little effect on the theoretical transmural pressure vs. diameter curve for specimen 3.

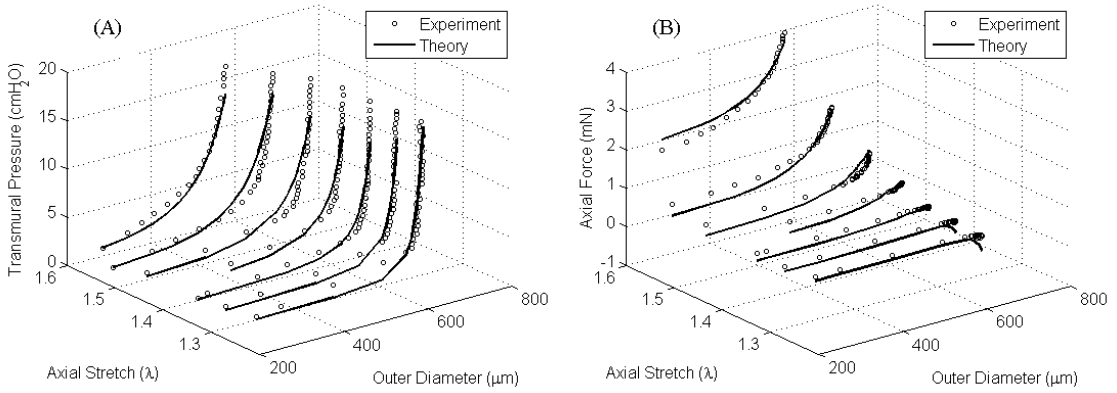

Figure 4.4. Illustrative plots from parameter fitting results for specimen 4 using a four-fiber constitutive model. (A) Transmural pressure vs. diameter plot for a range of axial stretch values. (B) Axial force vs. diameter plot for a range of axial stretch values. Note that axial force values in the modeling process exclude contributions from end cap pressure (i.e. f_m is reported rather than f_z). Open circles denote experimental data and solid lines denote theoretical predictions.

Table 4.2. Passive material parameter calculations for rat thoracic ducts using a four-fiber constitutive model. Data are reported as the mean ± SEM. The family of parameters b_1^k exhibit a much higher degree of variability than the family of parameters b_2^k. The structural parameter exhibits consistency, and all parameters yield error values that suggest reasonable fits of the experimental data.

	b (dyne/cm^2)	b_1^1 (dyne/cm^2)	b_2^1	b_1^2 (dyne/cm^2)	b_2^2	b_1^3 (dyne/cm^2)	b_2^3	α (degrees)	Error (%)
1	0.00018	2253	0.8694	4629	2.214	427.7	4.0938	27.7	6.730
2	661.6	19990	1.4624	0.00011	11.02	1899	4.6244	25.5	9.919
3	0.00015	501.8	1.1838	1125	1.942	2852	1.9431	27.7	7.540
4	0.00037	242.6	2.2181	60.12	3.267	1839	2.6113	33.5	8.677
5	0.01320	16080	7.4201	33410	1.745	5396	5.1123	32.7	13.01
6	0.00390	2027	4.4631	190930	0.3119	53.37	6.6564	39.5	7.740
Average	110.3	6849	2.9362	38359	3.417	2078	4.1736	31.1	8.936
SEM	100.7	3275	0.9497	28267	1.433	717.2	0.6384	1.9	0.848

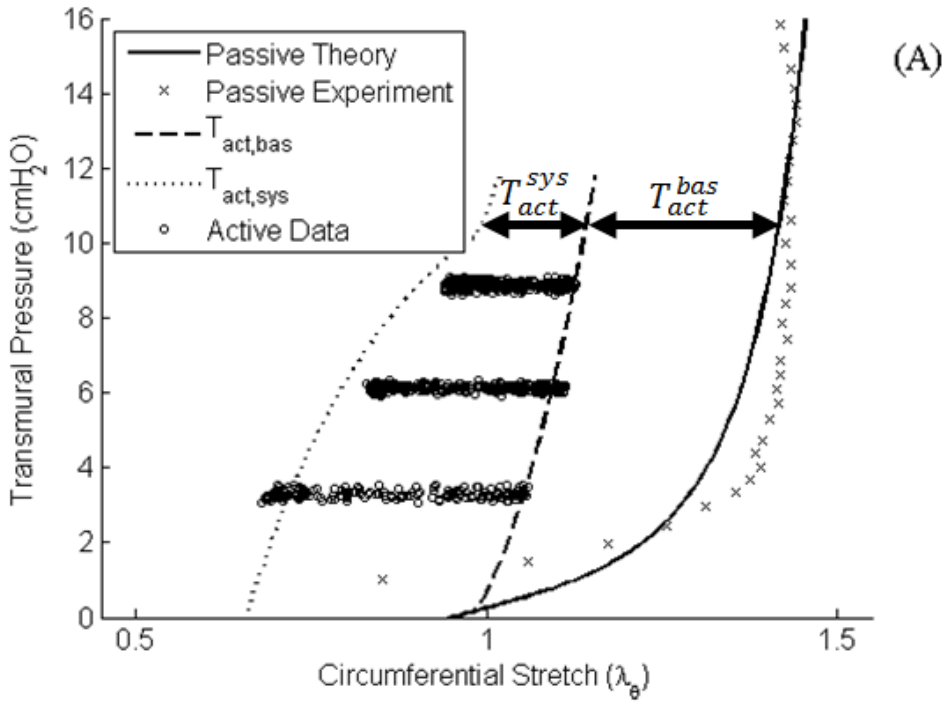

Figure 4.5. Model simulations of transmural pressure vs. circumferential stretch behavior for specimen 2 at an axial stretch value of λ = 1.3. Theoretical simulation of transmural pressure vs. circumferential stretch behavior was calculated from the combination of passive plus active stress and provides a good fit of the active data. Contributions to the behavior from the basal (dashed line) and systolic (dotted line) parameters are denoted on the graph. Note that the maximal systolic condition is determined by the summation of the basal and systolic contributions.

Table 4.3. Active material parameter calculations for rat thoracic ducts. Slope and intercept values for T_{act}^{bas} were determined using linear regression. The parameters λ_M and λ_0 were prescribed based on experimental data. (†) Denotes sample with a single data point removed from error calculation. Removal of data point was due to the large slope of the basal curve resulting in excessively high errors that skewed the interpretation of the data. Removal of data point had no effect on parameter calculation or estimation of total stress. Data are reported as the mean ± SEM.

	$T_{act,sys}$ (dyne/cm^2)	λ_M	λ_0	a	b(dyne/cm^2)	$Error_{sys}$ (%)	$Error_{bas}$ (%)	
1	118620	1.7636	0.6119	13.0981	-4574.4	2.030	21.26	
2	134500	1.4923	0.6125	11.5804	-1954.3	18.99	1.330	
3	100140	1.7600	0.7685	11.4275	-5990.1	6.130	0.990	†
4	96680	1.6617	0.6541	11.9908	-1354.1	2.320	14.82	
5	91331	1.2957	0.7719	0.0447	13401	0.405	0.004	
6	79184	1.4575	0.6641	11.3276	1480.0	9.770	2.370	
Average	103409	1.5718	0.6805	9.9115	168.017	6.608	6.796	
SEM	7429	0.0699	0.0271	1.8175	2603.8	2.589	3.345	

4.2.2.3 Collagen and elastin organization

A single outer layer of collagen and a single inner layer of elastin were consistently identified in all samples using confocal microscopy (Figure 4.6). Similar observation of the layered structure of lymphatic vessels was reported by Arkill et al. [150]. The fluorescence spectrum of elastin revealed a 'fiber family' oriented nearly circumferentially and another oriented nearly longitudinal. Collagen fibers showed a more undulated morphology at lower loading conditions and appeared to recruit fibers more gradually throughout the loading process, compared to elastin. Despite consistency in the elastin fiber orientations, significant differences in collagen fiber distributions were observed across samples, with all samples exhibiting differing degrees of material asymmetry (Figure 4.7).

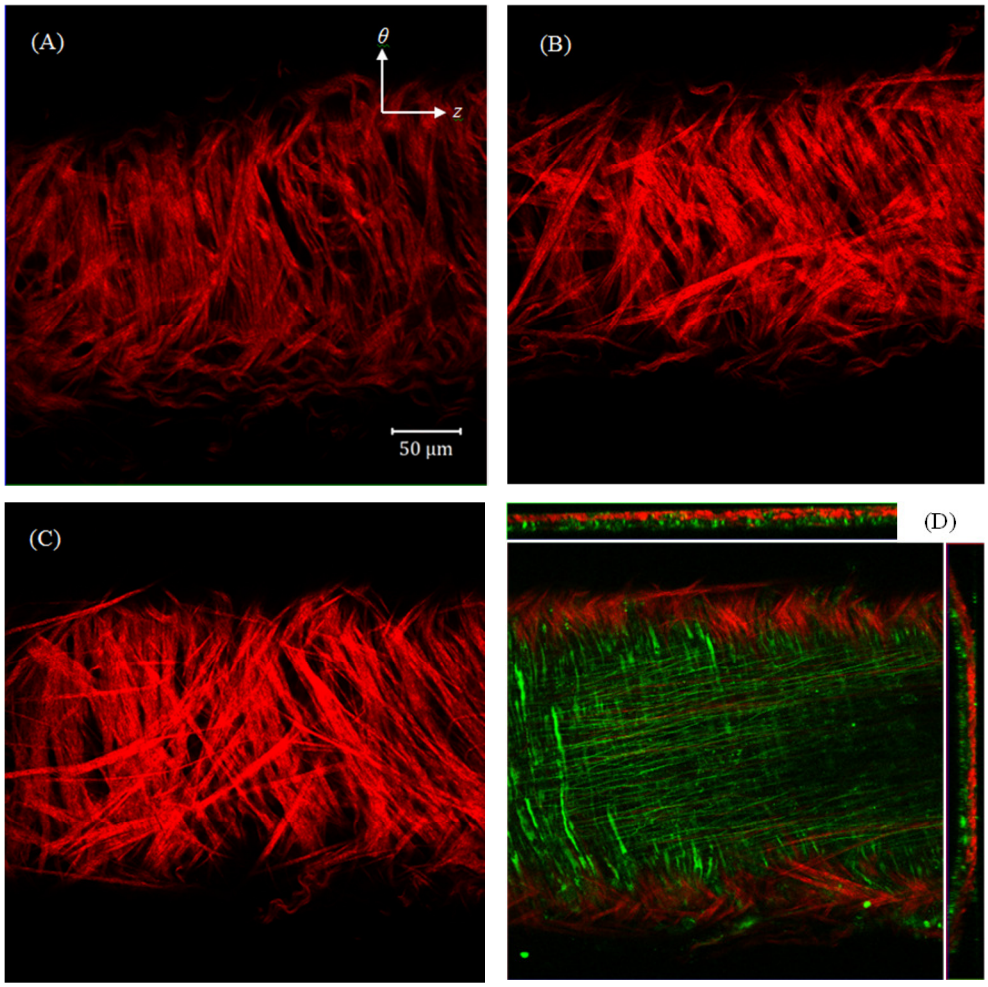

Figure 4.6. Representative multiphoton images of specimen 3 at low, mid, and high loading conditions (A-C, respectively). Multiple images were taken in order to produce a three-dimensional representation of the vessel wall. Collagen fibers are denoted by red and elastin fibers are denoted by green. Note the presence of small, elongated elastin fibers and the much larger collagen fibers that have a wavier morphology. Scale and orientation are denoted in (A). (D) Representative orthogonal image of a vessel under high loading conditions including both collagen and elastin. The layered structure and curvature of the vessel are evident. Thickness of the vessel was determined from the cross-sectional view depicting the curvature.

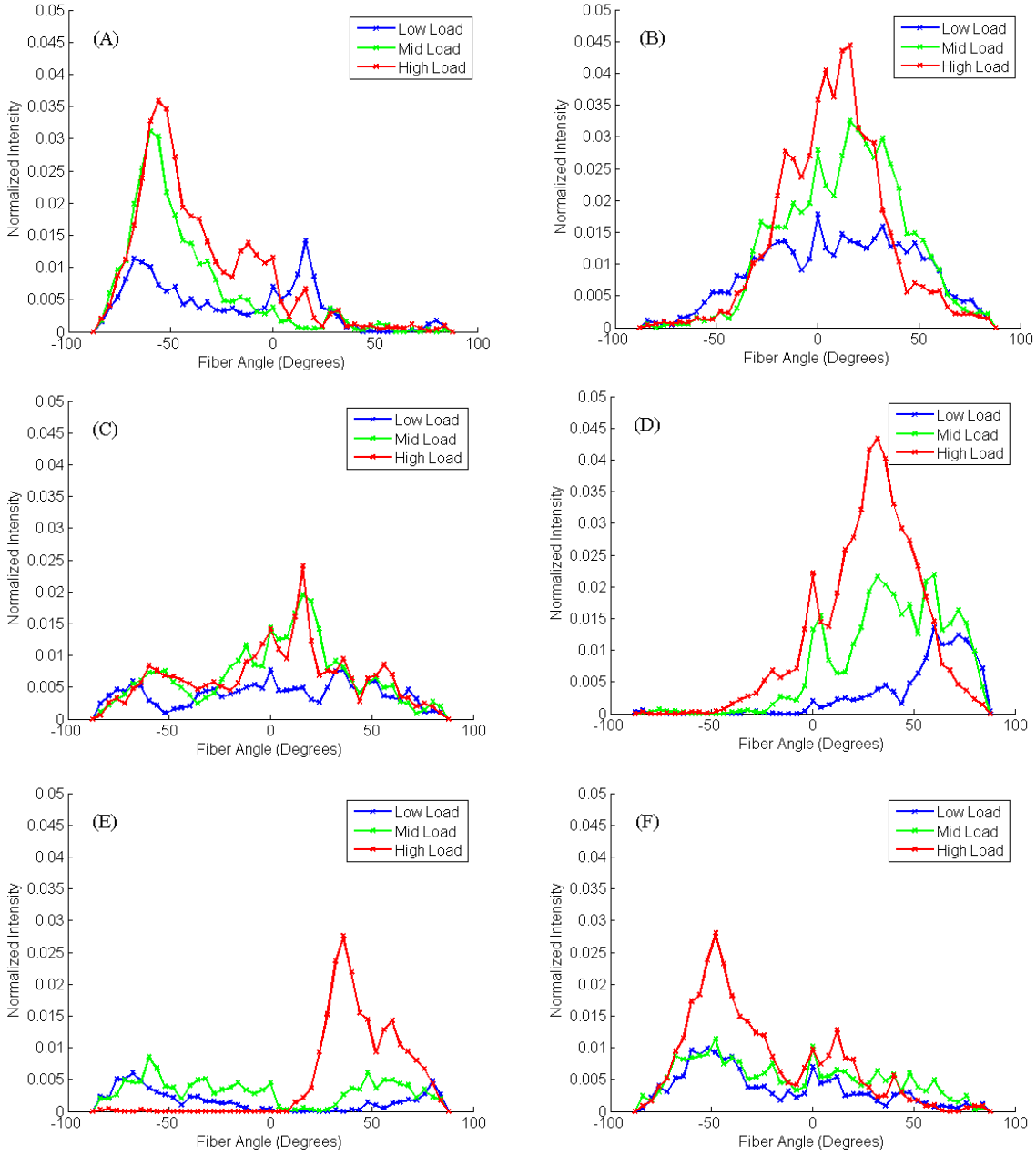

Figure 4.7. Frequency intensity plots for low-, mid-, and high-loading conditions as a function of orientation angle for six rat thoracic ducts (A-F for specimens 1-6, respectively). An angle of 0 degrees denotes an orientation in the axial direction. Primary angle orientations were easily identified by a large peak in frequency intensity. Peaks associated with secondary angles were more difficult to interpret. Data suggests that material asymmetry exists in all specimens. Note that the highest normalized intensity values occur in the high loading conditions of every specimen, indicating increased alignment of collagen fibers as loading conditions are increased.

4.2.3 Discussion

Lymphatics play a key role in a diverse set of physiological functions, including tissue fluid balance, lipid absorption, and immune cell trafficking. As is the case for other soft tissues, mechanically-mediated biological mechanisms likely play a central role in lymphatic function (or dysfunction) and disease progression. Experimental studies have shown that lymphatic contractility is altered following changes in transmural pressure [145, 146] and changes in axial pressure gradients [13, 141], and clinical data has shown that lymphedema leads to dramatic changes in lymphatic vessel geometry (e.g. thickness, radius, lymphatic muscle hyperproliferation) [16]. While it is well known that tissues remodel in response to changes in their local mechanical environment, altered loading conditions such as those found in lymphedema have yet to be directly linked. To study mechanically-mediated remodeling of lymphatics, accurate quantification of the local mechanical environment of lymphatics is required; however, a critical gap remains in quantifying the biaxial mechanical response of lymphatic tissue and modeling the mechanical behavior in a framework that allows quantification of the local mechanical environment for relevant applied loads and vessel geometries. Such a model represents a critical step in the investigation of mechanically-mediated dysfunction and disease progression. To that end, we have identified material parameters, combining the models from Baek et al. [254] and Rachev and Hayashi [111], to accurately describes the mechanical behavior of rat thoracic ducts to passive cylindrical biaxial testing and spontaneous contraction.

4.2.3.1 "Microstructurally-motivated" passive constitutive model

The functional forms of the constitutive equations were motivated by the tissue microstructure; however, microscopy revealed both consistencies and inconsistencies between the microstructure captured in the constitutive model and that observed in the tissue. First, although elastin is often modeled as an isotropic material [109, 110, 119, 256], elastin imaging revealed nearly circumferentially and nearly axially oriented fibers. Second, although we did not quantify their organization, there are nearly circumferentially oriented smooth muscle cells. Third, we observe collagen fibers oriented at off-axis angles. Fourth, in addition to these elastin structural components, collagen structural components, and smooth muscle cells, an amorphous, presumably isotropic mechanically significant solid, likely containing proteoglycans, glycosaminoglycans, water, and other ECM constituents, exists in which these structural components are embedded. Thus, the proposed four-fiber family model (Equation (4.6)) captures many of the key salient features of the observed microstructure. Namely, the axially fiber family captures, the contribution from the axially oriented elastin structural element (and perhaps the contribution from axial collagen components), the circumferential fiber family captures the combined role of passive smooth muscle and the circumferentially oriented elastin structural element (and perhaps the circumferential collagen components), the fiber-families at $\pm\alpha$ capture the combined contribution of collagen fibers oriented off axis, and the isotropic term captures the contribution from the amorphous solid.

There are, however, several important inconsistencies between our microstructurally-motivated constitutive model and the observed microstructure. For

several vessels, the collagen fiber distributions were asymmetric, often with a single peak oriented off-axis (see Figure 4.7), suggesting material asymmetry. To accurately identify material parameters for an asymmetric material requires one to quantify both the shear strains and the torsional load during fixed length pressurization; more rigorously, one should also perform torque-twist tests on the tissue [257]. Although quantifying shear strains can be done via tracking of markers or particle image velocimetry, the measurement of applied torque is technically challenging and has not been reported for tissues of this caliber. Without this torsion boundary condition, proper analysis to identify material parameters for a proposed asymmetric constitutive model cannot be performed. Indeed, other asymmetries are also apparent; namely, the elastin fibers and smooth muscle cells are not oriented at exactly 0- and 90-degrees. Note that material asymmetries exist in most arteries, yet rarely are torsional loads quantified (particularly in small caliber vessels) and rarely are these material asymmetries incorporated into the functional form of the constitutive model, perhaps because the nominal values and biological significance of these shear strains and stresses are thought to be of secondary importance, compared to the normal strains and stresses. Thus, although our model is motivated by microstructure, we do not use measured microstructure as an input to the constitutive model. Despite the technical challenges required for such an effort, the results herein motivate the need for incorporating microstructural measurements into the constitutive model [110] and quantifying relevant boundary conditions and deformations so that such modeling efforts may be performed.

4.2.3.2 Sample-to-sample variations and material heterogeneity

We observed significant variations in mechanical response (Figure 4.3) and material parameters (Table 4.2 and Table 4.3), geometry (Table 4.1), and microstructural organization (Figure 4.7) across samples; such variability is not uncommon in the lymphatic circulation [143, 144, 258]. Loaded thicknesses in rat thoracic ducts reported in the literature are consistent with the present data [144, 153]; geometric and functional parameters generally show large standard errors, suggesting large sample-to-sample variations. Similarly, others have used confocal microscopy to quantify angle orientation in bovine mesenteric lymphangions, and report similar variability to that reported herein [150]. Geometric variability in human thoracic ducts as a function of longitudinal position has been reported [258] and we (data not shown) and others have reported heterogeneities in the microstructural organization along the length of a single lymphangion [153].

Such heterogeneities and sample-to-sample differences in geometry, microstructure, and mechanical behavior render quantifying a unified constitutive model for the rat thoracic duct challenging. Indeed, it further motivates the need for a constitutive model that links microstructural measurements to the tissue-level mechanical response. The goal of this milestone was to isolate the mechanical behavior of a central, nearly homogeneous region of a lymphangion, quantify the deformation and boundary conditions for this central region, identify an appropriate constitutive model for this homogeneous region that captures well the tissue level mechanical response, and quantify the microstructure of the same region. We submit that an accurate constitutive equation that links the microstructural architecture to the tissue-level biomechanical behavior for a

homogeneous region is a required first step, before the material heterogeneities can be accurately modeled.

4.2.3.3 Sample-to-sample variations in passive material parameters

Passive parameters obtained via non-linear regression spanned multiple orders of magnitude (Table 4.2); such variations may be due to several factors. First, given that we observed significant sample-to-sample variations in the mechanical response, geometry, and microstructural organization, it is perhaps not surprising that there were also large variations in material parameters obtained via non-linear regression. Second, identification of material parameters for exponential constitutive models, via regression to biaxial mechanical testing data, often results in large deviations across samples [112, 259, 260], even when sample-to-sample variations in mechanical behavior is low; non-uniqueness may be a factor [108, 261]. Note, however, we were unable to identify models with fewer material parameters (e.g., two or three fiber-family models) that provided an adequate fit to data. All parameters were restricted to be positive, however, since our goal was to identify a model that provided the best fit to data, no other restrictions were placed on their value; we also surveyed a broad range of initial guesses during regression to ensure that a global minimum was identified. Restricting the values of material parameters in order to ascribe a more physical meaning and microstructural motivation to each may be an opportunity for future work [122].

4.2.3.4 Model spontaneous contraction and basal tone

Lymphatic muscle cells have characteristics in common with both smooth muscle cells, which exhibit tonic contraction, and cardiac muscle, which exhibit rapid and spontaneous contraction [125, 149]; both characteristics are observed here and are

captured in the active model. The contraction results suggest that the maximum contraction is captured well by the functional form of Rachev and Hayashi, but that the basal tone that occurs during the resting phase exhibited a pressure (or strain) dependencies, beyond that captured from the strain-dependent response captured in Equation (4.7); modeling a linear dependency between the basal parameter and transmural pressure provided a reasonable fit to data. In general, material parameters should not be prescribed as a function of applied loads (e.g., pressure), but rather as a function of an appropriate strain measure; this is a limitation of the current active model. However, with the data reported herein, at fixed length (i.e. fixed axial strain), the diastolic diameter (and circumferential strain) remained nearly constant with increasing pressure, presumably due to a myogenic response from the muscle cells; such singularities prohibit relating basal tone to strain using the original model in Equation (4.7) because the model cannot produce the highly nonlinear behavior necessary to recapitulate maintenance of load-dependent tone without prescribing unrealistic values for the parameters λ_M and λ_0. Davis et al. reported myogenic responses in rat lymphatic vessels that are time-dependent following a step-change in transmural pressure [142] and reported a decrease in maximum diastolic diameter following an increase in afterload [13] in the rat mesentery. Gasheva et al. have reported increases in end diastolic diameter of rat thoracic ducts due to pumping-induced production of nitric oxide [124]. Further, these data suggest that contraction amplitude (Figure 4.7) and frequency (not shown) are highly dependent on the axial stretch; however, the current active model does not consider such axial dependencies. Developing a new functional form for the active stress as a function of appropriate circumferential and axial strain measures and material

constants (and performing a broader range of theoretically-motivated experiments to quantify these material constants for lymphatic vessels) should be a target of future work.

Taken together, these findings provide a framework for future investigations targeting lymphatic growth and remodeling as it relates to the progression of diseases such as lymphedema. Given that an important role of the lymphatic system is the transport of fluid from tissues to the venous system, many functional parameters that have been quantified in the literature relate directly to the ability of the vessels to transport fluid (e.g. contractile amplitude and contractile frequency). It is unknown how these functional parameters may be affected by the internal forces experienced in these vessels, and it therefore remains necessary to quantify these forces. It is well known that mechanical factors such as transmural pressure, stretch, and flow direct tissue growth and remodeling [118, 119, 121, 122, 252], and quantification of stresses in lymphatics will provide a foundation for simulating growth and remodeling in an effort to quantify the effect of mechanically-mediated geometrical changes on common functional parameters describing contractile behavior. This proposed model is the first to successfully simulate both the active and passive behavior of a lymphatic vessel using a microstructurally-motivated model and provides potential for long-term predictions of mechanically-mediated maladaptive remodeling as well as identification of primary parameters contributing to the development of diseases relating to the lymphatic vasculature.

4.3 Milestone 2: Establish a novel predictive framework characterizing the relationship between mechanically-mediated lymphatic growth and remodeling and time-dependent lymphatic pumping function in order to identify key parameters driving progression of lymphedema.

The goal of this milestone is to characterize lymph transport through a single actively contracting rat thoracic duct using experimentally-determined parameters from Milestone 1 in conjunction with a model of Poiseuille flow and adaptations of previously published models of volumetric mechanically-mediated growth and remodeling in order to identify potential key parameters driving the progression of lymphatic dysfunction and lymphedema.

4.3.1 Methods and materials

Constitutive model. Given the sufficiently small nature of lymphatic vessels, it is appropriate to begin mathematical modeling with the simple two-dimensional framework as described in section 4.2.1. We can consider a single lymphangion as a long, straight tube subjected to a prescribed luminal pressure and axial load. In the 2-D case, average stress values serve as suitable representations for the intramural stresses within the vessel because we assume the wall to be a thin membrane. We can impose a luminal pressure and axial load, and we can easily measure the outer radius of the vessel. Given isochoric deformation, it is then easy to calculate the inner radius and wall thickness in the loaded configuration, making experimental stress calculations straightforward.

For constitutive modeling, the Cauchy stress can be expressed as a function of the deformation gradient and the strain energy function following equation (4.2). For this case, we consider the deformation gradient to be expressed as

$$\boldsymbol{F} = \begin{bmatrix} \frac{\partial r}{\partial R} & \frac{1}{R}\frac{\partial r}{\partial \Theta} & \frac{dr}{dZ} \\ r\frac{\partial \theta}{\partial R} & \frac{r}{R}\frac{\partial \theta}{\partial \Theta} & r\frac{\partial \theta}{\partial Z} \\ \frac{\partial z}{\partial R} & \frac{1}{R}\frac{\partial z}{\partial \Theta} & \frac{\partial z}{\partial Z} \end{bmatrix} = \begin{bmatrix} \frac{\partial r(R)}{\partial R} & 0 & 0 \\ 0 & \frac{r\pi}{R\Theta_0} & 0 \\ 0 & 0 & \lambda\Lambda \end{bmatrix} = \begin{bmatrix} \lambda_r & 0 & 0 \\ 0 & \lambda_\theta & 0 \\ 0 & 0 & \lambda_z \end{bmatrix}$$

where r and R are the loaded and unloaded midwall radius, respectively, at an arbitrary point within the vessel wall, Θ_0 is the opening angle of the vessel after making a radial cut in the unloaded vessel (defined by Chuong and Fung [103]), λ and Λ are the loaded and unloaded lengths, respectively, and λ_r, λ_θ, and λ_z are the mean in-plane stretch ratios in the radial, circumferential, and axial directions, respectively. Note that the off-diagonal components are zero because we assume no shear deformation in an *in vitro* testing environment. For a normal carotid artery, residual stresses exist within the wall until a radial cut in a cross-sectional segment is made, allowing the vessel to spring open and create what is commonly called an opening angle. No data currently exists regarding opening angles of lymphatic vessels, so we have here assumed that there are no residual stresses within the wall of the vessel and consequently no opening angle, thereby reducing the in-plane circumferential component of the deformation gradient to $\lambda_\theta = r/R$. We consider this a reasonable assumption based on the sufficiently small thickness-to-radius ratio observed in the previous section (approximately 13%).

For the passive mechanical behavior of lymphatic vessels, we considered the four-fiber family strain energy density function in equation (4.6). We assume that fiber families one and two correspond to fibers oriented in the circumferential and axial directions, respectively, and are therefore prescribed as opposed to calculated. We also assume material symmetry such that, $\alpha^3 = -\alpha^4 \equiv \alpha$ and $b_1^3 = b_1^4$ and $b_2^3 = b_2^4$. Passive

material parameters were experimentally determined based on isolated rat thoracic ducts in the previous section, and those parameters are utilized in these simulations.

For active contraction, we consider an adaptation of the model of Rachev and Hayashi [111] as described in the previous section. Note that active contributions are only considered in the circumferential direction due to the preferred alignment of smooth muscle cells in the circumferential plane. Active parameters experimentally determined for rat thoracic ducts were utilized in these simulations. In order to capture the cyclic contractile feature of the lymphangion, we have here prescribed a time-varying value of the parameter as an adaptation of the prescribed motion published by Bertram et al. [159] such that,

$$T_{act} = T_{act}^{max}\left[1 - \cos\left(2\pi f(t - t_c)\right)\right] + T_{act}^{bas} \tag{4.9}$$

where f is the frequency of the lymphatic contraction, t is the current time, and t_c is the duration of the active contraction, and an additional parameter t_r is defined as the refractory period or time separating contractile phases. Note that because of the cosine function, the maximum value of T_{act} is equal to $2T_{act}^{max} + T_{act}^{bas}$, resulting in contractions stronger than expected based on experimental observations. This waveform was chosen partly based on previously proposed models. Because frequency has been shown to depend on transmural pressure [13, 262], frequency was prescribed based on the average basal transmural pressure and was defined based on equation (4.10),

$$f = m * \sqrt{p_a + \frac{p_b - p_a}{2}} + n \tag{4.10}$$

where m and n are parameters governing the shape and intercept of the curve, respectively. These values were determined by digitizing data from Figure 2C in the study from Davis et al. [13] and performing a nonlinear regression using the MATLAB

subroutine `lsqnonlin`. Results depicting the regression can be seen in Appendix B. The calculated values for m and n were 1.59 and 4.28, respectively. Note that this relationship forces a (nearly) maximum frequency value. Note also that the frequency can also be defined as the inverse of the sum of t_c and t_r, and thus alteration of the frequency requires manipulation of either the duration of contraction, the refractory time, or both. In this study, we have assumed that the duration of contraction is constant, and thus the refractory time is the value adjusted in order to calculate the correct frequency based on equation (4.10), which is in agreement with observations reported on collecting rat lymphatics *in vivo* [263, 264]. Incorporation of the strain energy density function in equation (4.6) in conjunction with this theoretical framework can then provide us with a complete view of the mechanical environment in the vessel wall.

Lumped parameter model. In order to model lymph propulsion through a lymphangion, the vessel was modeled similar to that in Bertram et al. [159] such that the vessel can be considered a cylindrical, distensible tube with a valve at the proximal and distal end of the tube and fixed inlet and outlet pressures p_a and p_b, respectively. Pressure within the vessel is divided into three nodes: p_1, p_m, and p_2 which are the pressures immediately distal to the inlet valve, the luminal pressure halfway down the length of the vessel, and the pressure immediately proximal to the outlet valve, respectively. A graphical representation of the model of a lymphangion can be seen in Figure 4.8.

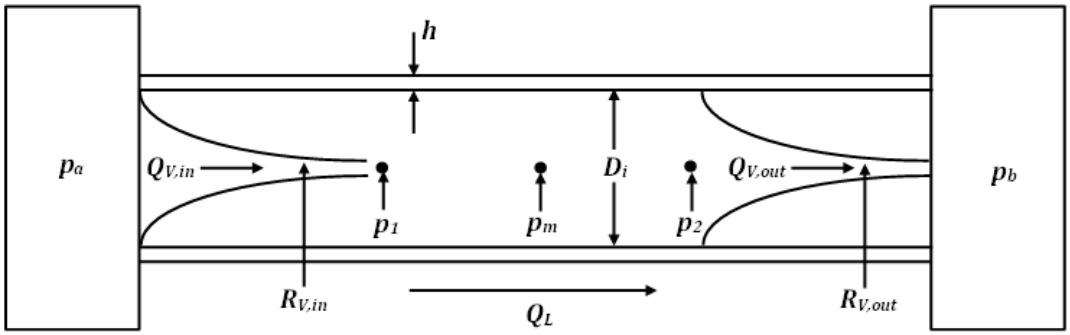

Figure 4.8. Model of the relationship between pressure, flow, and diameter in a single lymphangion pump. The time varying values include the diameter D, the pressures p_m, p_1, p_2, and the flow rates Q_1, Q_2. The valve resistances R_{V1} and R_{V2} are functions of the pressure drop (the difference between the inlet and the outlet pressure). The external pressure as well as each of the pressure reservoirs are fixed values, and p_a is constitutively less than p_b.

Lymph propulsion through the tube was modeled as steady, fully-developed, unidirectional, axisymmetric flow such that the pressure drop across the length of the tube can be defined by equation (4.11),

$$\Delta P = \frac{8\mu\lambda_z L Q_L}{\pi r_i^4} \tag{4.11}$$

where ΔP is the pressure drop across the length of the vessel, μ is the dynamic viscosity of the fluid, λ_z is the axial stretch of the vessel, L is the unloaded length of the vessel, Q_L is the flow through the vessel, and r_i is the inner radius of the vessel. The assumption of Poiseuille flow from equation (4.11) has been demonstrated to be a reasonable approximation of the flow profile in areas away from the valves [154, 155]. If contraction of the vessel is assumed to be uniform throughout the vessel wall and the fluid is considered incompressible, bulk flow through the vessel can be defined as the change in volume per unit of time as seen in equation (4.12),

$$Q_L = \frac{\partial V}{\partial t} = 2\pi r_i \frac{\partial r_i}{\partial t} \lambda_z L \tag{4.12}$$

For the sake of simplicity, we assume here that the pressure drop across the vessel is linear such that the pressures p_1 and p_2 can be approximated by equation (4.13).

$$p_1 = p_m + \frac{\Delta P}{2}, \quad p_2 = p_m - \frac{\Delta P}{2} \tag{4.13}$$

In this model, the transmural pressure p_m is calculated from the constitutive model previously described using the time-dependent T_{act} term in equation (4.9) and Laplace's Law following equations (4.4) and (4.5). Taken together, we can calculate the entire pressure profile of a single lymphangion. Using these pressures, the flow across the inlet and outlet valves can then be calculated using equation (4.14),

$$Q_V = \frac{p_{in} - p_{out}}{R_V} \tag{4.14}$$

where p_{in} is the pressure on the proximal side of the valve, p_{out} is the pressure on the distal side of the valve, and R_V is the resistance of the valve as defined by equation (4.15),

$$R_V = R_{Vn} + \frac{R_{Vx}}{1 + exp\big(-s_o(\Delta p_V - \Delta p_o)\big)} \tag{4.15}$$

where R_{Vn} is the resistance when the valve is fully open, R_{Vx} is the resistance when the valve is fully closed, s_o is the valve opening slope, Δp_V is the pressure drop across the valve (defined as $p_{in} - p_{out}$), and Δp_o is the pressure drop at which the valve opens and closes. It has been shown that this value is a function of transmural pressure and differs depending on whether the valve is opening or closing [126]. For simplicity's sake, we have modeled the transition state as a fixed value of pressure differential for both opening and closing characteristics. Finally, conservation of mass dictates that

$$dV_L = dV_{V,in} - dV_{V,out} \tag{4.16}$$

where dV_L is the change in volume in the lumen of the vessel for a fixed time step, dt, $dV_{V,in}$ is the volume of fluid taken in through the proximal valve for a fixed time step, and $dV_{V,out}$ is the volume of fluid expelled through the distal valve for a fixed time step. For modeling, the time-dependent active contraction was prescribed following equation (4.9) and the midwall radius was calculated at each time step by utilizing Equation (4.16) as the cost function and employing the MATLAB subroutine `lsqnonlin`. Following calculation of the inner radius, all other values can be calculated explicitly prior to moving forward to the next time step.

Various flow parameters have been previously utilized to quantify changes in lymphatic function. These metrics can be defined by the following equations:

$$EF = (EDD^2 - ESD^2)/EDD^2 \tag{4.17}$$

$$FPF = EF \times f \tag{4.18}$$

$$AMP = EDD - ESD \tag{4.19}$$

$$SV = EDV - ESV \tag{4.20}$$

where EF is the ejection fraction, FPF is the fractional pump flow, EDD is the end diastolic diameter, ESD is the end systolic diameter, f is the contractile pumping frequency, AMP is the contraction amplitude, SV is the stroke volume, EDV is the end diastolic volume, and ESV is the end systolic volume where the volume at any point in time is calculated as $V = \pi r_i^2 \lambda_z L$.

Time-dependent volumetric growth. The constitutive model describing the solid mechanical behavior of the vessel wall can be extended to include volumetric growth following the model proposed previously by Taber et al. [117]. To expand the model to support growth, the deformation gradient $\boldsymbol{F}$ must be reformulated to include a growth

term. To do so, an infinitesimally small element of an unloaded and stress-free body (in this case, the vessel wall) must first undergo growth before undergoing kinematic deformation such that the deformation gradient can be defined as $\boldsymbol{F} = \boldsymbol{F}^* \cdot \boldsymbol{F}_g$ where $\boldsymbol{F}^*$ is the kinematic deformation gradient tensor describing the deformation from an unloaded, grown state to a loaded grown state (i.e. the current state), and $\boldsymbol{F}_g$ is the growth deformation gradient describing the deformation from the original unloaded state to the current or grown unloaded state. With this framework in place, the in-plane stretch ratios can then be described by equations (4.21) - (4.23),

$$\lambda_r = \lambda_r^* \lambda_{gr} = h/H_0 \tag{4.21}$$

$$\lambda_\theta = \lambda_\theta^* \lambda_{g\theta} = r/R_0 \tag{4.22}$$

$$\lambda_z = \lambda_z^* \lambda_{gz} = l/L \tag{4.23}$$

where λ_i^* is the ratio of the current loaded length to the current unloaded length and λ_{gi} is the ratio of the current unloaded length to the original unloaded length, H_0 and R_0 are the unloaded thickness and midwall radius prior to growth, respectively, and $i = (r, \theta, z)$. To accurately describe the growth behavior of the tissue with this framework, a growth law must be prescribed for each plane. However, data motivating lymphatic growth is largely absent in the literature. Consequently, growth laws are prescribed here to model the growth observed in arteries. Sustained increases in flow are known to induce an increase in radius with little change in thickness [265], whereas sustained increases in luminal pressure are known to induce an increase in thickness with little change in radius. It is widely believed that these changes occur in an effort for the tissues to reach homeostatic states of stress. Changes in the growth ratios λ_{gi} can be defined according to the following equations,

$$d\lambda_{gr} = \frac{1}{\eta_r}\left[\frac{T_{\theta\theta} - T_{\theta\theta,m}}{T_{\theta\theta,m}}\right] * dt_g \tag{4.24}$$

$$d\lambda_{g\theta} = \left\{\frac{1}{\eta_\theta}\left[\frac{T_{\theta\theta} - T_{\theta\theta,m}}{T_{\theta\theta,m}}\right] + \frac{1}{\eta_\tau}\left[\frac{\tau - \tau_m}{\tau_m}\right]\right\} * dt_g \tag{4.25}$$

$$d\lambda_{gz} = 0 \tag{4.26}$$

where $T_{\theta\theta,m}$ is the homeostatic circumferential stress, τ is the luminal shear stress, τ_m is the homeostatic shear stress, and η_r and η_θ are the time constants governing the speed of growth in the radial and circumferential directions due to sustained changes in circumferential stress, respectively, η_τ is the time constant governing growth in the circumferential direction due to sustained changes in shear stress, and dt_g is the fixed change in time during growth. Note that $d\lambda_{gz}$ is prescribed as zero for this study because growth in the axial direction is neglected. In this case the wall shear stress is defined by equation (4.27),

$$\tau = \frac{4\mu Q}{\pi r_i^3} \tag{4.27}$$

where μ is the dynamic viscosity, Q is the volumetric flow rate for a fixed change in time as calculated by equation (4.12), and r_i is the inner radius.

In order to properly predict growth and remodeling behavior, it is necessary to accurately assign time constants and homeostatic stress values that govern the growth behavior. In vascular function, circumferential stress can be calculated simply from the tonic contraction of smooth muscle cells in response to blood flow or increased blood pressure; however, the lymphatic vasculature experiences more variable circumferential and shear stress due to the spontaneous and rhythmic contraction of the muscle cells. Given this and the lack of experimental data motivating the concept of lymphatic growth

and remodeling, time-averaged stress values are considered here such that growth is calculated from equations (4.24) - (4.26) using the average stresses experienced over the course of a single contraction of a lymphangion, and the equilibrium values are assigned as the average stress values calculated prior to applying a step change to the system.

4.3.2 Illustrative simulations

Material parameters. Active and passive mechanical properties of isolated rat thoracic ducts were quantified in Milestone 1, and the estimated values are used here to govern the mechanical behavior during simulation. A list of constants used during all simulations can be seen in Table 4.4.

Simulation 1 – Changes in short term lymphatic pumping function in response to elevated afterload. Let all growth terms equal ∞ such that no growth occurs in response to a change in the mechanical environment. Let the preload equal 3 cmH_2O, and let the afterload experience a gradual, linear increase from 4 to 16 cmH_2O. Time-dependent pumping behavior including radius, flow rate, and transmural pressure can be seen in Figure 4.9 for time points before and after an increase in afterload. Pumping metrics can be seen in Figure 4.10. Note that ejection fraction decreases following an increase in afterload, while ESD increases, inducing a decrease in contractile amplitude, in response to elevated afterload. Note that the EDD does not change in this case because pumping pressure was assumed to be equal to the inlet pressure, which remains unchanged. Functional pumping metrics follow a pattern that is similar to that observed in Figure 2 of Davis et al., thus providing validity to the predictive capability of the model.

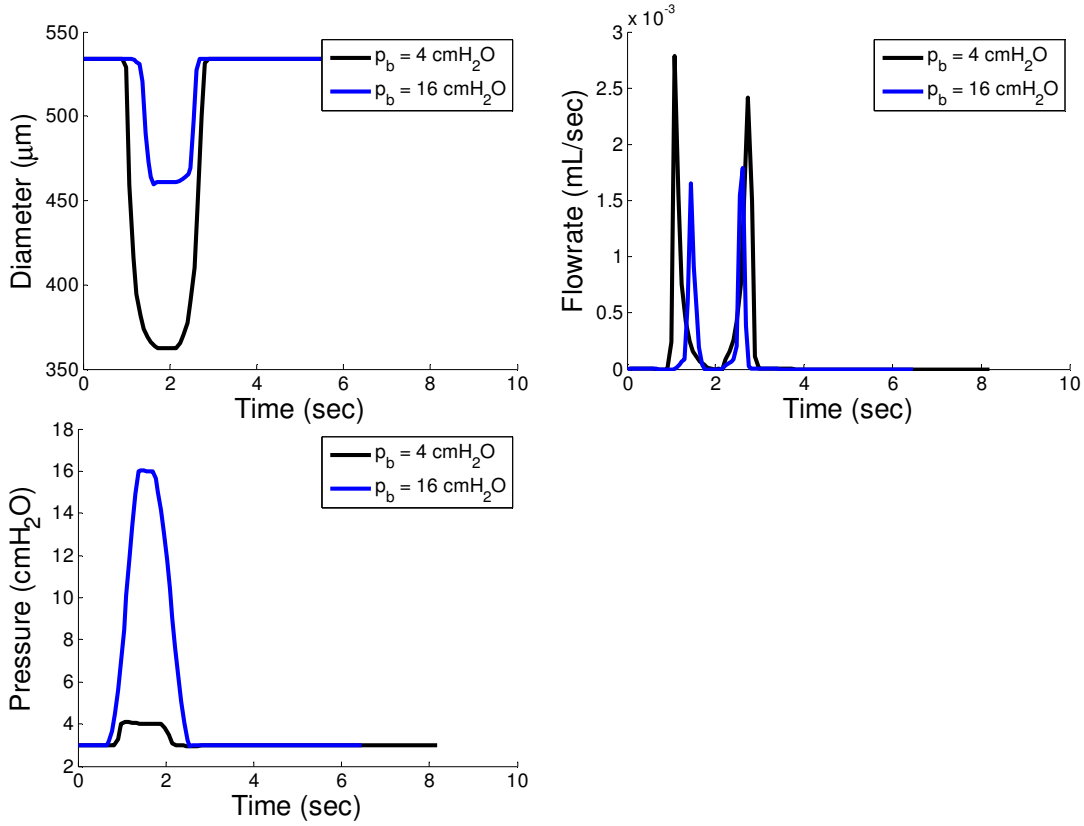

Figure 4.9. Predicted time-dependent waveforms of a single pumping lymphangion under two different afterloads. (Top left) Outer radius measurements over the course of a single pumping cycle. Note that EDD does not change, but ESD increases following an increase in afterload, thus decreasing the contractile amplitude. (Top right) Flow rates are decreased over the course of a single pumping cycle following an increase in afterload. (Bottom left) Pressure waveforms range from the value of the preload (unchanging in this simulation) to the value of the afterload.

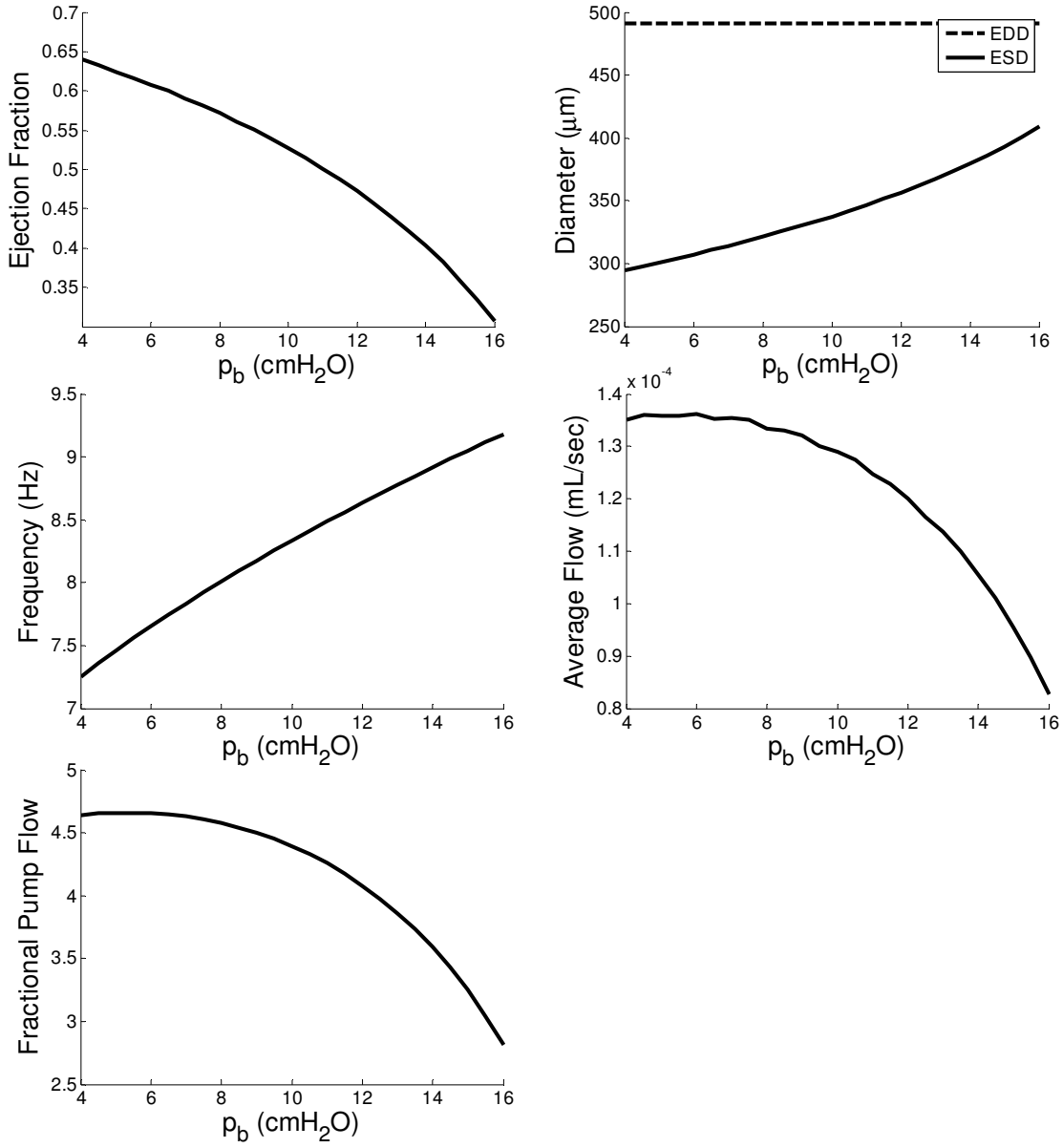

Figure 4.10. Functional flow metrics for a single pumping lymphangion as a function of increasing afterload. (Top left) Ejection fraction decreases uniformly as afterload increases. (Top right) EDD is unchanging, and ESD increases, thus decreasing contractile amplitude as a function of increasing afterload. (Middle left) Contractile frequency increases with increasing afterload. (Middle right) Average flow rate initially increases and subsequently decreases as afterload increases. (Bottom left) Fractional pump flow increases initially and subsequently decreases as afterload increases. Note that although ejection fraction decreases uniformly, FPF has an apparent maximum because of the increasing frequency.

Table 4.4. Table of constants used for simulations illustrating the effects of various changes in mechanical loading on growth and remodeling behavior of a single lymphatic vessel. Simulations were performed using data obtained from a passive biaxial mechanical test of a rat thoracic duct.

Constant	Units	Simulation 1	Simulation 2	Simulation 3
R_0	cm	240	240	240
H_0	cm	32.2	32.2	32.2
b	dyne/cm^2	110.3	110.3	110.3
b_1^1	dyne/cm^2	6849.6	6849.6	6849.6
b_2^1	dyne/cm^2	2.9362	2.9362	2.9362
b_1^2	dyne/cm^2	38359.3	38359.3	38359.3
b_2^2	dyne/cm^2	3.417	3.417	3.417
b_1^3	dyne/cm^2	2077.8	2077.8	2077.8
b_2^3	dyne/cm^2	4.1736	4.1736	4.1736
α^1	degrees	90	90	90
α^2	degrees	0	0	0
α^3	degrees	31.1	31.1	31.1
$T_{act,max}$	dyne/cm^2	103409	103409	103409
a	unitless	9.9115	9.9115	9.9115
int	dyne/cm^2	168.02	168.02	168.02
λ_M	unitless	1.5718	1.5718	1.5718
λ_0	unitless	0.6805	0.6805	0.6805
λ_z	unitless	1.3	1.3	1.3
RV_x	dyne·s/(cm^2·mL)	12 (10^7)	12 (10^7)	12 (10^7)
RV_n	dyne·s/(cm^2·mL)	600	600	600
s_o	cm^2/dyne	0.2	0.2	0.2
p_e	cmH$_2$O	0	0	0
p_a	cmH$_2$O	3	3	3
p_b	cmH$_2$O	**4-16**	**4,16**	**4,16**
p_o	cmH$_2$O	-0.25	-0.25	-0.25
μ	cP	0.01	0.01	0.01
L	cm	0.3573	0.3573	0.3573
t_c	s	2	2	2
η_r	days	**∞**	**5**	**5**
η_θ	days	**∞**	**∞**	**60**
η_τ	days	**∞**	**∞**	**5**

Simulation 2 – Radial growth in response to elevated afterload. Let the afterload p_b experience a sustained increase from 4 to 16 cmH$_2$O, let the time constant η_r equal 5 days, and let the time constants η_θ and η_τ equal ∞ such that growth occurs only in the radial direction. The "target" value of circumferential stress was here defined as the circumferential stress calculated prior to the step increase in afterload. Simulation results

suggest that the pressure profile is relatively unchanged, but EDD and ESD both decrease as the thickness increases in order to restore the circumferential stress to the target value, resulting in a decrease in bulk flow (Figure 4.11). Circumferential stress is restored to the homeostatic value with an increase of wall thickness of approximately 24% (40 μm compared to 32.2 μm), but note that shear stress is decreased and does not return to homeostatic values as growth in this simulation is not shear-dependent (Figure 4.12). Ejection fraction is initially decreased following a step increase in afterload (Figure 4.13). However, the value increases slightly as the vessel wall thickens, but the value remains significantly less than the original homeostatic value. Note that fractional pump flow follows the same pattern, and, despite the sustained increase in contractile frequency, also never returns to original homeostatic values.

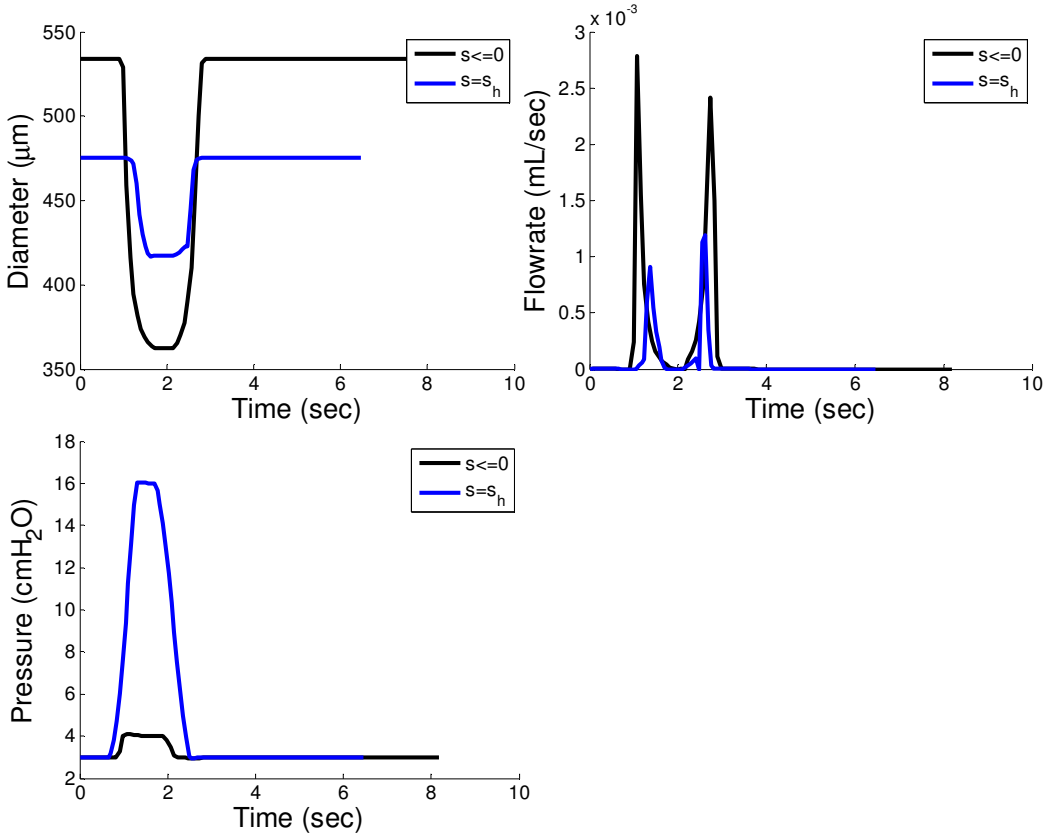

Figure 4.11. Time-dependent waveforms of a single pumping lymphangion under initial homeostatic conditions and homeostatic conditions following mechanically-induced vessel wall thickening. (Top left) EDD decreases and ESD increases due wall thickening following an increase in afterload. (Top right) Flow rates after reaching mechanical homeostasis are decreased. (Bottom left). Pressure profiles follow the preload and the afterload and appear relatively unaffected by the evolution of the thickness of the vessel wall.

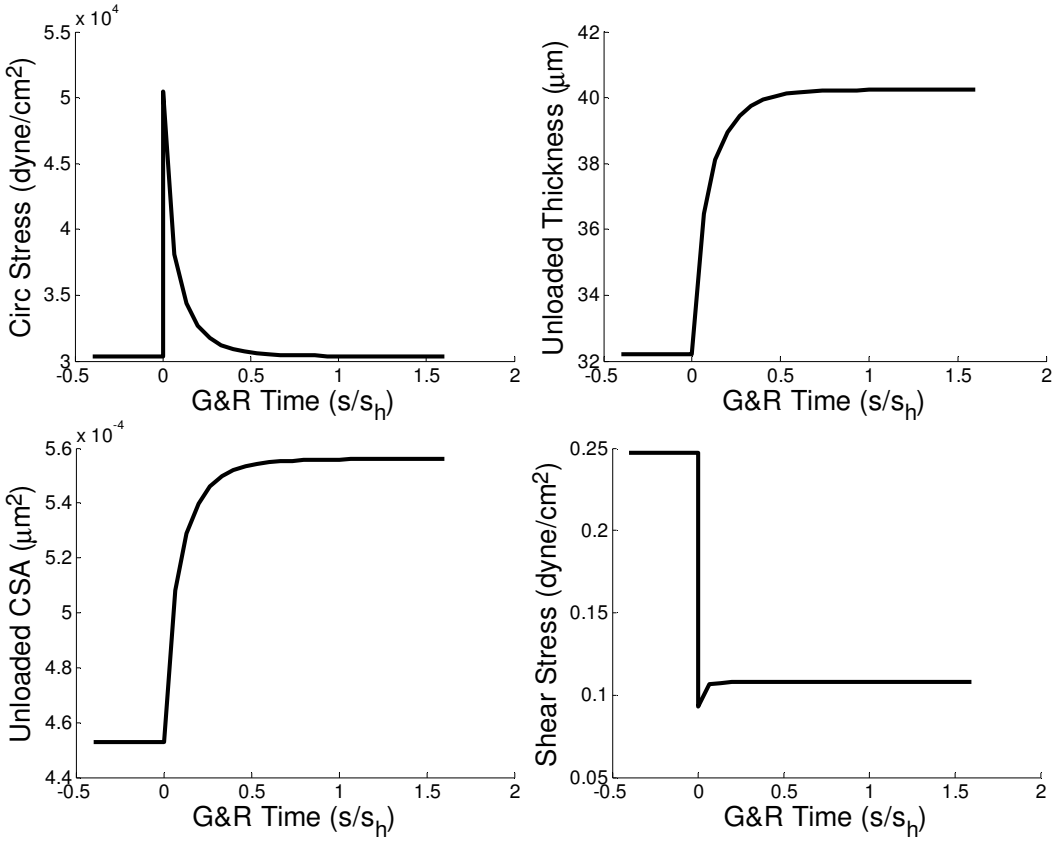

Figure 4.12. Mechanically-mediated radial geometric evolution of a single pumping lymphangion in response to a sustained elevation in afterload. (Top left) Circumferential stress is initially elevated following an increase in afterload and subsequently approaches the target value as the vessel wall thickens. (Top right) The vessel wall thickens in response to a sustained elevation in afterload in order to restore circumferential stress. (Bottom left) Vessel cross-sectional area increases as thickness increases. Increases in cross-sectional area have been reported in lymphatic vessels from lymphedematous legs of human subjects in the literature. (Bottom right) Shear stress is initially reduced but undergoes a small increase as the vessel wall thickens.

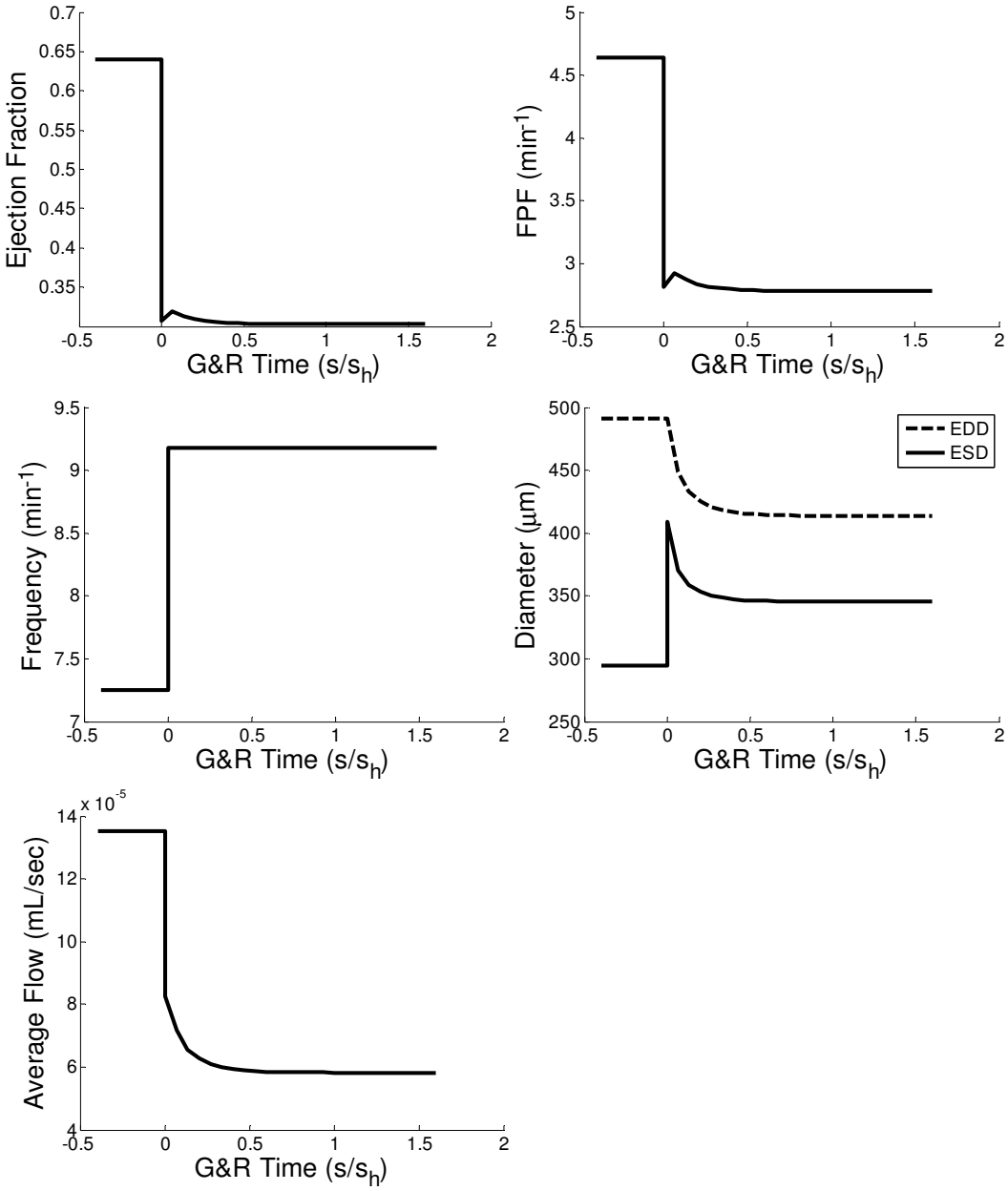

Figure 4.13. Evolution of functional flow metrics following a sustained increase in afterload and subsequent radial growth of a vessel wall. (Top left) Ejection fraction decreases significantly following an increase in afterload and undergoes little change in response to radial growth. (Top right) FPF follows the same trend as ejection fraction despite a sustained increase in frequency. (Middle left) Contractile frequency increases following an increase in afterload. Note that frequency is not dependent on the unloaded geometry and therefore does not evolve with growth. (Middle right) EDD and ESD decrease with radial growth, but EDD is reduced compared to initial homeostatic values, whereas ESD is elevated compared to initial homeostatic values. (Bottom left) Average flow rate per contraction experiences an initial decrease due to increased afterload as well as further decrease following vessel remodeling.

Simulation 3 – Radial and circumferential growth in response to elevated afterload. Let the afterload p_b experience a sustained increase from 4 to 16 cmH_2O, let the time constant η_r equal 5 days, and let the time constants η_θ and η_τ equal 60 days and 5 days, respectively such that growth occurs in the radial direction (i.e. thickness changes) in response to circumferential stress and growth occurs in the circumferential direction (i.e. radius changes) in response to circumferential and shear stress. Time-dependent waveforms show a dramatic decrease in EDD, ESD, and contractile amplitude as compared to the homeostatic value prior to the increase in afterload (Figure 4.14). Bulk flow was decreased and the pressure waveforms were unchanged following geometric changes of the vessel. Circumferential stress was initially increased due to elevated afterload but experienced a sharp decrease as the vessel remodeled in response to the dominant shear term (Figure 4.15). Shear stress initially experienced a sharp drop and gradually increased as the vessel radius decreased. Vessel thickness and radius decreased by 25% and 33%, respectively. Note that without the inclusion of shear-induced remodeling, thickness increases in order to re-establish a homeostatic value of circumferential stress, but inclusion of shear dominates the growth behavior and causes a sharp decrease in radius. Ejection fraction and fractional pump flow were both reduced in response to elevated afterload, and geometric remodeling induced a small increase in both values, but neither value reached the values associated with the original homeostatic configuration (Figure 4.16).

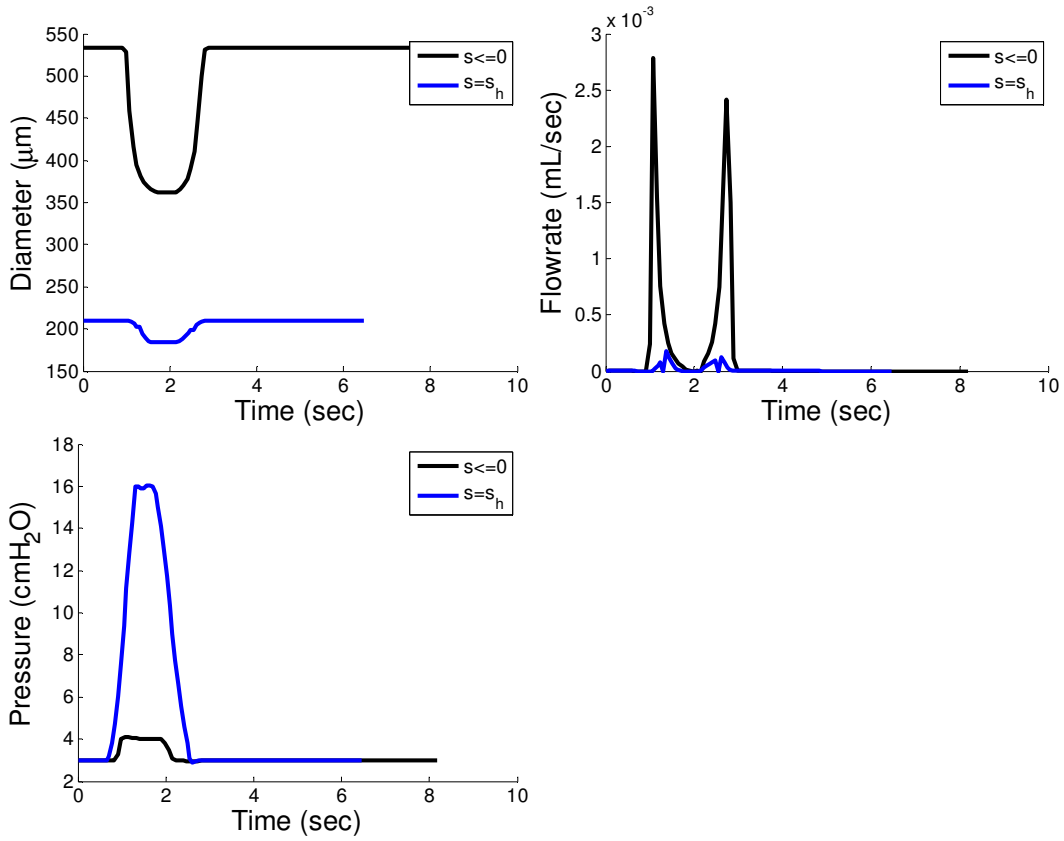

Figure 4.14. Time-dependent waveforms of a single pumping lymphangion following mechanically-mediated radial and circumferential growth. (Top left) EDD, ESD, and contractile amplitude are substantially reduced following growth induced by increased afterload. (Top right) Bulk flow is reduced following remodeling. (Bottom left) Pressure profiles are unchanged both before and after elevation in afterload.

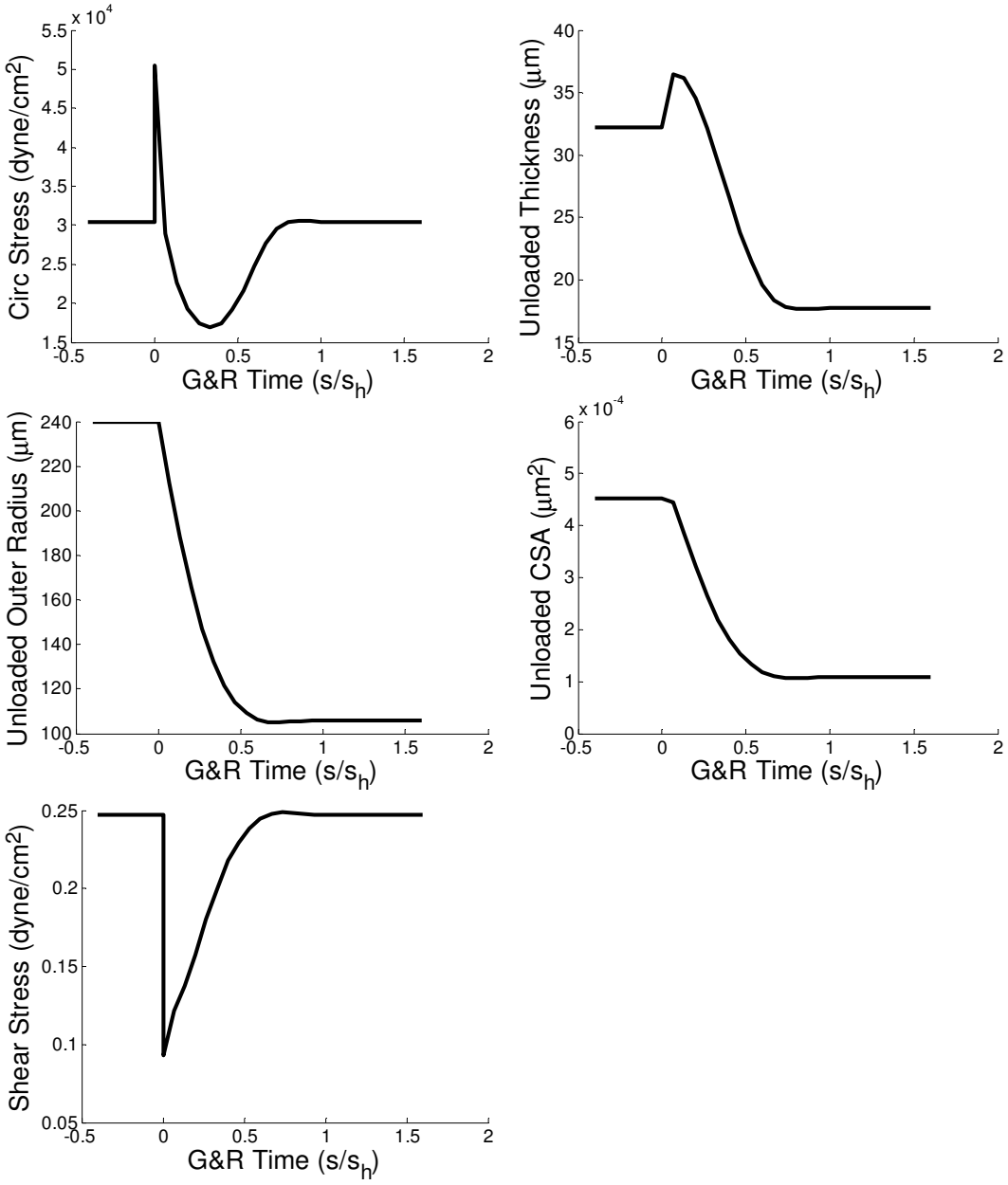

Figure 4.15. Mechanically-mediated circumferential and radial growth of a single lymphangion in response to elevated afterload. (Top left) Circumferential stress undergoes an initial increase in response to the elevated load, but a subsequent decrease occurs as the shear stress term dominates the geometric changes of the vessel. (Top right) The vessel initial thickens but ultimately atrophies in response to elevated afterload. (Middle left) The vessel radius reduces in order to restore values of time-averaged shear stress. (Middle right) Vessel cross-sectional area decreases following remodeling. (Bottom left) Time-averaged shear stress restores to the initial homeostatic value following vessel atrophy.

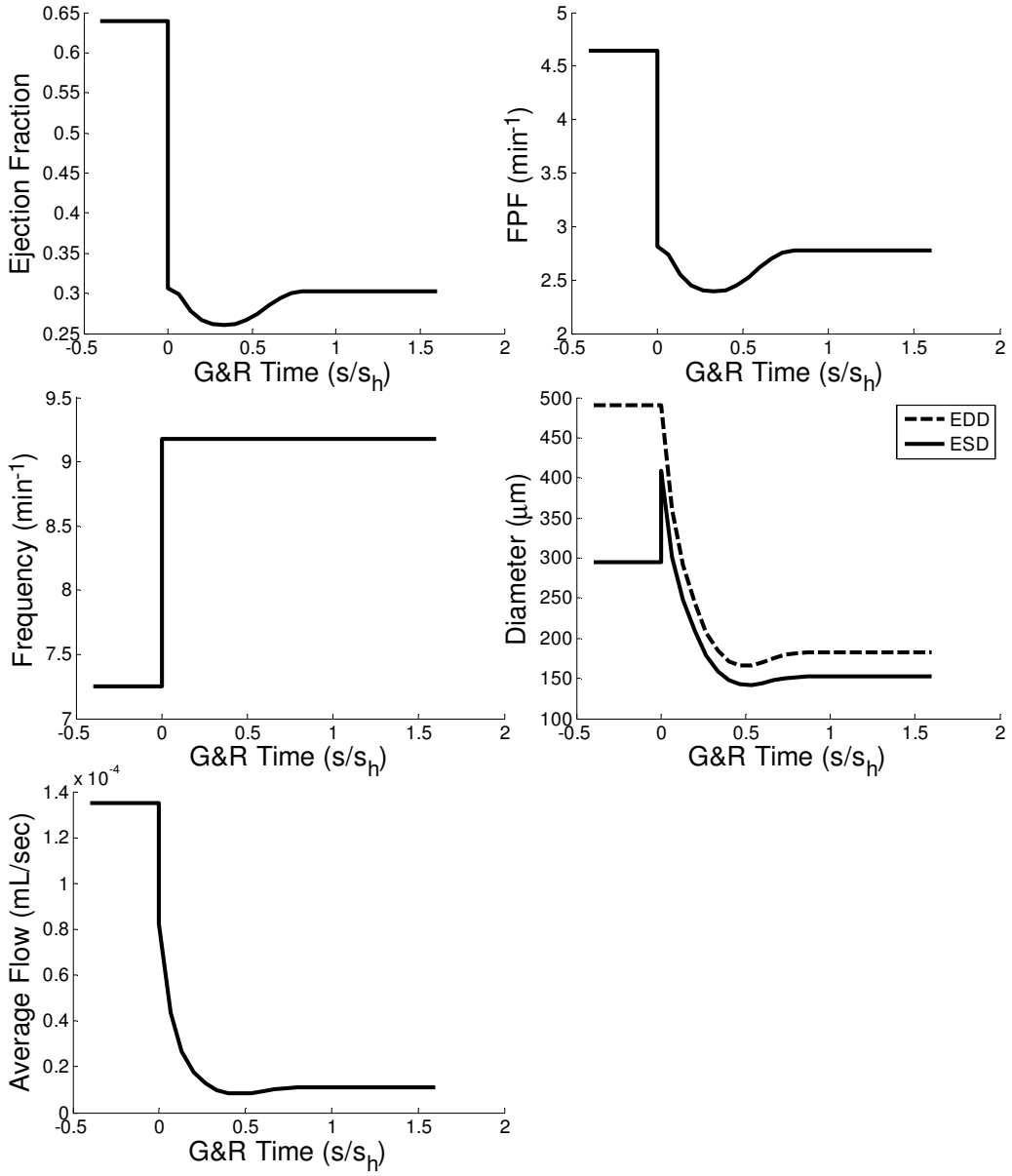

Figure 4.16. Evolution of functional flow metrics following a sustained increase in afterload and subsequent circumferential and radial growth of a vessel wall. (Top left) Ejection fraction is initially reduced but is slightly increased in response to reduction of vessel thickness and radius. (Top right) Fractional pump flow follows the same pattern as the ejection fraction. (Middle left) Contractile frequency is increased in response to elevated afterload. (Middle right) EDD and ESD are both reduced compared to initial homeostatic values. (Bottom left) Average flow rate per contractile cycle decreases in response to vessel remodeling.

4.3.3 Discussion

Mechanically-mediated maladaptive growth and remodeling as it relates to disease development is a well-documented phenomenon, especially in the vascular mechanics literature; however, little is known regarding the relationship between the mechanical environment of lymphatic vessels and the progression of lymphedema. Consequently, the primary goals of this milestone were twofold: (1) to test the hypothesis that mechanics is a driver of the progression of lymphedema using a theoretical framework for mechanically-mediated volumetric growth, and (2) to highlight key parameters that can potentially be investigated as these motivators using available ex vivo testing techniques. We have here developed a microstructurally-motivated lumped parameter model that predicts diameter, pressure, and flow profiles for a single lymphangion that follows patterns seen in the literature [13] and utilized this model to predict long-term growth and remodeling in response to a sustained elevation of afterload under various growth considerations. These simulations suggest that radial growth can restore circumferential stress but that shear-induced remodeling leads to reduction of vessel radius and thickness in response to a sustained elevation in afterload. Such a finding suggests that shear stress may not be a mediator of the lymphatic growth observed in the lymphedema literature.

Results from simulation 1 demonstrate the ability of our model to recapitulate available data in the literature, specifically that from Davis et al. These simulations were performed for a thoracic duct (as opposed to mesenteric lymphatics), and thus the geometric predictions were much larger than those observed in the aforementioned study. However, functional pumping metrics (e.g. ejection fraction, fractional pumping flow) as

well as general contractile behavior (e.g. changes in EDD and ESD) in response to an elevated afterload were similar to those observed by Davis et al., thus lending credibility to the predictive capability of our model. It should be noted, however, that the peak value of the active parameter was larger than that determined in the previous study of this aim due to the chosen cosine waveform. This waveform was selected based on studies from Bertram et al. [159]. Scaling of the waveform was performed to more accurately recapitulate the results in this aim and resulted in pumping function that could not exceed normal values of afterload. This is perhaps a limitation of the solving techniques rather than the model itself, and additional work to address this limitation is ongoing. Simulations 2 and 3 suggest that thickening of the vessel wall may be exclusively due to the need for restoration of circumferential stress. Inclusion of shear-dependent growth suggests shrinking of the vessel in response to elevated afterload in order to increase the shear stress. This simulation does not follow the limited results that are reported in the literature that show narrowing of the lumen and thickening of the vessel wall. Time constants in all simulations were chosen based on the study from Taber et al. [117]; however, these time constants were prescribed for the case of aortic growth and could therefore take on any number of values for the lymphatic vasculature. Larger time constants suggest slower growth; consequently, the smaller time constant associated with shear-induced growth in simulation 3 dominated the growth process. Note that the time constants do not affect the homeostatic values of the unloaded geometry but rather how quickly the vessels remodel to achieve such homeostasis (data no shown). Thus, varying these parameters would have little effect on the ability of the model to recapitulate

geometric data in the literature, and because time-dependent remodeling data has never been reported, a sensitivity analysis of the time constants was not performed.

We assumed a target value of circumferential and shear stress for all simulations in this study based simply on the starting conditions of the vessel prior to the increase in afterload. To effectively test a hypothesis for mechanically-mediated growth and remodeling, it is critical that the hypothesis include a target value of stress for which the vessel to try to achieve. Homeostatic stress values in arteries have been proposed in previous studies [119]. These homeostatic values are on the order of 10^6 dyne/cm^2 for circumferential and axial stress and 10^1 dyne/cm^2 for shear stress; however, the stresses experienced by lymphatic vessels are notably lower than those in arteries and veins [146, 154, 266]. Indeed, homeostatic circumferential stress values in this model were 3000 dyne/cm^2, and homeostatic shear stress values were 0.25 dyne/cm^2. Future studies should investigate the homeostatic mechanical conditions of lymphatic vessels. Taken together, these results demonstrate a clear need for additional experimental data in the literature in order to better understand the role of mechanics in lymphatic remodeling and progression of lymphedema.

Although these simulations suggest a novel perspective, they should be interpreted with caution due to the large number of assumptions that must be made. First, the transport model contains many assumptions that may not in fact be true of normal *in vivo* lymphatics. To start, the model does not include the effects of gravity on overall lymph transport, thus limiting its application in studying lymphedema of the lower limbs in humans. With this assumption in mind, the model still adequately supports *ex vivo* testing of lymphatics as well as *in vivo* experimental models of lymphedema such as a

mouse tail model that does not require inclusion of gravity in its considerations [267]. As additional experimental data becomes available, expansion of the model can be performed in order to include the effects of gravity and better simulate the native environment of lymphatics of the lower limbs in humans.

Valve behavior in lymphatics is known to be complex and has recently been quantified as a function of transmural pressure [159]. Transition properties of the valves are dependent on the pressure drop across the valves, and lymphatic valves have different properties depending on whether they are opening or closing. In most cases the valves are biased to remain in an open position (i.e. the valves remain open even when facing a small negative pressure drop) [126]. Valve behavior here was simplified to support valve opening properties that were constant rather than pressure-dependent in order to simplify model behavior. Constants were chosen to support the concept that valves should remain biased to stay open. Valve behavior is an important determinant in flow profiles within the vessel; however, the goal of this milestone was to develop a framework in which specific parameters could be identified as contributors to lymphatic dysfunction, and thus valve behavior was simplified with the assumption that future studies might include a more detailed analysis of the relationship between complex valve behavior and mechanically-mediated growth and remodeling. Additional assumptions of the transport model include a linear pressure drop across the vessel and Poiseuille flow, and although these may not represent exact behavior, it is unlikely that these assumptions would dramatically inhibit the utility of the model due to the low Reynold's numbers generally observed in lymphatic flow (less than 1) [154].

Many assumptions were made in order to predict growth and remodeling behavior. First, a volumetric growth model explicitly ignores the remodeling behavior of individual constituents of the microstructure (e.g. collagen and elastin). Growth and remodeling of arteries is a much larger field, and many have proposed constrained mixture models that propose differential growth behavior of individual constituents [118, 120-122]. Lack of available data regarding microstructural organization and evolution of lymphatics makes such models too advanced. The volumetric model proposed here is similar to that proposed by Taber et al. [117], but other volumetric models have been proposed for arteries that have offered a wide range of utility in understanding cardiovascular disease development [116, 268-270]. Without a thorough understanding of stress-dependent microstructural behavior of lymphatics, a volumetric growth model is a suitable starting point in understanding mechanically-mediated disease development.

Due to the spontaneous and rhythmic contraction of lymphatic vessels, the mechanical environment is significantly more complex than that seen in arteries that exhibit only tonic contraction. Consequently, growth behavior was assumed to depend on time-averaged values of stress that occur over the course of a single contraction cycle of a vessel. This consequently makes growth and remodeling behavior dependent on the frequency of contraction. In this case, duration of contraction was assumed to be constant, whereas frequency (as determined by the addition of the duration of contraction and refractory period) was calculated as a function of the spatially averaged transmural pressure (i.e. the average of the afterload and preload). The relationship between the frequency and transmural pressure was determined from values in the literature; however, the data in the literature is noisy, and thus the model is very inaccurate. Fractional pump

flow is explicitly dependent on the contractile frequency, and in order to accurately calculate such a metric, the relationship between frequency and transmural pressure should be better characterized. It should be noted that Gasheva et al. have demonstrated that shear-dependent production of nitric oxide from spontaneous contractions contributes to the maintenance of contractile frequency in rat thoracic ducts [124], but it is unknown how the geometry of vessel contributes to this behavior.

Mihara et al. have reported thickening of lymphatic vessels in patients with lymphedema, and although they report increased pressures associated with thickening, pressure values are not reported, and neither are geometric changes quantified [16]. Similar results have been shown by another group that demonstrate phenotypic changes of muscle cells as well as changes in cross-sectional area of lymphatics in progression of lymphedema [271], but this study also lacks pressure measurements in order to correlate mechanical load with geometric evolution. Phenotypic changes of muscle cells may be associated with decreased contractility. These simulations do not incorporate any changes in the material parameters governing the contractility of the vessel (e.g. T_{act}^{max} and T_{act}^{bas}) and therefore assume a constant maximum value of contractility and basal tone. However, proliferation and phenotypic changes of muscle cells would likely inhibit contractility and consequently the time-dependent flow profiles of the vessel. Such a relationship should be experimentally investigated and included in future simulations.

These simulations predict growth and remodeling behavior in the face of a constant adverse pressure gradient. There have been a multitude of other experimental and computational studies that have investigated the behavior of lymphatics under varying axial pressure gradients. Notably, Quick et al. developed a computational model

similar to the one proposed here and applied it to simulations of a favorable pressure gradient [152]. The simulations presented here make no account for conduit behavior of lymphatic vessels, an assumption considered valid only for cases of an adverse pressure gradient. Additionally, the experimentally determined material parameters used in the proposed model were evaluated for a single lymphangion with an axial pressure gradient of 0 cmH_2O. While material parameters that govern passive mechanical behavior and maximum contractility should generally remain constant independent of load, strong correlations between loading conditions and parameters such as contractile frequency have been repeatedly demonstrated in many studies.

The mechanical environment of a single lymphangion is difficult enough to quantify; however, the model should ideally be expanded to support the prediction of flow through a chain of lymphangions as this is more physiologically relevant. Adding vessels onto a chain creates additional complication in prediction of behavior because timing and magnitude of contractions affect the pressure profiles within each respective segment of the chain and consequently affect valve behavior and bulk flow. Expansion of the model to support a chain would not only create difficulties in the mathematical modeling but would also require additional information of the mechanical properties of the tissue at locations of valve insertion. The current model treats valve locations as two-dimensional planes with built in variable resistance, an assumption that obscures the nuances of mechanical behavior in a single vessel, but mechanical behavior at valve insertion may induce more pronounced changes in the transport capability of a long chain of vessels.

Model limitations aside, this study provides a novel framework for the investigation of mechanically-mediated lymphatic growth and remodeling. The transport model (excepting growth) accurately recapitulates experimental data available in the literature investigating the effects of changes in the mechanical environment on lymphatic function. The successful development of the transport model provided a platform for the incorporation of mechanically-mediated growth and remodeling behavior in an actively pumping lymphangion. Our simulations suggest that a sustained elevation in afterload induces geometric changes in an isolated lymphatic vessel that is associated with decreases in standard markers of lymphatic function (e.g. ejection fraction). This model offers a novel perspective on potential parameters driving the progression of lymphatic dysfunction and the progression of lymphedema and directly motivates future studies to investigate lymphatic growth and remodeling.

CHAPTER 5

CONCLUSIONS AND FUTURE DIRECTIONS

5.1 Summary

The overall purpose of this study was to utilize various modeling techniques in biomechanics to test hypotheses that would identify key parameters in mechanically-mediated disease development in the context of understudied populations. Two separate modeling techniques were employed to study two different diseases of the vasculature. First, a common mouse model of atherosclerosis was used to test the hypothesis that EFV treatment leads to arterial stiffening, a hypothesis motivated by clinical studies that established a correlation between EFV treatment and vascular remodeling and dysfunction in an Ethiopian population of HIV-1+ adults. Second, a microstructurally-motivated mathematical model of lymphatic mechanical behavior was developed in the context of finite elasticity to test the hypothesis that changes in the mechanical environment of the lymphatic vasculature lead to mechanically-mediated growth and remodeling.

Cross-sectional clinical studies were performed in adult and pediatric Ethiopian HIV-1+ patients in order to investigate the role of various antiretroviral drugs in the progression of preclinical markers of CVD. PWA and PWV were analyzed in all patients in order to quantify arterial stiffening in the aorta. Non-invasive ultrasound was implemented to quantify arterial stiffening and geometric changes in the carotid artery as well as flow-mediated dilation of the brachial artery. EFV treatment was associated with various markers of CVD in the adult population, most notably an increase in arterial

stiffness as measured by PWV in EFV-treated subjects compared to NVP-treated subjects and impaired FMD in EFV-treated subjects compared to NVP-treated and HAART-naïve subjects. Given the significant HIV burden in sub-Saharan Africa, the prevalence with which EFV is prescribed, and the lack of data investigating HIV-related CVD in Ethiopian populations, this study offered useful information that motivated the need to better characterize the role of EFV in the development of CVD. Consequently, we employed a mouse model of atherosclerosis to study the effects of EFV on vascular remodeling independent of HIV infection and the drug cocktails associated with treatment. Mice were treated with EFV for 35 or 70 days. Biaxial mechanical testing was performed on suprarenal abdominal aortas following 35 days of treatment, and early onset of plaque progression was also quantified for both 35 and 70 days of treatment. This study demonstrated that EFV treatment leads to aortic stiffening and remodeling as quantified by compliance measurements and alteration of axial force and *in vivo* axial stretch, respectively. However, plaque progression was not different between groups. The observation of decreased compliance in EFV-treated mice supports the correlation between EFV treatment and increased PWV in aortas that was established in the clinical studies. Animal models offer significant advantages when attempting to study the effects of a drug, especially as it relates to vascular mechanics. Mouse models offer the ability to isolate the effects of the drug from the context of HIV-infection and combined therapy as well as the ability to directly study the behavior of the vasculature (as opposed to the non-invasive methods utilized in clinical studies).

A pronounced gap exists in the lymphatic literature describing the mechanisms driving the onset of lymphedema. Thus, we sought to develop a novel experimental /

theoretical paradigm describing mechanically-mediated remodeling of the lymphatic vasculature in order to provide a useful tool for the investigation of the relationship between mechanics and the onset of lymphedema. We first performed active and passive biaxial mechanical testing of rat thoracic ducts to quantify the mechanical environment of lymphatic vessels using a microstructurally-motivated mathematical model. This model successfully recapitulated the spatial mechanical behavior of rat thoracic ducts including passive transmural pressure vs. diameter behavior, maintenance of basal tone, and contractile amplitude as a function of transmural pressure. Confocal microscopy was performed, and fiber angle orientation was quantified. The results suggested material asymmetry and high degree of variability between specimens. A predictive model of lymph transport was developed that incorporated the material parameters determined from biaxial testing and simulated changes temporal contractile behavior of an isolated lymphangion in response to elevated afterload. Calculation of functional pumping metrics suggested that the predictive capacity of the model was reasonable. This model was then utilized in a model of mechanically-mediated growth and remodeling in order to postulate the effect of the mechanical environment on the progression of lymphatic dysfunction and lymphedema. Simulations suggest that circumferential stress may be the primary mediator of lymphatic growth; however, the model should be interpreted with caution until experimental data can confirm or refute the predictions of the model.

5.2 Limitations

Many limitations in this project motivate the need to perform future studies that improve upon the current results presented here. George E.P. Box stated that, “all models are wrong, but some are useful,” and we have here employed models at multiple

experimental and theoretical models at various scales. Our clinical studies investigating the relationship between treatment with EFV and accelerated progression of CVD utilize statistical models with inherent limitations primarily because of the study design. The study was cross-sectional and therefore does not offer data regarding causal relationships between antiretroviral treatment and markers of CVD. Additionally, the HIV-negative control group in the adult population was recruited by word of mouth and may have been predominantly from the neighboring cardiac facility, thus potentially biasing the results, and the pediatric population was without a control group due to the difficulty of recruitment of children. In all cases, clinical studies contain inherent difficulties when attempting to isolate specific variables, and certainly the population characteristics in our study increase the difficulty in analysis; however, we do not believe that these limitations impede the utility of the data provided. Future clinical studies may include longitudinal data in similar cohorts in order to investigate a causal relationship between EFV treatment and progression of CVD.

On another length scale is the animal model utilized to establish a link between EFV treatment and arterial stiffening. In contrast to the clinical studies, animal models offer a significant advantage in isolating specific variables and carefully controlling the experimental environment. However, animal models also pose obvious difficulties when attempting to interpret data in a clinical light. Our study suggests that treatment with EFV (75 mg/kg) leads arterial stiffening in a mouse model of atherosclerosis. However, it is difficult to interpret data between small rodents and humans. Mice have a significantly higher metabolism than humans, and without a pharmacokinetic study, it is difficult to know that plasma levels of EFV in mice are equivalent to those seen in humans. It should

be noted that the concentration utilized was 10 fold higher than the typical human dose, a value that has been utilized in studies investigating the effects other antiretroviral drugs on vascular dysfunction. Similarly, the physiologic environment within the mouse is not the same as that found in chronically infected HIV-1+ patients receiving HAART. Without the infection and the combination therapy, the interaction between EFV and the vasculature cannot be fully characterized. Additionally, *ex vivo* experiments such as those performed on the murine arteries in specific aim 1 neglect contributions from the perivascular tissue to the mechanical behavior of the artery. In such a case, the *in vivo* geometry and mechanical behavior can only be inferred rather than directly calculated.

Similar *ex vivo* studies were performed with rat thoracic ducts in order to quantify the active and passive mechanical properties of the vessel. The limitations in this case, however, extend beyond simply neglecting the contributions of the surrounding tissue. Microstructurally-motivated mathematical modeling was employed to characterize the mechanical properties of this tissue, and the model contains limitations of its own. We modeled the tissue as a non-linear, pseudo-elastic material comprised of four symmetrically oriented families of collagen fibers and uniformly distributed, isotropic elastin. We also included a tonic and rhythmic contractile response from lymphatic muscle cells using an adapted constitutive equation of active stress. Confocal microscopy revealed that the microstructural organization of the tissue does not contain symmetrically oriented collagen fibers and likely consists of one or two families rather than four. Thus, while the model was capable of predicting bulk pressure vs. diameter and axial force vs. pressure behavior, it cannot truly be characterized as microstructurally-motivated because the material asymmetry is not considered. Material

asymmetry likely leads to a small degree of torsion, which was also neglected in this portion of the project. Future studies of the passive mechanical behavior of lymphatic vessels should seek to better quantify the microstructural organization of the tissue and include material asymmetry and torsional components in the mathematical model. Active stress contributions were considered only for a case without an axial pressure gradient. However, studies have shown that contractile parameters such as frequency, amplitude, and tone are dependent on not only the transmural pressure but also the axial pressure gradient. Future studies should seek to more accurately quantify the active mechanical properties using a model that can include the relationship between contractile parameters and axial pressure gradient. With these limitations in mind, we believe that the utility of the model is not diminished as it still accurately simulates passive and active mechanical properties of the rat thoracic duct and at least begins to bridge the gap between empirical and truly microstructurally-motivated modeling.

Predictive modeling of both lymph transport and lymphatic growth and remodeling contain significant limitations. Accurate prediction of lymph transport requires accurate characterization of contractile behavior and valve behavior as well as quantification of loading (e.g. *in vivo* axial stretch, preload, afterload), geometry (e.g. unloaded thickness and radius), and fluid properties (e.g. viscosity). All of these are difficult enough to accurately quantify, and this does not include any consideration of the biological signaling (e.g. intracellular calcium concentration, pH, production of growth factors, cytokines, etc.) that undoubtedly affect the mechanical behavior of the vessel. Biological signaling aside, we sought to predict lymph transport behavior using the experimentally derived parameters obtained from biaxial testing in conjunction with a

model of Poiseuille flow. Although we made many assumptions and simplifications such as uniform valve behavior, no dependence of tone on fluid shear stress, and no turbulent or backwards flow, our model was still capable of recapitulating data observed for a single isolated lymphangion in the literature. Similarly, growth and remodeling predictions require accurate quantification of the mechanical environment of the tissue, characterization of the microstructure, and ideally consideration of the biological response of each constituent in the microstructure to changes in the mechanical, biological, and chemical environment. A volumetric growth model such as the one proposed here does not account for differential growth patterns of collagen, elastin, and muscle cells. Even the constrained mixture models of in the literature are lacking considerable data because the process driving turnover and deposition of ECM proteins is not well understood. Without any data available addressing remodeling of lymphatics in response to altered loading, a model of growth and remodeling can only be a useful tool for motivating future experimental frameworks. Despite many of the limitations of our model, the theoretical framework motivates future studies on isolated lymphatics and holds the potential for the identification of key parameters driving the remodeling process. As additional data becomes available, the model can be adapted to better support and predict behavior in order to identify such parameters.

Taken together, the limitations of this project represent the myriad of limitations present in modeling techniques that span multiple length scales and experimental settings. Although there were many limitations, this project offers novel insight into the relationship between biomechanics and disease progression in fields which have significant need for additional attention. We have quantified arterial stiffening, a known

preclinical marker of atherosclerosis, using non-invasive techniques in a clinical population of HAART-treated HIV-1+ patients, and we have quantified similar markers using *ex vivo* testing techniques in a mouse model of atherosclerosis. We also used similar *ex vivo* testing techniques and theoretical computational modeling to quantify the passive and active mechanical properties of rat thoracic ducts and predict transport behavior and growth and remodeling of an isolated lymphangion.

5.3 Future directions

The long-term goals of this project are to utilize various modeling techniques to parse out the mechanisms driving mechanically-mediated disease progression. An initial goal in this light is to develop tools and frameworks that support quantification of disease progression, and we have successfully developed such tools by providing a mouse model of EFV-induced arterial stiffening as well as an experimentally-motivated predictive theoretical framework describing lymphatic dysfunction. Studies in the immediate future should seek to add descriptive and predictive capabilities to each of these models. For the clinical model, longitudinal studies should be performed in order to establish a causal relationship between EFV treatment and development of CVD. For the mouse model, studies in the immediate future may include more in-depth quantification of the mechanical changes of the blood vessels in response to EFV treatment (e.g. opening angle, microstructural organization) as has been previously performed [12]. The mouse model also offers the ability to parse out mechanisms driving vascular remodeling. Recent studies have implicated cathepsins in HAART-induced vascular remodeling. Utilization of additional knockout mice, specifically $ApoE^{-/-}$ mice crossed with cathepsin K, cathepsin L, or cathepsin S knockouts can serve as an ideal next step for the

investigation of cathepsin-induced vascular remodeling in association with EFV treatment. Long-term studies should address identification of specific parameters contributing to EFV-induced vascular remodeling and should be coupled with models of HIV infection and eventually quantified in a clinical setting. Clinical verification of mechanisms driving HAART-induced remodeling can ultimately lead to either additional pharmaceutical intervention or development of better antiretrovirals that avoid mechanisms of action that operate on pathways detrimental to vascular health and integrity.

Similarly, studies in the immediate future addressing lymphatic biomechanics should seek to build up the theoretical framework and more accurately quantify the mechanical environment. Experimental setups that support the measurement of torsion may be utilized to better quantify the mechanical behavior of actively contracting lymphatic vessels and would thus support a model that includes shear stress in the wall of the vessel. Additional studies may also seek to quantify the effect of axial stretch on the contractile function of these vessels, a consideration that was neglected in the first milestone of specific aim 2 (note that axial stretch was, however, considered in the passive properties), or studies may address the relationship between axial pressure gradient and contractile function.

It is important to note that quantification of growth and remodeling as it relates to transport function is the primary goal of specific aim 2, and thus the mechanical environment during actual lymph transport should be better characterized. Specifically, valve characteristics are complicated, and accurate quantification of valve characteristics and behavior are critical for the prediction of flow through a lymphangion. Experimental

studies should be performed, noting that some have already tried [126], in order to improve the predictive capability of the transport model. The model should also be expanded to support prediction of flow metrics in a chain of lymphangions rather than a single isolated lymphangion. Similarly, a striking gap exists in the literature describing remodeling of lymphatic vessels in response to altered mechanical loading despite clinical evidence of lymphatic remodeling in the context of lymphedema [16, 271]. Animal models of lymphedema are currently available and may be utilized to quantify changes in geometry, microstructural organization, and cellular phenotype in order to better motivate predictive models of growth and remodeling. Long-term studies may seek to investigate mechanically-sensitive proteins or genes that contribute to changes in lymphatic function and thus provide insight into mechanisms driving lymphatic dysfunction and ultimately identifying targets for therapeutic intervention.

APPENDIX A

Table A.1. Lifestyle, personal and familial history of CVD, and complete blood count (CBC) analysis in an Ethiopian population. Continuous variables are reported as median (interquartile range). A, a = p<0.005 or p<0.05 versus HIV-negative controls, respectively; B, b = p<0.005 or p<0.05 versus HAART-naive, respectively; D, d = p<0.005 or p<0.05 versus EFV, respectively; E, e = p<0.005 or p<0.05 versus NVP, respectively.

End-point	HIV-Negative (n= 36)	HAART Naïve (n= 51)	Efavirenz (EFV) (n= 91)	Nevarapine (NVP) (n= 95)	Lopinavir/r (LPV/r) (n= 44)
Lifestyle					
Lifetime >100 Cigarettes [%]	6%	4%	8%	6%	11%
Current smoker [%]	3%	2%	0%	2%	0%
Consume ≥1 drinks/month [%]	75%	63%	46% [a]	44% [a]	48%
Consume >4 drink/week [%]	3%	6%	3%	2%	2%
Personal History of CVD					
HA, Angina, or Stroke [%]	3%	4%	4%	2%	0%
Kidney Disease [%]	3%	8%	7%	5%	2%
Lipid Disorders [%]	0%	4%	5%	4%	9%
Family History of CVD					
HA, Angina, or Stroke [%]	0%	6%	4%	9%	14%
Kidney Disease [%]	0%	2%	0%	3%	5% [d]
Diabetes [%]	6%	4%	12%	16%	11%
Lipid Disorders [%]	0%	0%	0%	0%	2%
Blood Sample Analysis					
Complete Blood Count					
WBC [10^3/uL]	**6.01** (4.55 - 6.71)	**5.40** (4.29 - 6.49)	**5.69** (4.12 - 6.96)	**4.86** (3.83 - 6.48)	**4.95** (4.06 - 5.89)
Neu [%]	**56.6** (46.6 - 63.3)	**51.3** (42.9 - 60.5)	**54.7** (41.6 - 63.9)	**50.8** (42.3 - 59.6)	**52.8** (43.3 - 62.7)
Lym [%]	**34.4** (26.3 - 45.1)	**34.9** (28.4 - 45.8)	**33.9** (26.9 - 44.6)	**39.2** (30.1 - 47.7)	**37.2** (29.9 - 41.3)
Mon [%]	**3.4** (2.6 - 5.6)	**4.3** (2.8 - 6.0)	**4.2** (2.9 - 6.6)	**4.9** (2.8 - 6.7)	**5.5** (3.6 - 7.4)
Eos [%]	**3.5** (2.1 - 5.3)	**3.9** (2.0 - 6.9)	**3.5** (1.6 - 7.0)	**3.7** (2.0 - 6.1)	**4.1** (2.4 - 6.1)
Bas [%]	**0.5** (0.4 - 0.8)	**0.4** (0.3 - 0.6)	**0.5** (0.3 - 0.6)	**0.5** (0.3 - 0.7)	**0.6** (0.4 - 0.8)
MID [%]	**8.0** (6.2 - 11.1)	**9.7** (7.0 - 13.8)	**9.1** (7.3 - 13.4)	**8.9** (6.8 - 13.3)	**10.5** (8.5 - 13.4)
Neu # [10^3/uL]	**3.32** (2.01 - 4.48)	**2.76** (1.80 - 3.86)	**2.90** (1.83 - 4.28)	**2.29** (1.71 - 3.17)	**2.36** (1.70 - 3.18)
Lym # [10^3/uL]	**2.01** (1.59 - 2.31)	**1.94** (1.39 - 2.42)	**1.85** (1.50 - 2.20)	**1.83** (1.37 - 2.31)	**1.70** (1.37 - 2.32)
Mon # [10^3/uL]	**0.19** (0.15 - 0.31)	**0.22** (0.17 - 0.31)	**0.22** (0.14 - 0.36)	**0.21** (0.14 - 0.35)	**0.28** (0.15 - 0.35)
Eos # [10^3/uL]	**0.21** (0.10 - 0.35)	**0.22** (0.09 - 0.37)	**0.17** (0.09 - 0.37)	**0.17** (0.07 - 0.29)	**0.18** (0.11 - 0.33)
Bas # [10^3/uL]	**0.03** (0.02 - 0.04)	**0.02** (0.0 - 0.0)	**0.02** (0.01 - 0.03)	**0.02** (0.01 - 0.04)	**0.03** (0.02 - 0.03)
MID [#]	**0.46** (0.37 - 0.64)	**0.49** (0.35 - 0.75)	**0.50** (0.34 - 0.71)	**0.41** (0.30 - 0.67)	**0.55** (0.37 - 0.69)
RBC [10^6/uL]	**5.14** (4.76 - 5.31)	**4.84** (4.43 - 5.29)	**4.40** (4.05 - 4.67) [A,B]	**4.07** (3.68 - 4.57) [A,B,D]	**4.33** (3.98 - 4.53) [A,B]
HGB [g/dL]	**15.3** (14.6 - 16.3)	**14.9** (13.8 - 15.7) [a]	**15.0** (14.1 - 15.8)	**15.0** (14.1 - 15.7) [a]	**14.4** (13.6 - 15.2) [A,d,e]
HCT [%]	**44.5** (43.2 - 47.9)	**43.5** (40.2 - 46.1) [a]	**43.1** (41.2 - 45.0) [A]	**42.6** (40.5 - 45.6) [A]	**42.5** (40.0 - 44.4) [A]
MCV [fL]	**89.3** (86.6 - 92.4)	**88.7** (85.8 - 92.5)	**97.8** (91.6 - 105.2) [A,B]	**104.6** (97.5 - 113.8) [A,B,D]	**98.4** (95.1 - 103.6) [A,B,E]
MCH [pg]	**30.5** (29.7 - 31.6)	**30.2** (29.1 - 31.6)	**34.0** (32.0 - 37.1) [A,B]	**36.5** (33.3 - 40.2) [A,B,D]	**33.2** (32.2 - 36.6) [A,B,E]
MCHC [g/dL]	**34.4** (33.9 - 34.6)	**34.1** (33.3 - 34.4)	**34.5** (33.6 - 35.3) [b]	**34.7** (33.8 - 35.4) [a,B]	**34.2** (33.3 - 34.8) [d,E]
RDW-CV [%]	**12.2** (12.0 - 12.5)	**12.6** (12.2 - 13.2) [a]	**12.9** (12.2 - 13.9) [A]	**12.1** (11.6 - 12.8) [B,D]	**12.6** (12.0 - 13.4) [e]
RDW-SD [fL]	**45.0** (43.4 - 46.6)	**46.1** (44.6 - 47.9)	**50.0** (47.6 - 52.7) [A,B]	**51.2** (47.5 - 55.0) [A,B]	**49.6** (47.4 - 54.5) [A,B]
PLT [103/uL]	**254** (213 - 282)	**247** (206 - 275)	**273** (233 - 331) [a,B]	**243** (197 - 279) [D]	**246** (210 - 281) [D]
MPV [fL]	**9.5** (9.0 - 10.2)	**9.1** (8.7 - 9.9)	**8.9** (8.0 - 9.6) [A]	**8.8** (8.3 - 9.7) [a]	**9.1** (8.7 - 10.1)
PDW	**16.0** (15.7 - 16.2)	**15.9** (15.8 - 16.1)	**15.8** (15.1 - 16.1)	**15.8** (12.2 - 16.2)	**15.9** (15.6 - 16.2)
PCT [%]	**0.238** (0.206 - 0.272)	**0.220** (0.194 - 0.257)	**0.250** (0.210 - 0.287) [B]	**0.209** (0.181 - 0.245) [a,D]	**0.218** (0.197 - 0.249) [D]

APPENDIX B

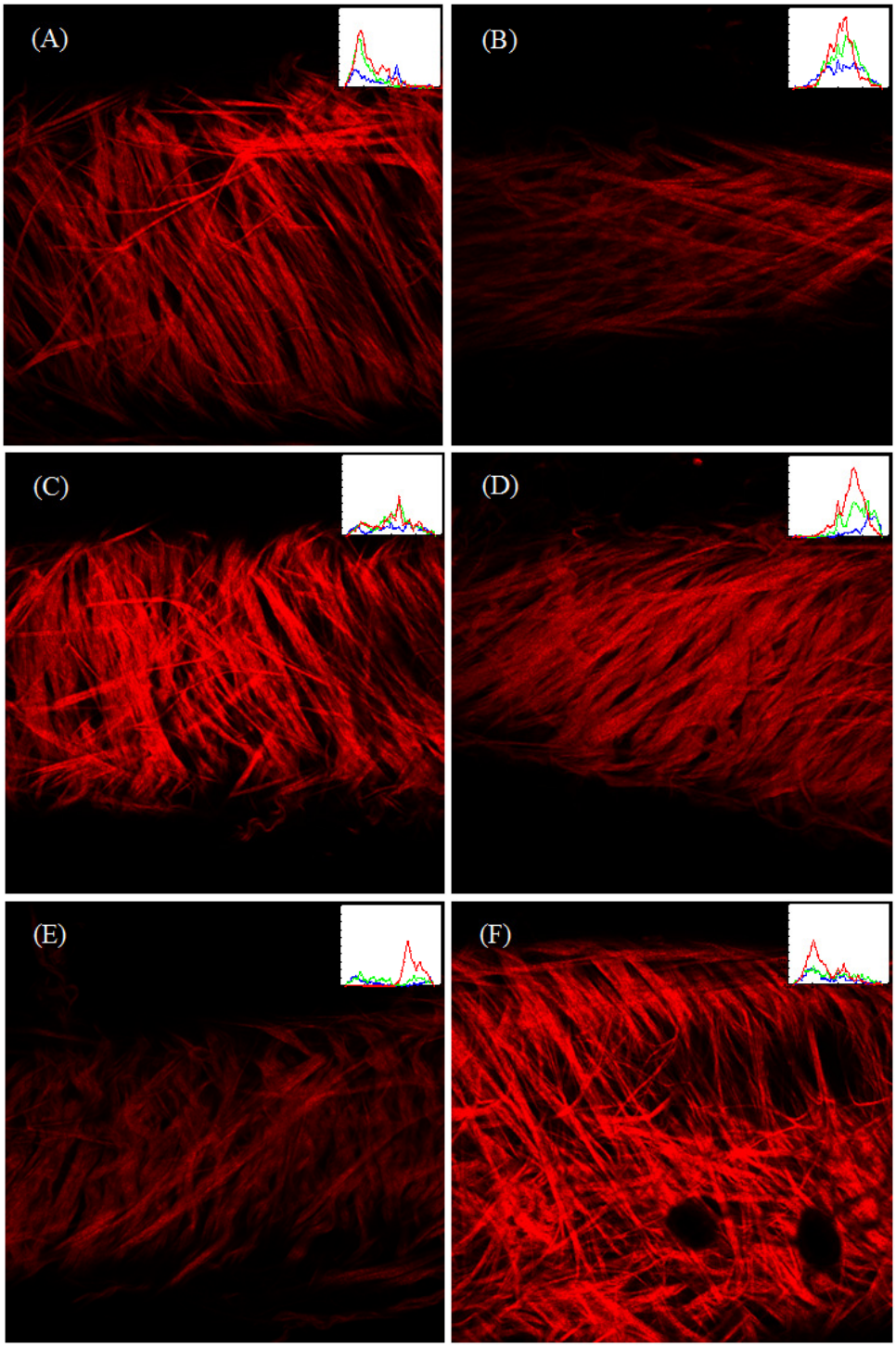

Figure B.1. Confocal imaging results from 6 rat thoracic ducts at high loading conditions with overlays of angle orientation results.

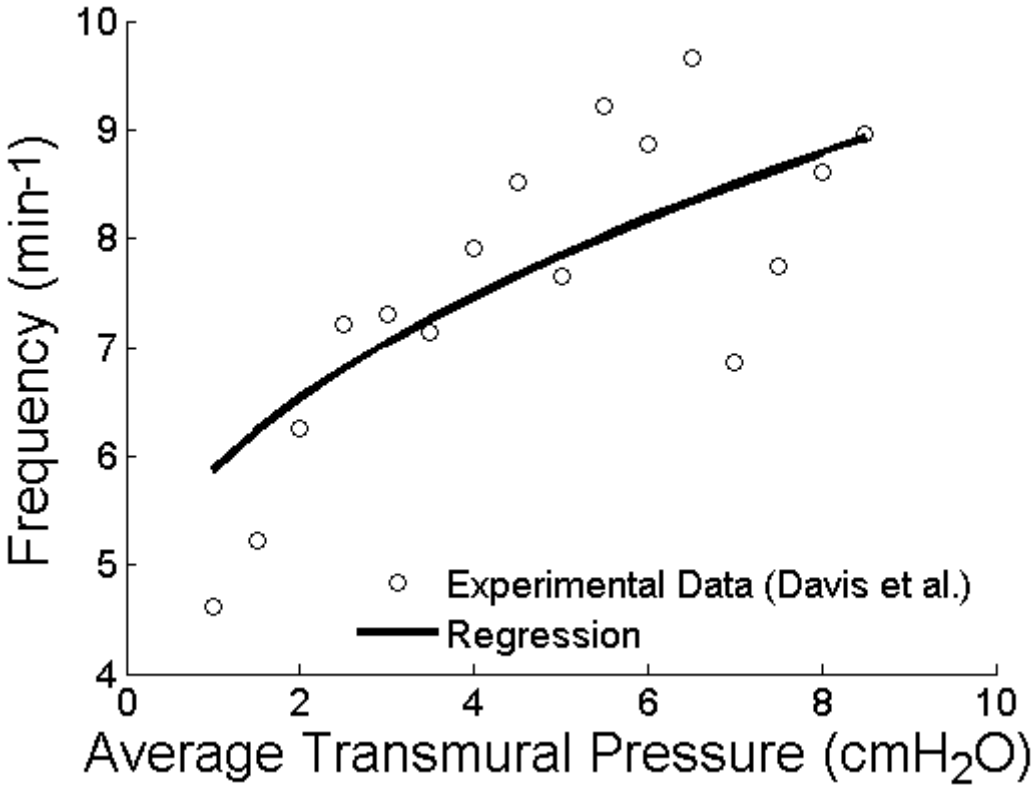

Figure B.2. Non-linear regression results for contractile frequency vs. transmural pressure data from the literature.

REFERENCES

1. Salomon, J.A., et al., *Healthy life expectancy for 187 countries, 1990-2010: a systematic analysis for the Global Burden Disease Study 2010.* Lancet, 2012. **380**(9859): p. 2144-62.
2. UNAIDS. *Global report on the AIDS epidemic*. Sub-Saharan Africa regional fact sheet 2012 [cited 2015 April 1]; Available from: www.unaids.org/sites/default/files/en/media/unaids/contentassets/documents/epidemiology/2012/gr2012/2012_FS_regional_ssa_en.pdf.
3. Orlando, G., et al., *Antiretroviral treatment and age-related comorbidities in a cohort of older HIV-infected patients.* HIV Med, 2006. **7**(8): p. 549-57.
4. WHO, *Progress report on the global program to eliminate lymphatic filariasis*. 2010.
5. Hotez, P.J. and A. Kamath, *Neglected tropical diseases in sub-saharan Africa: review of their prevalence, distribution, and disease burden.* PLoS Negl Trop Dis, 2009. **3**(8): p. e412.
6. Ingber, D.E., *Mechanobiology and diseases of mechanotransduction.* Ann Med, 2003. **35**(8): p. 564-77.
7. Friis-Moller, N., et al., *Cardiovascular disease risk factors in HIV patients--association with antiretroviral therapy. Results from the DAD study.* AIDS, 2003. **17**(8): p. 1179-93.
8. Jamaluddin, M.S., et al., *Non-nucleoside reverse transcriptase inhibitor efavirenz increases monolayer permeability of human coronary artery endothelial cells.* Atherosclerosis, 2010. **208**(1): p. 104-11.
9. Gupta, S.K., et al., *Worsening Endothelial Function with Efavirenz Compared to Protease Inhibitors: A 12-Month Prospective Study.* PLoS One, 2012. **7**(9): p. e45716.
10. Apostolova, N., et al., *Enhanced oxidative stress and increased mitochondrial mass during efavirenz-induced apoptosis in human hepatic cells.* Br J Pharmacol, 2010. **160**(8): p. 2069-84.
11. Blas-Garcia, A., et al., *Inhibition of mitochondrial function by efavirenz increases lipid content in hepatic cells.* Hepatology, 2010. **52**(1): p. 115-25.
12. Hansen, L., et al., *Azidothymidine (AZT) leads to arterial stiffening and intima-media thickening in mice.* J Biomech, 2013. **46**(9): p. 1540-7.
13. Davis, M.J., et al., *Intrinsic increase in lymphangion muscle contractility in response to elevated afterload.* Am J Physiol Heart Circ Physiol, 2012. **303**(7): p. H795-808.
14. Gashev, A.A., M.J. Davis, and D.C. Zawieja, *Inhibition of the active lymph pump by flow in rat mesenteric lymphatics and thoracic duct.* J Physiol, 2002. **540**(Pt 3): p. 1023-37.
15. Wolinsky, H., *Response of the rat aortic media to hypertension. Morphological and chemical studies.* Circ Res, 1970. **26**(4): p. 507-22.
16. Mihara, M., et al., *Pathological steps of cancer-related lymphedema: histological changes in the collecting lymphatic vessels after lymphadenectomy.* PLoS One, 2012. **7**(7): p. e41126.

17. Humphrey, J.D. and SpringerLink (Online service), *Cardiovascular Solid Mechanics Cells, Tissues, and Organs*. 2002, Springer New York : Imprint: Springer: New York, NY.
18. Furchgott, R.F. and J.V. Zawadzki, *The obligatory role of endothelial cells in the relaxation of arterial smooth muscle by acetylcholine.* Nature, 1980. **288**(5789): p. 373-6.
19. Roger, V.L., et al., *Heart disease and stroke statistics--2012 update: a report from the American Heart Association.* Circulation, 2012. **125**(1): p. e2-e220.
20. WHO, *Global Atlas on Cardiovascular Disease Prevention and Control*. 2011.
21. Yusuf, S., et al., *Global burden of cardiovascular diseases: part I: general considerations, the epidemiologic transition, risk factors, and impact of urbanization.* Circulation, 2001. **104**(22): p. 2746-53.
22. Ross, R., *Atherosclerosis--an inflammatory disease.* N Engl J Med, 1999. **340**(2): p. 115-26.
23. Davignon, J. and P. Ganz, *Role of endothelial dysfunction in atherosclerosis.* Circulation, 2004. **109**(23 Suppl 1): p. III27-32.
24. Nam, D., et al., *Partial carotid ligation is a model of acutely induced disturbed flow, leading to rapid endothelial dysfunction and atherosclerosis.* Am J Physiol Heart Circ Physiol, 2009. **297**(4): p. H1535-43.
25. Conway, D.E., et al., *Endothelial cell responses to atheroprone flow are driven by two separate flow components: low time-average shear stress and fluid flow reversal.* Am J Physiol Heart Circ Physiol, 2010. **298**(2): p. H367-74.
26. Conway, D.E., et al., *Fluid shear stress on endothelial cells modulates mechanical tension across VE-cadherin and PECAM-1.* Curr Biol, 2013. **23**(11): p. 1024-30.
27. Ku, D.N., et al., *Pulsatile flow and atherosclerosis in the human carotid bifurcation. Positive correlation between plaque location and low oscillating shear stress.* Arteriosclerosis, 1985. **5**(3): p. 293-302.
28. Doran, A.C., N. Meller, and C.A. McNamara, *Role of smooth muscle cells in the initiation and early progression of atherosclerosis.* Arterioscler Thromb Vasc Biol, 2008. **28**(5): p. 812-9.
29. Laurent, S., et al., *Aortic stiffness is an independent predictor of all-cause and cardiovascular mortality in hypertensive patients.* Hypertension, 2001. **37**(5): p. 1236-41.
30. Lorenz, M.W., et al., *Prediction of clinical cardiovascular events with carotid intima-media thickness: a systematic review and meta-analysis.* Circulation, 2007. **115**(4): p. 459-67.
31. Corretti, M.C., et al., *Guidelines for the ultrasound assessment of endothelial-dependent flow-mediated vasodilation of the brachial artery: a report of the International Brachial Artery Reactivity Task Force.* J Am Coll Cardiol, 2002. **39**(2): p. 257-65.
32. Echocardiography, A.S.o., *Use of carotid ultrasound to identify subclinical vascular disease and evaluate cardiovascular disease risk: A consensus statement from the American Society of Echocardiography carotid intima-media thickness task force*. 2008.

33. Laurent, S., et al., *Expert consensus document on arterial stiffness: methodological issues and clinical applications.* Eur Heart J, 2006. **27**(21): p. 2588-605.
34. Greene, W.C., *A history of AIDS: looking back to see ahead.* Eur J Immunol, 2007. **37 Suppl 1**: p. S94-102.
35. *A timeline of AIDS*. 2012 [cited 2015 April 1]; Available from: https://www.aids.gov/hiv-aids-basics/hiv-aids-101/aids-timeline/.
36. Turner, B.G. and M.F. Summers, *Structural biology of HIV*. J Mol Biol, 1999. **285**(1): p. 1-32.
37. DHHS. *Guidelines for the use of antiretroviral agents in HIV-1-infected adults and adolescents*. 2014 [cited 2015 January 13]; Available from: http://aidsinfo.nih.gov/ContentFiles/AdultandAdolescentGL.pdf.
38. Warnke, D., J. Barreto, and Z. Temesgen, *Antiretroviral drugs.* J Clin Pharmacol, 2007. **47**(12): p. 1570-9.
39. Pommier, Y., A.A. Johnson, and C. Marchand, *Integrase inhibitors to treat HIV/AIDS.* Nat Rev Drug Discov, 2005. **4**(3): p. 236-48.
40. Guaraldi, G., et al., *Premature age-related comorbidities among HIV-infected persons compared with the general population.* Clin Infect Dis, 2011. **53**(11): p. 1120-6.
41. Bozzette, S.A., et al., *Cardiovascular and cerebrovascular events in patients treated for human immunodeficiency virus infection.* N Engl J Med, 2003. **348**(8): p. 702-10.
42. Bozzette, S.A., et al., *Long-term survival and serious cardiovascular events in HIV-infected patients treated with highly active antiretroviral therapy.* J Acquir Immune Defic Syndr, 2008. **47**(3): p. 338-41.
43. Friis-Moller, N., et al., *Combination antiretroviral therapy and the risk of myocardial infarction.* N Engl J Med, 2003. **349**(21): p. 1993-2003.
44. Mary-Krause, M., et al., *Increased risk of myocardial infarction with duration of protease inhibitor therapy in HIV-infected men.* AIDS, 2003. **17**(17): p. 2479-86.
45. Spieker, L.E., et al., *Rapid progression of atherosclerotic coronary artery disease in patients with human immunodeficiency virus infection.* Heart Vessels, 2005. **20**(4): p. 171-4.
46. Maggi, P., et al., *Colour-Doppler ultrasonography of carotid vessels in patients treated with antiretroviral therapy: a comparative study.* AIDS, 2004. **18**(7): p. 1023-8.
47. Boccara, F., *Cardiovascular complications and atherosclerotic manifestations in the HIV-infected population: type, incidence and associated risk factors.* AIDS, 2008. **22 Suppl 3**: p. S19-26.
48. van Vonderen, M.G., et al., *Increase in carotid artery intima-media thickness and arterial stiffness but improvement in several markers of endothelial function after initiation of antiretroviral therapy.* J Infect Dis, 2009. **199**(8): p. 1186-94.
49. Sevastianova, K., et al., *Arterial stiffness in HIV-infected patients receiving highly active antiretroviral therapy.* Antivir Ther, 2005. **10**(8): p. 925-35.
50. Kaplan, R.C., et al., *T cell activation predicts carotid artery stiffness among HIV-infected women.* Atherosclerosis, 2011. **217**(1): p. 207-13.

51. Hsue, P.Y., et al., *Progression of atherosclerosis as assessed by carotid intima-media thickness in patients with HIV infection.* Circulation, 2004. **109**(13): p. 1603-8.
52. Hsue, P.Y., et al., *Association of abacavir and impaired endothelial function in treated and suppressed HIV-infected patients.* AIDS, 2009. **23**(15): p. 2021-7.
53. Shankar, S.S., et al., *Indinavir impairs endothelial function in healthy HIV-negative men.* Am Heart J, 2005. **150**(5): p. 933.
54. Joshi, V.V., et al., *Arteriopathy in children with acquired immune deficiency syndrome.* Pediatr Pathol, 1987. **7**(3): p. 261-75.
55. Paton, P., et al., *Coronary artery lesions and human immunodeficiency virus infection.* Res Virol, 1993. **144**(3): p. 225-31.
56. Hansen, L., et al., *Endothelial dysfunction, arterial stiffening, and intima-media thickening in large arteries from HIV-1 transgenic mice.* Ann Biomed Eng, 2013. **41**(4): p. 682-93.
57. Kline, E.R., et al., *Vascular oxidative stress and nitric oxide depletion in HIV-1 transgenic rats are reversed by glutathione restoration.* Am J Physiol Heart Circ Physiol, 2008. **294**(6): p. H2792-804.
58. Parker, I.K., et al., *Pro-atherogenic shear stress and HIV proteins synergistically upregulate cathepsin K in endothelial cells.* Ann Biomed Eng, 2014. **42**(6): p. 1185-94.
59. Asztalos, B.F., et al., *Circulating Nef induces dyslipidemia in simian immunodeficiency virus-infected macaques by suppressing cholesterol efflux.* J Infect Dis, 2010. **202**(4): p. 614-23.
60. Lorenz, M.W., et al., *Both long-term HIV infection and highly active antiretroviral therapy are independent risk factors for early carotid atherosclerosis.* Atherosclerosis, 2008. **196**(2): p. 720-726.
61. Grubb, J.R., et al., *Lopinavir-ritonavir: effects on endothelial cell function in healthy subjects.* J Infect Dis, 2006. **193**(11): p. 1516-9.
62. Paladugu, R., et al., *Hiv Tat protein causes endothelial dysfunction in porcine coronary arteries.* J Vasc Surg, 2003. **38**(3): p. 549-55; discussion 555-6.
63. Chiodelli, P., et al., *Sialic acid associated with alphavbeta3 integrin mediates HIV-1 Tat protein interaction and endothelial cell proangiogenic activation.* J Biol Chem, 2012. **287**(24): p. 20456-66.
64. Rusnati, M. and M. Presta, *HIV-1 Tat protein and endothelium: from protein/cell interaction to AIDS-associated pathologies.* Angiogenesis, 2002. **5**(3): p. 141-51.
65. Urbinati, C., et al., *Integrin alphavbeta3 as a target for blocking HIV-1 Tat-induced endothelial cell activation in vitro and angiogenesis in vivo.* Arterioscler Thromb Vasc Biol, 2005. **25**(11): p. 2315-20.
66. Urbinati, C., et al., *Substrate-immobilized HIV-1 Tat drives VEGFR2/alpha(v)beta(3)-integrin complex formation and polarization in endothelial cells.* Arterioscler Thromb Vasc Biol, 2012. **32**(5): p. e25-34.
67. Andras, I.E., et al., *HIV-1 Tat protein alters tight junction protein expression and distribution in cultured brain endothelial cells.* J Neurosci Res, 2003. **74**(2): p. 255-65.
68. Price, T.O., et al., *HIV-1 viral proteins gp120 and Tat induce oxidative stress in brain endothelial cells.* Brain Res, 2005. **1045**(1-2): p. 57-63.

69. Louboutin, J.P., et al., *HIV-1 gp120-induced injury to the blood-brain barrier: role of metalloproteinases 2 and 9 and relationship to oxidative stress.* J Neuropathol Exp Neurol, 2010. **69**(8): p. 801-16.
70. Toborek, M., et al., *HIV-Tat protein induces oxidative and inflammatory pathways in brain endothelium.* J Neurochem, 2003. **84**(1): p. 169-79.
71. van Vonderen, M., et al., *Increase in carotid artery intima-media thickness and arterial stiffness but improvement in several markers of endothelial function after initiation of antiretroviral therapy.* Journal of Infectious Diseases, 2009. **199**(8): p. 1186-1194.
72. Kaplan, R.C., et al., *T cell activation predicts carotid artery stiffness among HIV-infected women.* Atherosclerosis, 2011.
73. Sevastianova, K., et al., *Arterial stiffness in HIV-infected patients receiving highly active antiretroviral therapy.* Antivir Ther, 2005. **10**(8): p. 925-935.
74. Seaberg, E.C., et al., *Association between human immunodeficiency virus infection and stiffness of the common carotid artery.* Stroke, 2010. **41**(10): p. 2163-2170.
75. Stein, J., et al., *Use of human immunodeficiency virus-1 protease inhibitors is associated with atherogenic lipoprotein changes and endothelial dysfunction.* Circulation, 2001. **104**(3): p. 257-262.
76. Shankar, S., et al., *Indinavir impairs endothelial function in healthy HIV-negative men.* American Heart Journal, 2005. **150**(5): p. 933.
77. Gupta, S.K., et al., *Worsening endothelial function with efavirenz compared to protease inhibitors: a 12-month prospective study.* PloS one, 2012. **7**(9): p. e45716.
78. Lorenz, M., et al., *Both long-term HIV infection and highly active antiretroviral therapy are independent risk factors for early carotid atherosclerosis.* Atherosclerosis, 2008. **196**(2): p. 720-726.
79. Jiang, B., et al., *HIV antiretroviral drug combination induces endothelial mitochondrial dysfunction and reactive oxygen species production, but not apoptosis.* Toxicol Appl Pharmacol, 2007. **224**(1): p. 60-71.
80. Jiang, B., et al., *Antiretrovirals induce endothelial dysfunction via an oxidant-dependent pathway and promote neointimal hyperplasia.* Toxicol Sci, 2010. **117**(2): p. 524-36.
81. Kline, E.R., et al., *Long-term exposure to AZT, but not d4T, increases endothelial cell oxidative stress and mitochondrial dysfunction.* Cardiovasc Toxicol, 2009. **9**(1): p. 1-12.
82. Sutliff, R., et al., *Nucleoside reverse transcriptase inhibitors impair endothelium-dependent relaxation by increasing superoxide.* American Journal of Physiology: Heart and Circulatory Physiology, 2002. **283**: p. H2363-H2370.
83. Jiang, B., et al., *HIV-1 antiretrovirals induce oxidant injury and increase intima-media thickness in an atherogenic mouse model.* Toxicol Lett, 2009. **187**(3): p. 164-71.
84. van Wijk, J.P., et al., *Functional and structural markers of atherosclerosis in human immunodeficiency virus-infected patients.* Journal of the American College of Cardiology, 2006. **47**(6): p. 1117-1123.

85. Johnsen, S., et al., *Carotid intimal medial thickness in human immunodeficiency virus-infected women: effects of protease inhibitor use, cardiac risk factors, and the metabolic syndrome.* Journal of Clinical Endocrinology and Metabolism, 2006. **91**(12): p. 4916-24.
86. Stein, J.H., et al., *Use of human immunodeficiency virus-1 protease inhibitors is associated with atherogenic lipoprotein changes and endothelial dysfunction.* Circulation, 2001. **104**(3): p. 257-62.
87. Shankar, S.S., et al., *Indinavir impairs endothelial function in healthy HIV-negative men.* American Heart Journal, 2005. **150**(5): p. 933.
88. Blanco, J.J., et al., *Endothelial function in HIV-infected patients with low or mild cardiovascular risk.* Journal of Antimicrobial Chemotherapy, 2006. **58**(1): p. 133-9.
89. Fontas, E., et al., *Lipid profiles in HIV-infected patients receiving combination antiretroviral therapy: are different antiretroviral drugs associated with different lipid profiles?* Journal of Infectious Diseases, 2004. **189**(6): p. 1056-1074.
90. Fisher, S.D., T.L. Miller, and S.E. Lipshultz, *Impact of HIV and highly active antiretroviral therapy on leukocyte adhesion molecules, arterial inflammation, dyslipidemia, and atherosclerosis.* Atherosclerosis, 2006. **185**(1): p. 1-11.
91. Worm, S.W., et al., *Risk of myocardial infarction in patients with HIV infection exposed to specific individual antiretroviral drugs from the 3 major drug classes: the data collection on adverse events of anti-HIV drugs (D:A:D) study.* Journal of Infectious Diseases, 2010. **201**(3): p. 318-30.
92. Currier, J.S., et al., *Progression of carotid artery intima-media thickening in HIV-infected and uninfected adults.* AIDS, 2007. **21**(9): p. 1137-45.
93. Currier, J.S., et al., *Carotid artery intima-media thickness and HIV infection: traditional risk factors overshadow impact of protease inhibitor exposure.* AIDS, 2005. **19**(9): p. 927-33.
94. Grubb, J.R., et al., *Lopinavir-ritonavir: effects on endothelial cell function in healthy subjects.* Journal of Infectious Diseases, 2006. **193**(11): p. 1516-9.
95. Nolan, D., et al., *Endothelial function in HIV-infected patients receiving protease inhibitor therapy: does immune competence affect cardiovascular risk?* QJM, 2003. **96**(11): p. 825-32.
96. Solages, A., et al., *Endothelial function in HIV-infected persons.* Clinical Infectious Diseases, 2006. **42**(9): p. 1325-32.
97. Pilon, A.A., et al., *Induction of apoptosis by a nonnucleoside human immunodeficiency virus type 1 reverse transcriptase inhibitor.* Antimicrob Agents Chemother, 2002. **46**(8): p. 2687-91.
98. Mondal, D., et al., *HAART drugs induce oxidative stress in human endothelial cells and increase endothelial recruitment of mononuclear cells: exacerbation by inflammatory cytokines and amelioration by antioxidants.* Cardiovasc Toxicol, 2004. **4**(3): p. 287-302.
99. Roy, C.S., *The Elastic Properties of the Arterial Wall.* J Physiol, 1881. **3**(2): p. 125-59.
100. Ding, Z. and M.H. Friedman, *Dynamics of human coronary arterial motion and its potential role in coronary atherogenesis.* J Biomech Eng, 2000. **122**(5): p. 488-92.

101. Roach, M.R. and A.C. Burton, *The reason for the shape of the distensibility curves of arteries.* Can J Biochem Physiol, 1957. **35**(8): p. 681-90.
102. Wang, R. and R.L. Gleason, Jr., *A mechanical analysis of conduit arteries accounting for longitudinal residual strains.* Ann Biomed Eng, 2010. **38**(4): p. 1377-87.
103. Chuong, C.J. and Y.C. Fung, *On residual stresses in arteries.* J Biomech Eng, 1986. **108**(2): p. 189-92.
104. VAISHNAV, R.N., J.T. YOUNG, and D.J. PATEL, *Distribution of Stresses and of Strain-Energy Density through the Wall Thickness in a Canine Aortic Segment.* Circulation Research, 1973. **32**(5): p. 577-583.
105. Fung, Y.C., K. Fronek, and P. Patitucci, *Pseudoelasticity of arteries and the choice of its mathematical expression.* Am J Physiol, 1979. **237**(5): p. H620-31.
106. Takamizawa, K. and K. Hayashi, *Strain energy density function and uniform strain hypothesis for arterial mechanics.* Journal of Biomechanics, 1987. **20**(1): p. 7-17.
107. Delfino, A., et al., *Residual strain effects on the stress field in a thick wall finite element model of the human carotid bifurcation.* J Biomech, 1997. **30**(8): p. 777-86.
108. Holzapfel, G., T. Gasser, and R. Ogden, *A New Constitutive Framework for Arterial Wall Mechanics and a Comparative Study of Material Models.* Journal of elasticity and the physical science of solids, 2000. **61**(1-3): p. 1-48.
109. Zulliger, M.A., et al., *A strain energy function for arteries accounting for wall composition and structure.* J Biomech, 2004. **37**(7): p. 989-1000.
110. Wan, W., J.B. Dixon, and R.L. Gleason, Jr., *Constitutive modeling of mouse carotid arteries using experimentally measured microstructural parameters.* Biophys J, 2012. **102**(12): p. 2916-25.
111. Rachev, A. and K. Hayashi, *Theoretical study of the effects of vascular smooth muscle contraction on strain and stress distributions in arteries.* Ann Biomed Eng, 1999. **27**(4): p. 459-68.
112. Wan, W., H. Yanagisawa, and R. Gleason, *Biomechanical and Microstructural Properties of Common Carotid Arteries from Fibulin-5 Null Mice.* Annals of Biomedical Engineering, 2010. **38**(12): p. 3605-3617.
113. Kamiya, A. and T. Togawa, *Adaptive regulation of wall shear stress to flow change in the canine carotid artery.* Am J Physiol, 1980. **239**(1): p. H14-21.
114. Clark, J.M. and S. Glagov, *Structural integration of the arterial wall. I. Relationships and attachments of medial smooth muscle cells in normally distended and hyperdistended aortas.* Lab Invest, 1979. **40**(5): p. 587-602.
115. Jackson, Z.S., A.I. Gotlieb, and B.L. Langille, *Wall tissue remodeling regulates longitudinal tension in arteries.* Circ Res, 2002. **90**(8): p. 918-25.
116. Skalak, R., et al., *Compatibility and the genesis of residual stress by volumetric growth.* J Math Biol, 1996. **34**(8): p. 889-914.
117. Taber, L.A., *A model for aortic growth based on fluid shear and fiber stresses.* J Biomech Eng, 1998. **120**(3): p. 348-54.
118. Gleason, R.L. and J.D. Humphrey, *A 2D constrained mixture model for arterial adaptations to large changes in flow, pressure and axial stretch.* Mathematical Medicine and Biology, 2005. **22**(4): p. 347-369.

119. Gleason, R.L., L.A. Taber, and J.D. Humphrey, *A 2-D Model of Flow-Induced Alterations in the Geometry, Structure, and Properties of Carotid Arteries.* Journal of Biomechanical Engineering, 2004. **126**(3): p. 371-381.
120. Humphrey, J.D. and K.R. Rajagopal, *A constrained mixture model for arterial adaptations to a sustained step change in blood flow.* Biomech Model Mechanobiol, 2003. **2**(2): p. 109-26.
121. Valentín, A., et al., *Complementary vasoactivity and matrix remodelling in arterial adaptations to altered flow and pressure.* Journal of The Royal Society Interface, 2009. **6**(32): p. 293-306.
122. Wan, W., L. Hansen, and R. Gleason, Jr., *A 3-D constrained mixture model for mechanically mediated vascular growth and remodeling.* Biomechanics and Modeling in Mechanobiology, 2010. **9**(4): p. 403-419.
123. Alitalo, K., *The lymphatic vasculature in disease.* Nat Med, 2011. **17**(11): p. 1371-80.
124. Gasheva, O.Y., D.C. Zawieja, and A.A. Gashev, *Contraction-initiated NO-dependent lymphatic relaxation: a self-regulatory mechanism in rat thoracic duct.* J Physiol, 2006. **575**(Pt 3): p. 821-32.
125. Bridenbaugh, E.A., A.A. Gashev, and D.C. Zawieja, *Lymphatic muscle: a review of contractile function.* Lymphat Res Biol, 2003. **1**(2): p. 147-58.
126. Davis, M.J., et al., *Determinants of valve gating in collecting lymphatic vessels from rat mesentery.* Am J Physiol Heart Circ Physiol, 2011. **301**(1): p. H48-60.
127. Nakamura, K. and S.G. Rockson, *The role of the lymphatic circulation in the natural history and expression of cardiovascular disease.* Int J Cardiol, 2008. **129**(3): p. 309-17.
128. Rader, D.J., et al., *The role of reverse cholesterol transport in animals and humans and relationship to atherosclerosis.* J Lipid Res, 2009. **50 Suppl**: p. S189-94.
129. Lim, H.Y., et al., *Hypercholesterolemic Mice Exhibit Lymphatic Vessel Dysfunction and Degeneration.* The American Journal of Pathology, 2009. **175**(3): p. 1328-1337.
130. Martel, C., et al., *Lymphatic vasculature mediates macrophage reverse cholesterol transport in mice.* J Clin Invest, 2013. **123**(4): p. 1571-9.
131. Kholova, I., et al., *Lymphatic vasculature is increased in heart valves, ischaemic and inflamed hearts and in cholesterol-rich and calcified atherosclerotic lesions.* Eur J Clin Invest, 2011. **41**(5): p. 487-97.
132. Nakano, T., et al., *Angiogenesis and lymphangiogenesis and expression of lymphangiogenic factors in the atherosclerotic intima of human coronary arteries.* Hum Pathol, 2005. **36**(4): p. 330-40.
133. Grabner, R., et al., *Lymphotoxin beta receptor signaling promotes tertiary lymphoid organogenesis in the aorta adventitia of aged ApoE-/- mice.* J Exp Med, 2009. **206**(1): p. 233-48.
134. Gloviczki, P., et al., *Ultrastructural and electrophysiologic changes of experimental acute cardiac lymphostasis.* Lymphology, 1983. **16**(3): p. 185-92.
135. Sun, S.C. and J.T. Lie, *Cardiac lymphatic obstruction: ultrastructure of acute-phase myocardial injury in dogs.* Mayo Clin Proc, 1977. **52**(12): p. 785-92.

136. Kong, D., X. Kong, and L. Wang, *Effect of cardiac lymph flow obstruction on cardiac collagen synthesis and interstitial fibrosis.* Physiol Res, 2006. **55**(3): p. 253-8.
137. Ludwig, L.L., et al., *Impairment of left ventricular function by acute cardiac lymphatic obstruction.* Cardiovasc Res, 1997. **33**(1): p. 164-71.
138. Taira, A., et al., *Active drainage of cardiac lymph in relation to reduction in size of myocardial infarction: an experimental study.* Angiology, 1990. **41**(12): p. 1029-36.
139. Warren, A.G., et al., *Lymphedema: a comprehensive review.* Ann Plast Surg, 2007. **59**(4): p. 464-72.
140. Stout Gergich, N.L., et al., *Preoperative assessment enables the early diagnosis and successful treatment of lymphedema.* Cancer, 2008. **112**(12): p. 2809-19.
141. Scallan, J.P., et al., *Independent and interactive effects of preload and afterload on the pump function of the isolated lymphangion.* Am J Physiol Heart Circ Physiol, 2012. **303**(7): p. H809-24.
142. Davis, M.J., et al., *Myogenic constriction and dilation of isolated lymphatic vessels.* Am J Physiol Heart Circ Physiol, 2009. **296**(2): p. H293-302.
143. Gashev, A.A., et al., *Regional variations of contractile activity in isolated rat lymphatics.* Microcirculation, 2004. **11**(6): p. 477-92.
144. Gashev, A.A., et al., *Regional heterogeneity of length-tension relationships in rat lymph vessels.* Lymphat Res Biol, 2012. **10**(1): p. 14-9.
145. Zhang, R., et al., *Length-dependence of lymphatic phasic contractile activity under isometric and isobaric conditions.* Microcirculation, 2007. **14**(6): p. 613-25.
146. Zhang, R.Z., et al., *Length-tension relationships of small arteries, veins, and lymphatics from the rat mesenteric microcirculation.* Am J Physiol Heart Circ Physiol, 2007. **292**(4): p. H1943-52.
147. Koller, A., R. Mizuno, and G. Kaley, *Flow reduces the amplitude and increases the frequency of lymphatic vasomotion: role of endothelial prostanoids.* Am J Physiol, 1999. **277**(6 Pt 2): p. R1683-9.
148. Johnston, M.G. and J.L. Gordon, *Regulation of lymphatic contractility by arachidonate metabolites.* Nature, 1981. **293**(5830): p. 294-7.
149. Muthuchamy, M., et al., *Molecular and functional analyses of the contractile apparatus in lymphatic muscle.* FASEB J, 2003. **17**(8): p. 920-2.
150. Arkill, K.P., J. Moger, and C.P. Winlove, *The structure and mechanical properties of collecting lymphatic vessels: an investigation using multimodal nonlinear microscopy.* J Anat, 2010. **216**(5): p. 547-55.
151. Meisner, J.K., et al., *Lymphatic vessels transition to state of summation above a critical contraction frequency.* Am J Physiol Regul Integr Comp Physiol, 2007. **293**(1): p. R200-8.
152. Quick, C.M., et al., *Intrinsic pump-conduit behavior of lymphangions.* Am J Physiol Regul Integr Comp Physiol, 2007. **292**(4): p. R1510-8.
153. Rahbar, E., et al., *Passive pressure-diameter relationship and structural composition of rat mesenteric lymphangions.* Lymphat Res Biol, 2012. **10**(4): p. 152-63.
154. Dixon, J.B., et al., *Lymph flow, shear stress, and lymphocyte velocity in rat mesenteric prenodal lymphatics.* Microcirculation, 2006. **13**(7): p. 597-610.

155. Rahbar, E. and J.E. Moore, Jr., *A model of a radially expanding and contracting lymphangion.* J Biomech, 2011. **44**(6): p. 1001-7.
156. Galie, P. and R.L. Spilker, *A two-dimensional computational model of lymph transport across primary lymphatic valves.* J Biomech Eng, 2009. **131**(11): p. 111004.
157. Mendoza, E. and G.W. Schmid-Schonbein, *A model for mechanics of primary lymphatic valves.* J Biomech Eng, 2003. **125**(3): p. 407-14.
158. Macdonald, A.J., et al., *Modeling flow in collecting lymphatic vessels: one-dimensional flow through a series of contractile elements.* Am J Physiol Heart Circ Physiol, 2008. **295**(1): p. H305-13.
159. Bertram, C.D., C. Macaskill, and J.E. Moore, Jr., *Incorporating measured valve properties into a numerical model of a lymphatic vessel.* Comput Methods Biomech Biomed Engin, 2013.
160. Bertram, C.D., et al., *Development of a model of a multi-lymphangion lymphatic vessel incorporating realistic and measured parameter values.* Biomech Model Mechanobiol, 2014. **13**(2): p. 401-16.
161. USAID, *Report on the global AIDS epidemic*. 2008.
162. Holmberg, S.D., et al., *Protease inhibitors and cardiovascular outcomes in patients with HIV-1.* Lancet, 2002. **360**(9347): p. 1747-8.
163. Lewis, W., et al., *Combined antiretroviral therapy causes cardiomyopathy and elevates plasma lactate in transgenic AIDS mice.* Lab Invest, 2001. **81**(11): p. 1527-36.
164. Lewis, W., et al., *Cardiac Dysfunction Occurs in the HIV-1 Transgenic Mouse Treated with Zidovudine.* Lab Invest, 2000. **80**(2): p. 187-197.
165. Sutliff, R.L., et al., *Nucleoside reverse transcriptase inhibitors impair endothelium-dependent relaxation by increasing superoxide.* Am J Physiol Heart Circ Physiol, 2002. **283**(6): p. H2363-70.
166. Jiang, B., et al., *Antiretrovirals induce direct endothelial dysfunction in vivo.* J Acquir Immune Defic Syndr, 2006. **42**(4): p. 391-5.
167. Kline, E.R. and R.L. Sutliff, *The roles of HIV-1 proteins and antiretroviral drug therapy in HIV-1-associated endothelial dysfunction.* J Investig Med, 2008. **56**(5): p. 752-69.
168. Wang, X., et al., *Molecular mechanisms of HIV protease inhibitor-induced endothelial dysfunction.* J Acquir Immune Defic Syndr, 2007. **44**(5): p. 493-9.
169. Johnsen, S., et al., *Carotid intimal medial thickness in human immunodeficiency virus-infected women: effects of protease inhibitor use, cardiac risk factors, and the metabolic syndrome.* J Clin Endocrinol Metab, 2006. **91**(12): p. 4916-24.
170. Blanco, J.J., et al., *Endothelial function in HIV-infected patients with low or mild cardiovascular risk.* J Antimicrob Chemother, 2006. **58**(1): p. 133-9.
171. Nolan, D., et al., *Endothelial function in HIV-infected patients receiving protease inhibitor therapy: does immune competence affect cardiovascular risk?* QJM, 2003. **96**(11): p. 825-832.
172. Solages, A., et al., *Endothelial function in HIV-infected persons.* Clin Infect Dis, 2006. **42**(9): p. 1325-32.

173. Fontas, E., et al., *Lipid profiles in HIV-infected patients receiving combination antiretroviral therapy: are different antiretroviral drugs associated with different lipid profiles?* J Infect Dis, 2004. **189**(6): p. 1056-74.
174. van Leth, F., et al., *Nevirapine and Efavirenz Elicit Different Changes in Lipid Profiles in Antiretroviral- Therapy-Naive Patients Infected with HIV-1.* PLoS Med, 2004. **1**(1): p. e19.
175. Tohyama, J., et al., *Effects of nevirapine and efavirenz on HDL cholesterol levels and reverse cholesterol transport in mice.* Atherosclerosis, 2009. **204**(2): p. 418-23.
176. van Vonderen, M.G., et al., *Carotid intima-media thickness and arterial stiffness in HIV-infected patients: the role of HIV, antiretroviral therapy, and lipodystrophy.* J Acquir Immune Defic Syndr, 2009. **50**(2): p. 153-61.
177. Humphrey, J.D., et al., *Fundamental role of axial stress in compensatory adaptations by arteries.* J Biomech, 2009. **42**(1): p. 1-8.
178. Gleason, R.L., E. Wilson, and J.D. Humphrey, *Biaxial biomechanical adaptations of mouse carotid arteries cultured at altered axial extension.* J Biomech, 2007. **40**(4): p. 766-76.
179. Maiellaro-Rafferty, K., et al., *Catalase overexpression in aortic smooth muscle prevents pathological mechanical changes underlying abdominal aortic aneurysm formation.* Am J Physiol Heart Circ Physiol, 2011. **301**(2): p. H355-62.
180. Arnet, D., G. Evans, and W. Riley, *Arterial stiffness: a new cardiovascular risk factor?* American Journal of Epidemiology, 1994. **140**: p. 669-682.
181. van Vonderen, M., et al., *Carotid intima-media thickness and arterial stiffness in HIV-infected patients: the role of HIV, antiretroviral therapy, and lipodystrophy.* Journal of Acquired Immune Deficiency Syndromes, 2009. **50**(2): p. 153-161.
182. Yeboah, J., et al., *Predictive value of brachial flow-mediated dilation for incident cardiovascular events in a population-based study: the multi-ethnic study of atherosclerosis.* Circulation, 2009. **120**(6): p. 502-9.
183. Oliviero, U., et al., *Human immunodeficiency virus per se exerts atherogenic effects.* Atherosclerosis, 2009. **204**(2): p. 586-589.
184. Torriani, F., et al., *Endothelial function in human immunodeficiency virus-infected antiretroviral-naive subjects before and after starting potent antiretroviral therapy: The ACTG (AIDS Clinical Trials Group) Study 5152s.* Journal of the American College of Cardiology, 2008. **52**(7): p. 569-576.
185. Chironi, G., et al., *Brief report: carotid intima-media thickness in heavily pretreated HIV-infected patients.* Journal of Acquired Immune Deficiency Syndromes, 2003. **32**(5): p. 490-493.
186. Mercie, P., et al., *Carotid intima-media thickness is slightly increased over time in HIV-1-infected patients.* HIV Med, 2005. **6**(6): p. 380-387.
187. Hsue, P.Y., et al., *Role of viral replication, antiretroviral therapy, and immunodeficiency in HIV-associated atherosclerosis.* AIDS, 2009. **23**(9): p. 1059-67.
188. Mangili, A., et al., *Markers of atherosclerosis and inflammation and mortality in patients with HIV infection.* Atherosclerosis, 2011. **214**(2): p. 468-473.

189. Maggi, P., et al., *Colour-Doppler ultrasonography of carotid vessels in patients treated with antiretroviral therapy: a comparative study.* AIDS, 2004. **18**(7): p. 1023-1028.
190. Kaplan, R.C., et al., *T cell activation and senescence predict subclinical carotid artery disease in HIV-infected women.* The Journal of infectious diseases, 2011. **203**(4): p. 452-463.
191. Longenecker, C., et al., *Markers of inflammation and CD8 T-cell activation, but not monocyte activation, are associated with subclinical carotid artery disease in HIV-infected individuals.* HIV Med, 2013.
192. Ross, A.C., et al., *Heightened inflammation is linked to carotid intima-media thickness and endothelial activation in HIV-infected children.* Atherosclerosis, 2010. **211**(2): p. 492-498.
193. Falcone, E.L., et al., *Framingham risk score and early markers of atherosclerosis in a cohort of adults infected with HIV.* Antiviral therapy, 2011. **16**(1): p. 1-8.
194. Kline, E.R. and R.L. Sutliff, *The role of HIV-1 proteins and antiretroviral drug therapy in HIV-1-associated endothelial dysfunction.* J Investig Med, 2008. **56**(5): p. 752-769.
195. Choi, A.I., et al., *Cardiovascular risks associated with abacavir and tenofovir exposure in HIV-infected persons.* AIDS, 2011. **25**(10): p. 1289-98.
196. Kowalska, J.D., et al., *Implementing the number needed to harm in clinical practice: risk of myocardial infarction in HIV-1-infected patients treated with abacavir.* HIV medicine, 2010. **11**(3): p. 200-8.
197. Worm, S.W., et al., *Risk of myocardial infarction in patients with HIV infection exposed to specific individual antiretroviral drugs from the 3 major drug classes: the data collection on adverse events of anti-HIV drugs (D:A:D) study.* The Journal of infectious diseases, 2010. **201**(3): p. 318-30.
198. Lundgren, J., et al., *Use of nucleoside reverse transcriptase inhibitors and risk of myocardial infarction in HIV-infected patients.* AIDS, 2008. **22**(14): p. F17-24.
199. Ribaudo, H.J., et al., *No risk of myocardial infarction associated with initial antiretroviral treatment containing abacavir: short and long-term results from ACTG A5001/ALLRT.* Clinical infectious diseases : an official publication of the Infectious Diseases Society of America, 2011. **52**(7): p. 929-40.
200. Sutliff, R.L., et al., *Nucleoside reverse transcriptase inhibitors impair endothelium-dependent relaxation by increasing superoxide.* American Journal of Physiology: Heart and Circulatory Physiology, 2002. **283**: p. H2363-H2370.
201. El-Sadr, W.M., et al., *CD4+ count-guided interruption of antiretroviral treatment.* New England Journal of Medicine, 2006. **355**(22): p. 2283-96.
202. Oliviero, U., et al., *Human immunodeficiency virus per se exerts atherogenic effects.* Atherosclerosis, 2009. **204**(2): p. 586-9.
203. Perez-Atayde, A.R., et al., *Cardiac, aortic, and pulmonary arteriopathy in HIV-infected children: the Prospective P2C2 HIV Multicenter Study.* Pediatric and developmental pathology : the official journal of the Society for Pediatric Pathology and the Paediatric Pathology Society, 2004. **7**(1): p. 61-70.
204. Maniker, A.H. and C.D. Hunt, *Cerebral aneurysm in the HIV patient: a report of six cases.* Surg Neurol, 1996. **46**(1): p. 49-54.

205. Blum, A., et al., *Viral load of the human immunodeficiency virus could be an independent risk factor for endothelial dysfunction.* Clin Cardiol, 2005. **28**(3): p. 149-53.
206. Bonnet, D., et al., *Arterial stiffness and endothelial dysfunction in HIV-infected children.* AIDS, 2004. **18**(7): p. 1037-41.
207. Lorenz, M.W., et al., *Both long-term HIV infection and highly active antiretroviral therapy are independent risk factors for early carotid atherosclerosis.* Atherosclerosis, 2007.
208. Buchacz, K., et al., *Changes in lipid profile over 24 months among adults on first-line highly active antiretroviral therapy in the home-based AIDS care program in rural Uganda.* Journal of Acquired Immune Deficiency Syndromes, 2008. **47**(3): p. 304-311.
209. Charakida, M., et al., *Early structural and functional changes of the vasculature in HIV-infected children.* Circulation, 2005.
210. Bonnet, D., et al., *Arterial stiffness and endothelial dysfunction in HIV-infected children.* AIDS, 2004. **18**(7): p. 1037-1041.
211. Ross, A.C., et al., *Longitudinal changes in carotid intima-media thickness and cardiovascular risk factors in human immunodeficiency virus-infected children and young adults compared with healthy controls.* The Pediatric infectious disease journal, 2010. **29**(7): p. 634-638.
212. McComsey, G., et al., *Increased carotid intima media thickness and cardiac biomarkers in HIV infected children.* AIDS, 2007. **21**(8): p. 921-927.
213. Estrada, V. and J. Portilla, *Dyslipidemia related to antiretroviral therapy.* AIDS reviews, 2011. **13**(1): p. 49-56.
214. Loonam, C.R. and A. Mullen, *Nutrition and the HIV-associated lipodystrophy syndrome.* Nutrition research reviews, 2012. **25**(2): p. 267-287.
215. Carr, A., et al., *Diagnosis, prediction, and natural course of HIV-1 protease-inhibitor-associated lipodystrophy, hyperlipidaemia, and diabetes mellitus: a cohort study.* Lancet, 1999. **353**(9170): p. 2093-2099.
216. Werner, M., et al., *Lipodystrophy syndrome and cardiovascular risk factors in children and adolescents infected with HIV/AIDS receiving highly active antiretroviral therapy.* Jornal de Pediatria, 2010. **86**(1): p. 27-32.
217. Beregszaszi, M., et al., *Longitudinal evaluation and risk factors of lipodystrophy and associated metabolic changes in HIV-infected children.* Journal of Acquired Immune Deficiency Syndromes, 2005. **40**(2): p. 161-8.
218. Jaquet, D., et al., *Clinical and metabolic presentation of the lipodystrophic syndrome in HIV-infected children.* AIDS, 2000. **14**(14): p. 2123-8.
219. Leonard, E.G. and G.A. McComsey, *Antiretroviral therapy in HIV-infected children: the metabolic cost of improved survival.* Infectious disease clinics of North America, 2005. **19**(3): p. 713-729.
220. Krause, J.C., et al., *Metabolic abnormalities in human immunodeficiency virus-infected children: two-year follow-up.* Journal of pediatric endocrinology & metabolism : JPEM, 2009. **22**(4): p. 345-351.
221. dos Reis, L.C., et al., *Dyslipidaemia and insulin resistance in vertically HIV-infected children and adolescents.* Transactions of the Royal Society of Tropical Medicine and Hygiene, 2011. **105**(4): p. 197-203.

222. Ridker, P.M., et al., *Comparison of C-reactive protein and low-density lipoprotein cholesterol levels in the prediction of first cardiovascular events.* The New England journal of medicine, 2002. **347**(20): p. 1557-65.
223. Ballantyne, C.M., et al., *Lipoprotein-associated phospholipase A2, high-sensitivity C-reactive protein, and risk for incident ischemic stroke in middle-aged men and women in the Atherosclerosis Risk in Communities (ARIC) study.* Archives of Internal Medicine, 2005. **165**(21): p. 2479-84.
224. Rost, N.S., et al., *Plasma concentration of C-reactive protein and risk of ischemic stroke and transient ischemic attack: the Framingham study.* Stroke; a journal of cerebral circulation, 2001. **32**(11): p. 2575-9.
225. Dolan, S.E., et al., *Increased cardiovascular disease risk indices in HIV-infected women.* Journal of acquired immune deficiency syndromes (1999), 2005. **39**(1): p. 44-54.
226. Masia, M., et al., *The role of C-reactive protein as a marker for cardiovascular risk associated with antiretroviral therapy in HIV-infected patients.* Atherosclerosis, 2007. **195**(1): p. 167-71.
227. Ross, A.C., et al., *Endothelial activation markers are linked to HIV status and are independent of antiretroviral therapy and lipoatrophy.* Journal of acquired immune deficiency syndromes, 2008. **49**(5): p. 499-506.
228. Kristoffersen, U., et al., *Reduction in circulating markers of endothelial dysfunction in HIV-infected patients during antiretroviral therapy.* HIV Med, 2009. **10**(2): p. 79-87.
229. Lichtner, M., et al., *Increased carotid intima media thickness is associated with depletion of circulating myeloid dendritic cells in HIV-infected patients on suppressive antiretroviral treatment.* Atherosclerosis, 2009. **204**(2): p. e1-3.
230. Hsue, P., et al., *Role of viral replication, antiretroviral therapy, and immunodeficiency in HIV-associated atherosclerosis.* AIDS, 2009. **23**(9): p. 1059-1067.
231. Neuhaus, J., et al., *Markers of inflammation, coagulation, and renal function are elevated in adults with HIV infection.* The Journal of infectious diseases, 2010. **201**(12): p. 1788-1795.
232. Miller, T.L., et al., *Biomarkers of vascular dysfunction in children infected with human immunodeficiency virus-1.* Journal of acquired immune deficiency syndromes (1999), 2010. **55**(2): p. 182-188.
233. Baker, J., et al., *High-density lipoprotein particles and markers of inflammation and thrombotic activity in patients with untreated HIV infection.* Journal of Infectious Diseases, 2010. **201**(2): p. 285-292.
234. Calmy, A., et al., *HIV increases markers of cardiovascular risk: results from a randomized, treatment interruption trial.* AIDS, 2009. **23**(8): p. 929-939.
235. Masiá, M., et al., *Endothelial function is impaired in HIV-infected patients with lipodystrophy.* Antiviral therapy, 2010. **15**(1): p. 101-110.
236. Galkina, E. and K. Ley, *Vascular adhesion molecules in atherosclerosis.* Arteriosclerosis, Thrombosis, and Vascular Biology, 2007. **27**(11): p. 2292-301.
237. Gattegno, L., et al., *Elevated concentrations of circulating intercellular adhesion molecule 1 (ICAM-1) and of vascular cell adhesion molecule 1 (VCAM-1) in HIV-1 infection.* Cell Adhesion and Communication, 1995. **3**(3): p. 179-85.

238. Mastroianni, C.M., et al., *Changes in circulating levels of soluble cell adhesion molecules following highly active antiretroviral treatment of HIV-1-infected patients.* Clinical immunology (Orlando, Fla.), 2000. **95**(3): p. 212-217.
239. Matarese, G., C. Mantzoros, and A. La Cava, *Leptin and adipocytokines: bridging the gap between immunity and atherosclerosis.* Current Pharmaceutical Design, 2007. **13**(36): p. 3676-80.
240. Takemura, Y., K. Walsh, and N. Ouchi, *Adiponectin and cardiovascular inflammatory responses.* Current atherosclerosis reports, 2007. **9**(3): p. 238-43.
241. Gougeon, M.L., et al., *Adipocytes targets and actors in the pathogenesis of HIV-associated lipodystrophy and metabolic alterations.* Antiviral therapy, 2004. **9**(2): p. 161-77.
242. Choi, A.I., et al., *Cardiovascular risks associated with abacavir and tenofovir exposure in HIV-infected persons.* AIDS, 2011.
243. Gleason, R.L., et al., *A multiaxial computer-controlled organ culture and biomechanical device for mouse carotid arteries.* J Biomech Eng, 2004. **126**(6): p. 787-95.
244. Doran, D.E., et al., *Differential effects of AT1 receptor and Ca2+ channel blockade on atherosclerosis, inflammatory gene expression, and production of reactive oxygen species.* Atherosclerosis, 2007. **195**(1): p. 39-47.
245. Wan, W., H. Yanagisawa, and R.L. Gleason, Jr., *Biomechanical and microstructural properties of common carotid arteries from fibulin-5 null mice.* Ann Biomed Eng, 2010. **38**(12): p. 3605-17.
246. Mukhamedova, N., et al., *Antiretroviral compounds and cholesterol efflux from macrophages.* Atherosclerosis, 2009. **206**(2): p. 439-43.
247. Balani, S.K., et al., *Nonlinear pharmacokinetics of efavirenz (DMP-266), a potent HIV-1 reverse transcriptase inhibitor, in rats and monkeys.* Drug Metab Dispos, 1999. **27**(1): p. 41-5.
248. Back, D.J., A. Owen, and S.H. Khoo, *Population pharmacokinetics of efavirenz in an unselected cohort of HIV-1-infected individuals.* Clin Pharmacokinet, 2006. **45**(2): p. 213-4; author reply 214-5.
249. Chiappetta, D.A., et al., *Oral pharmacokinetics of the anti-HIV efavirenz encapsulated within polymeric micelles.* Biomaterials, 2011. **32**(9): p. 2379-87.
250. Dixon, J.B., *Lymphatic lipid transport: sewer or subway?* Trends Endocrinol Metab, 2010. **21**(8): p. 480-7.
251. Deng, X., et al., *Mechanical characteristics of the canine thoracic duct: what are the driving forces of the lymph flow?* Biorheology, 1999. **36**(5-6): p. 391-9.
252. Humphrey, J.D., *Mechanisms of arterial remodeling in hypertension: coupled roles of wall shear and intramural stress.* Hypertension, 2008. **52**(2): p. 195-200.
253. Zoumi, A., et al., *Imaging coronary artery microstructure using second-harmonic and two-photon fluorescence microscopy.* Biophysical Journal, 2004. **87**(4): p. 2778-2786.
254. Baek, S., et al., *Theory of small on large: Potential utility in computations of fluid–solid interactions in arteries.* Computer Methods in Applied Mechanics and Engineering, 2007. **196**(31–32): p. 3070-3078.
255. Dobrin, P.B., *Biaxial anisotropy of dog carotid artery: estimation of circumferential elastic modulus.* J Biomech, 1986. **19**(5): p. 351-8.

256. Cheng, J.K., et al., *A fiber-based constitutive model predicts changes in amount and organization of matrix proteins with development and disease in the mouse aorta.* Biomech Model Mechanobiol, 2013. **12**(3): p. 497-510.
257. Humphrey, J.D., et al., *Computer-aided vascular experimentation: a new electromechanical test system.* Ann Biomed Eng, 1993. **21**(1): p. 33-43.
258. Akcali, O., et al., *Thoracic duct variations may complicate the anterior spine procedures.* Eur Spine J, 2006. **15**(9): p. 1347-51.
259. Ferruzzi, J., D.A. Vorp, and J.D. Humphrey, *On constitutive descriptors of the biaxial mechanical behaviour of human abdominal aorta and aneurysms.* J R Soc Interface, 2011. **8**(56): p. 435-50.
260. Eberth, J.F., et al., *Mechanics of carotid arteries in a mouse model of Marfan Syndrome.* Ann Biomed Eng, 2009. **37**(6): p. 1093-104.
261. Holzapfel, G.A., T.C. Gasser, and R.W. Ogden, *Comparison of a multi-layer structural model for arterial walls with a fung-type model, and issues of material stability.* J Biomech Eng, 2004. **126**(2): p. 264-75.
262. McGeown, J.G., et al., *Peripheral lymphatic responses to outflow pressure in anaesthetized sheep.* J Physiol, 1987. **383**: p. 527-36.
263. Zawieja, D.C., et al., *Distribution, propagation, and coordination of contractile activity in lymphatics.* Am J Physiol, 1993. **264**(4 Pt 2): p. H1283-91.
264. Dixon, J.B., et al., *Measuring microlymphatic flow using fast video microscopy.* J Biomed Opt, 2005. **10**(6): p. 064016.
265. Langille, B.L., *Remodeling of developing and mature arteries: endothelium, smooth muscle, and matrix.* J Cardiovasc Pharmacol, 1993. **21 Suppl 1**: p. S11-7.
266. Baeyens, N., et al., *Vascular remodeling is governed by a VEGFR3-dependent fluid shear stress set point.* Elife, 2015. **4**.
267. Rutkowski, J.M., et al., *Secondary lymphedema in the mouse tail: Lymphatic hyperplasia, VEGF-C upregulation, and the protective role of MMP-9.* Microvasc Res, 2006. **72**(3): p. 161-71.
268. Fridez, P., et al., *Model of geometrical and smooth muscle tone adaptation of carotid artery subject to step change in pressure.* Am J Physiol Heart Circ Physiol, 2001. **280**(6): p. H2752-60.
269. Rachev, A., et al., *A model of stress-induced geometrical remodeling of vessel segments adjacent to stents and artery/graft anastomoses.* J Theor Biol, 2000. **206**(3): p. 429-43.
270. Rodriguez, E.K., A. Hoger, and A.D. McCulloch, *Stress-dependent finite growth in soft elastic tissues.* J Biomech, 1994. **27**(4): p. 455-67.
271. Ogata, F., et al., *Phenotypic modulation of smooth muscle cells in lymphedema.* Br J Dermatol, 2014.